

Carnegie Mellon University  
CARNEGIE INSTITUTE OF TECHNOLOGY

THESIS

Submitted in Partial Fulfillment of the Requirements  
For the Degree of Doctor of Philosophy

TITLE

**MECHANICS OF ADHESION AND CONTACT SELF-CLEANING OF  
BIO-INSPIRED MICROFIBER ADHESIVES**

PRESENTED BY

UYIOSA ANTHONY ABUSOMWAN

07.11.2014

ACCEPTED BY THE DEPARTMENT OF MECHANICAL ENGINEERING

---

MAJOR PROFESSOR

DATE

---

DEPARTMENT HEAD

DATE

APPROVED BY THE COLLEGE COUNCIL

---

DEAN

DATE

# **MECHANICS OF ADHESION AND CONTACT SELF-CLEANING OF BIO-INSPIRED MICROFIBER ADHESIVES**

## **Thesis Committee**

Professor Metin Sitti, Chair  
Professor Kellar Autumn  
Professor C. Fred Higgs, III  
Professor Maarten de Boer

Uyiosa Anthony Abusomwan  
July 11th, 2014

© Copyright by Uyiosa A. Abusomwan 2014  
All Rights Reserved

*For my entire family, and those whose lives have inspired me.*



## Abstract

The remarkable attachment system of geckos has inspired the development of dry microfiber adhesives through the last two decades. Some of the notable characteristics of gecko-inspired fibrillar adhesives include: strong, directional, and controllable adhesion to smooth and rough surfaces in air, vacuum, and under water; ability to maintain strong adhesion during repeated use; anti-fouling and self-cleaning after contamination. Given these outstanding qualities, fibrillar adhesives promise an extensive range of use in industrial, robotic, manufacturing, medical, and consumer products. Significant advancements have been made in the design of gecko-inspired microfiber adhesives with the characteristic properties listed above, with the exception of the anti-fouling and self-cleaning features. The self-cleaning mechanism of the gecko's adhesion system plays an important role to its ability to remain sticky in various environments. Similarly, enabling self-cleaning capability for synthetic microfiber adhesives will lead to robust performance in various areas of application. Presently, the practical use of fibrillar adhesives is restricted mainly to clean environments, where they are free from contaminants.

The goal of this thesis is to conduct a detailed study of the mechanisms and mechanics of contact-based self-cleaning of gecko-inspired microfiber adhesives. This work focuses on contact self-cleaning mechanisms, as a more practical approach to cleaning. Previous studies on the cleaning of microfiber adhesives have mostly focused on mechanisms that involve complete removal of the contaminants from the adhesive. In this thesis, a second cleaning process is proposed whereby particles are removed from the tip of the microfibers and embedded between adjacent microfibers or in grooves patterned onto the adhesive, where they are no longer detrimental to the performance of the adhesive.

In this work, a model of adhesion for microfiber adhesives that take the deformation of the backing layer under individual microfiber is developed. The dependence of adhesion of microfiber adhesives on the rate of unloading is also modeled and verified using experiments. The models of adhesion presented are later used to study the mechanics of contact self-cleaning of microfiber adhesives. Three major categories of self-cleaning are identified as wet self-cleaning, dynamic self-cleaning, and contact self-cleaning. A total of seven self-cleaning mechanisms that are associated with these categories are also presented and discussed.

Results from the self-cleaning model and experiments show that shear loading plays an important role in self-cleaning. The underlying mechanism of contact self-cleaning due to normal and shear loading for spherical contaminants is found to be the particle rolling between the adhesive and a contacted substrate. Results from the model and experiments also show that small microfiber tips (much less than the size of the contaminants) are favorable for self-cleaning. On the other hand, large microfiber tips (much larger than the size of the contaminants) are favorable for anti-fouling of the microfiber adhesive. Results from this work suggests that the sub-micrometer size of the gecko's adhesive fibers and the lamellae under the gecko toes contribute to its outstanding self-cleaning performance.

The results presented in this thesis can be implemented in the design of microfiber adhesives with robust adhesion, self-cleaning and anti-fouling characteristic, for use in numerous applications and in various environments.

## Acknowledgments

I wish to thank my wife Evangeline for her tremendous support and inspiration. In addition, I wish to thank my entire family, including my parents Mr. and Mrs. Efosa Anthony Abusomwan, and eight siblings Osadebamwen, Ikpomwosa, Osamede, Charity, Ehimwenma, Amenaghawon, Ighagosa and Idanosa, for their unconditional love, support and continued encouragement throughout my PhD study.

My advisor and thesis committee chair Professor Metin Sitti, has been the backbone of my thesis study right from the inception. He inspired and motivated me to pursue a doctoral degree when I wasn't sure of what was ahead for me, and assisted me all through the way while writing this chapter of my life. I also thank my thesis committee members Professor Kellar Autumn, Professor C. Fred Higgs, III, and Professor Maarten de Boer for their support.

Most of this work were done on the shoulders of past members of the NanoRobotics Lab. The tremendous work of Burak Aksak, provided a solid foundation for the modeling section of this thesis. My research work in the lab began under the mentorship of Yigit Menguc who later created the opportunity and directed my paths towards the study of self-cleaning of gecko-inspired adhesives. I couldn't have done this work without his support. Members of the NanoRobotics lab have contributed significantly to this work through systematic reviews, insights, and discussions, and have continuously provided encouragements throughout my research study. These include Rika Wright Carlson, Lindsey Hines, Eric Diller, Sehyuk Yim, Matthew Woodward, Jiho Song, Onur Ozcan, Slava Arabagi, Veikko Sariola, Jiang Zhuang, Joshua Giltinan, Sukho Song, Zhou Ye, Donghoon Son, Guo Zhan Lum, Xiaoguang Dong, David Colmenares, Hamid Marvi, Su Eun Chung, Randall Kania, and Yuanfeng Han. I would also like to thank Paul Glass and others at nanoGriptech for their support with sample fabrication.

My cousin Jason Abusomwan, his wife Jennifer and their two sons helped to make my stay in Pittsburgh very pleasurable. The members of RCCG Pittsburgh have also been a family to me throughout my stay in this beautiful city. I will also like to acknowledge the support of Stephen Oppong and his wife Christiana, Pastor A. Oni, and Mr. Michael Adamczyk for their mentorship roles in both my academic and career through the years. I would also like to thank the Mechanical Engineering staff including Chris Hertz, Mike Scampone, Bobbi Kostyak, Ed Wojciechowski and John Fulmer for their support.

Financial support has been through the National Science Foundation Graduate Research Fellowship (0946825), the National Science Foundation (CMMI-1130520), and the Department of Mechanical Engineering at Carnegie Mellon.

# Contents

<b>Abstract</b>	<b>iv</b>
<b>Acknowledgments</b>	<b>v</b>
<b>List of Figures</b>	<b>viii</b>
<b>List of Tables</b>	<b>xi</b>
<b>Nomenclature</b>	<b>xii</b>
<b>1 Introduction</b>	<b>1</b>
1.1 Motivation . . . . .	1
1.2 Background of Adhesion of Biological Gecko Foot-Hairs . . . . .	2
1.3 Self-Cleaning in Geckos . . . . .	4
1.4 Introduction to Synthetic Microfiber Adhesives . . . . .	5
1.5 Applications of Microfiber Adhesives . . . . .	8
1.6 Research Objectives . . . . .	10
1.7 Expected Contributions . . . . .	12
<b>2 Adhesion of Gecko-Inspired Microfiber Adhesives</b>	<b>14</b>
2.1 Introduction . . . . .	14
2.2 Adhesive Force of a Single Elastomeric Microfiber . . . . .	16
2.3 Adhesive Force of a Microfiber Array . . . . .	19
2.3.1 Adhesion with a Flat Surface . . . . .	20
2.3.2 Adhesion with a Spherical Surface . . . . .	21
2.3.3 Results and Discussions . . . . .	27
2.3.4 Conclusion . . . . .	41
2.4 Rate-dependent Adhesion of Microfiber Adhesives . . . . .	41
2.4.1 Introduction . . . . .	41
2.4.2 Experiments . . . . .	42
2.4.3 Theoretical Model . . . . .	45
2.4.4 Results and Discussions . . . . .	46
2.4.5 Conclusion . . . . .	50
2.5 Summary . . . . .	51

<b>3</b>	<b>Mechanisms and Mechanics of Contact Self-cleaning in Microfiber Adhesives</b>	<b>52</b>
3.1	Introduction . . . . .	52
3.1.1	What is Self-cleaning? . . . . .	52
3.1.2	Self-cleaning in Nature . . . . .	54
3.1.3	Self-cleaning of Synthetic Microfiber Adhesives . . . . .	57
3.2	Mechanisms of Self-cleaning of Microfiber Adhesives . . . . .	58
3.2.1	Mechanisms of Wet Self-cleaning . . . . .	58
3.2.2	Mechanisms of Dynamic Self-cleaning . . . . .	60
3.2.3	Mechanisms of Contact Self-cleaning . . . . .	60
3.3	Mechanics of Contact Self-Cleaning of Microfiber Adhesives . . . . .	62
3.3.1	Introduction . . . . .	62
3.3.2	Contact Self-cleaning Model for Small Contaminants ( $\kappa \ll 1$ ) . . . . .	66
3.3.3	Contact Self-cleaning Model for Large Contaminants ( $\kappa \gg 1$ ) . . . . .	72
3.4	Summary . . . . .	78
<b>4</b>	<b>Experiments and Simulation of Contact Self-cleaning of Microfiber Adhesives</b>	<b>80</b>
4.1	Introduction . . . . .	80
4.2	Experiment I: Effect of Contaminant Size Regimes on the Contact Self-cleaning Performance of Microfiber Adhesives . . . . .	81
4.2.1	Experimental Methodology . . . . .	81
4.2.2	Results and Discussions . . . . .	85
4.2.3	Conclusions . . . . .	93
4.3	Experiment II: The Mechanism of Contact Self-cleaning of Microfiber Adhesives Using the Load-Drag-Unload Procedure . . . . .	95
4.3.1	Experimental Methodology . . . . .	95
4.3.2	Results and Discussions . . . . .	97
4.3.3	Conclusions . . . . .	106
4.4	Simulation of Contact Self-cleaning for Microfiber Adhesives . . . . .	108
4.4.1	Introduction . . . . .	108
4.4.2	Simulation Methodology . . . . .	109
4.4.3	Results and Discussions . . . . .	111
4.5	Summary . . . . .	113
<b>5</b>	<b>Design Considerations for Contact Self-cleaning of Microfiber Adhesives</b>	<b>116</b>
5.1	Introduction . . . . .	116
5.2	Factors that Influence Self-cleaning and Anti-fouling of Microfiber Adhesives . . . . .	117
5.2.1	Microfiber Tip Shape . . . . .	117
5.2.2	Microfiber Tip Radius . . . . .	119
5.2.3	Contaminant Size . . . . .	119
5.2.4	Loading Condition . . . . .	120
5.3	Microfiber Design Considerations for Self-cleaning Based on Application Procedure . . . . .	121
5.3.1	Considerations for the load-unload procedure . . . . .	121
5.3.2	Considerations for the load-drag-unload procedure . . . . .	122

5.4	Microfiber Design Considerations for Anti-fouling . . . . .	125
5.5	Case Study: Design of a Self-cleaning Microfiber Adhesive Patch for Use in an Office Environment . . . . .	127
5.6	Summary . . . . .	130
<b>6</b>	<b>Summary and Conclusion</b>	<b>132</b>
6.1	Overview of Contributions . . . . .	132
6.1.1	Adhesion Modeling for Microfiber Adhesives . . . . .	132
6.1.2	Mechanisms of Self-cleaning . . . . .	133
6.1.3	Mechanics of Contact Self-cleaning . . . . .	133
6.1.4	Experiments and Simulation of Contact Self-cleaning . . . . .	134
6.1.5	Design Considerations for Microfiber Adhesives with Contact Self-cleaning or Anti-fouling Characteristics . . . . .	135
6.2	Outlook . . . . .	135
<b>A</b>	<b>Numerical Simulations</b>	<b>137</b>
A.1	Simulation Steps for Obtaining the Indentation Distance of a Spherical Indenter on a Microfiber Array . . . . .	137
A.2	Simulation Steps for Contact Self-cleaning of Microfiber Adhesives Based on the Load-Drag-Unload Procedure . . . . .	140
A.2.1	LEVEL I: Obtaining the Adhesive Force of a Contaminated Microfiber array . . . . .	141
A.2.2	LEVEL II: Applying a Normal Load to Simulate Loading . . . . .	142
A.2.3	LEVEL III: Applying a Horizontal Displacement to Simulate Dragging . . . . .	143
<b>B</b>	<b>Visualization of the Contact Area Using Interferometric Microscopy</b>	<b>145</b>
	<b>Bibliography</b>	<b>147</b>

# List of Figures

1.1	Images showing the gecko's adhesion system. . . . .	3
1.2	Self-cleaning in Geckos . . . . .	5
1.3	SEM images of synthetic gecko adhesives. . . . .	6
1.4	Images showing some applications of fibrillar adhesives. . . . .	9
2.1	Schematic of loading and deformation of a single microfiber and backing layer.	17
2.2	Schematic of loading and deformation of microfiber array by a spherical indenter showing the top and side view. . . . .	22
2.3	Flowchart for obtaining the indentation distance. . . . .	25
2.4	Graph of load plotted against indentation distance during loading/unloading simulation. . . . .	26
2.5	Effect of preload force on adhesion. . . . .	29
2.6	Effect of microfiber radius on adhesion. . . . .	31
2.7	Effect of microfiber radius on adhesion. . . . .	32
2.8	Effect of microfiber length on adhesion. . . . .	33
2.9	Effect of microfiber Young's modulus on adhesion. . . . .	35
2.10	Effect of microfiber spacing on adhesion. . . . .	36
2.11	Effect of indenter radius on adhesion. . . . .	38
2.12	Effect of $w$ on adhesion. . . . .	40
2.13	Procedures for fabricating a single cylindrical microfiber post. . . . .	43
2.14	Schematic drawing of a custom built experimental setup. . . . .	44
2.15	A graph of measured force in real time with corresponding images. . . . .	45
2.16	Graph showing the effect of retraction speed on adhesive force. . . . .	48
2.17	Graph showing the effect of crack propagation speed on energy release rate. . .	49
3.1	SEM images showing the surface topography of natural organisms with self-cleaning characteristics. . . . .	55
3.2	Evidence of self-cleaning in gecko setae. . . . .	56
3.3	Mechanisms of self-cleaning of microfiber Adhesives. . . . .	59
3.4	Schematics of contaminated microfiber adhesives showing contaminant size regimes. . . . .	64
3.5	Schematic diagrams illustrating the contact self-cleaning procedures and particle displacements. . . . .	65

3.6	Loading conditions for a single particle sandwiched between a microfiber tip and a glass substrate during the load-drag-unload cleaning processes for the small contaminant regime ( $\kappa \ll 1$ ). . . . .	68
3.7	Contact self-cleaning map for a 46.2 $\mu\text{m}$ diameter glass particle in the small contaminant regime shows the vertical and lateral loads that result in contact self-cleaning (grey region) by particle rolling or sliding as predicted by equation 3.13. . . . .	73
3.8	Loading conditions for a single particle sandwiched between a microfiber array and a glass substrate during the load-drag-unload cleaning processes for the large contaminant regime ( $\kappa \gg 1$ ). . . . .	74
3.9	Coefficient of cleaning by adhesion process . . . . .	76
4.1	Self-cleaning experiment results showing the relative adhesion for the large, intermediate and small contaminant regimes, and the flat control sample. . . . .	86
4.2	SEM images of samples in the small, intermediate and large contaminant regimes before and after contact self-cleaning shows significant cleaning in all regimes. . . . .	88
4.3	SEM images of samples in the small, intermediate and large contaminant regimes before and after contact self-cleaning shows significant cleaning in all regimes. . . . .	89
4.4	Images of the 2-axis force measurement system used in the self-cleaning experiments. . . . .	96
4.5	Schematics of a single contaminating particle sandwiched between a polyurethane microfiber tip and a hard glass substrate, before and after the substrate is dragged. . . . .	98
4.6	Graphs of the normalized particle displacements measured at various normal loads for a 250 $\mu\text{m}$ diameter contaminant particle sandwiched between a microfiber array and dragged horizontally at a speed of 20 $\mu\text{m/s}$ . . . . .	100
4.7	Graph of the normal and tangential forces measured during a single contact self-cleaning experiment with a 1 mm diameter silica micro-particle rolling across a flat polyurethane adhesive sample, for a normal load of 120 mN and a drag speed of 10 $\mu\text{m/s}$ . . . . .	102
4.8	Graphs showing the dependence of rolling friction on the drag speed and normal load for a 1 mm diameter particle. . . . .	103
4.9	Experimental and theoretical results from equation 4.10 of the dependence of rolling friction on both normal load and drag speed. . . . .	107
4.10	An illustrative diagram with dimensions showing the side view of a contaminated microfiber array used in the simulation of contact self-cleaning via the load-drag-unload procedure. . . . .	109
4.11	A numerical simulation flow chart for contact self-cleaning of microfiber adhesives using the load-drag-unload procedure. . . . .	112
4.12	Results of numerical simulation of contact self-cleaning of a microfiber adhesive array contaminated with small and large microspheres using the load-drag-unload procedure. . . . .	113

5.1	Microfiber tip shapes and their effect on self-cleaning. . . . .	118
5.2	Results of a preliminary study to show the advantage of implementing a groove pattern in the microfiber adhesive array. . . . .	124
5.3	Morphology of tree frog toe showing hexagonal patterned adhesive pad. . . . .	125
5.4	Schematic view of a microfiber array with groove pattern. . . . .	129
A.1	Flowchart for obtaining the indentation distance. . . . .	138
A.2	A numerical simulation flow chart for contact self-cleaning of microfiber adhesives using the load-drag-unload procedure. . . . .	140
B.1	Schematics of a typical experimental setup to observe contact area using interferometric microscopy. . . . .	146



# List of Tables

2.1	Simulated parameter values used to study the effects of microfiber length, microfiber radius, microfiber Young's modulus, microfiber spacing, interface work of adhesion, indenter radius, and preload force on adhesion. The value highlighted for each parameter is the default value used when testing other parameters	27
2.2	Effect of various microfiber parameters on adhesion. Arrow indicates increasing ( $\uparrow$ ) or decreasing ( $\downarrow$ ) values. . . . .	39
4.1	Dimensions of the microfiber adhesive samples and contaminating microspheres that were used in the experiments. The samples were grouped into small ( $\kappa \ll 1$ ), intermediate ( $\kappa \approx 1$ ) and large ( $\kappa \gg 1$ ) contaminant regimes. $D_s$ is the microfiber tip diameter, $D_p$ is the mean particle diameter and $\kappa = D_p/D_s$ . $\phi$ refers to the diameter dimension of the particles. . . . .	83
4.2	Simulation results of the clean $P_{\text{clean}}$ and dirty $P_{\text{dirty}}$ adhesion of a microfiber array contaminated with large microspheres ( $\kappa = 10.7$ and $\kappa = 5.9$ ) and small microspheres ( $\kappa = 0.1$ ). Comparison of the calculated dirty adhesion due to the contributions of the small microsphere to the clean adhesion resulted in a 21.1% relative adhesion, whereas larger microspheres resulted in as low as 0.56% relative adhesion. Note that these results were for the maximum number of contaminants possible in the array. In practice, the number of contaminating particles could be less, resulting in a smaller adhesive force. $D_p$ is the mean particle diameter, $\sigma_0$ is the interfacial strength of the microfibers, $N_s$ is the number of microspheres in contact with the substrate and $\kappa = D_p/D_s$ . . . . .	91
5.1	Size distribution of about 11 kg of bulk dust obtained from seven Danish office buildings with about 1047 occupants [99]. . . . .	128

# Nomenclature

$f_y$	Applied shear force
$\Delta$	Indentation depth
$\delta$	Total deformation (single microfiber)
$\delta x$	particle displacement
$\delta_b$	Backing layer deformation (single microfiber)
$\delta_{cr}$	Critical buckling deformation (single microfiber)
$\delta_c$	Maximum tensile deformation before pull-off (single microfiber)
$\delta_f$	Stem deformation (single microfiber)
$\Delta_p$	Indentation distance at preload
$\Delta_x$	Applied drag distance
$\eta$	Normalized particle rolling
$\gamma$	Surface energy
$\kappa$	Ratio of particle diameter to microfiber tip diameter
$\mu$	Friction coefficient
$\mu_{\text{Tabor}}$	Tabor parameter
$\rho$	Number of microfibers per unit area
$\rho_a$	Radius of curvature of a microfiber tip with spherical geometry
$\sigma_0$	Interface strength
$\tau$	Interface shear strength
$\varrho$	Cleaning coefficient
$\xi$	Critical rolling distance
$A$	apparent contact area
$a$	Stem radius (single microfiber)
$A_{\text{max}}$	Apparent contact area at preload
$a_p$	Width of contact gap as a result of a contaminant
$A_{\text{real}}$	True contact area
$A_{\text{real}}^c$	True contact area at $t_c$

$a_t$	Tip radius (single microfiber)
$C$	Total compliance (single microfiber)
$C_b$	Backing layer compliance (single microfiber)
$CF$	Contaminant-microfiber interface
$CS$	Contaminant-substrate interface
$d$	Distance between centers of adjacent microfibers
$D_f$	Microfiber tip diameter
$D_s$	Spherical contaminant diameter
$E_f$	Microfiber effective modulus
$F$	Applied normal load (single microfiber)
$F_c$	Adhesive force (single microfiber)
$f_{\text{fiber}}$	Critical shear force for particle sliding across microfiber
$F_p$	Adhesive force of a single particle
$f_{\text{rolling}}$	Critical shear force for particle rolling
$f_{\text{substrate}}$	Critical shear force for particle sliding across sub
$F_{cr}$	Critical buckling load (single microfiber)
$G$	Energy release rate
$G_0$	Critical energy release rate as $v \rightarrow 0$
$G_i$	Shear modulus of material i
$M_T$	Total rolling moment resistance
$n$	Fitting parameter for rate dependence on adhesion
$N_f$	Number of microfibers in contact
$N_p$	Number of particles simulataneously in contact with a substrate
$N_{\text{samples}}$	Number of samples tested in an experiment
$P$	Normal load
$P_{cf}$	Adhesive force of the contaminant-microfiber interface
$P_{\text{cleaned}}$	Adhesive force measured after a cleaning cycle
$P_{\text{clean}}$	Adhesive force measured before contamination
$P_{cs}$	Adhesive force of the contaminant-substrate interface
$P_c$	Adhesive force of a microfiber array
$p_c$	Adhesive strenfth of a microfiber array
$P_{\text{dirty}}$	Adhesive force measured immediately after contamination
$P_p$	Preload
$R$	Radius of a spherical particle

$R$	Radius of an indenter surface
$r$	Radial distance from the center of an indenter
$r_{cf}$	Contact radius of the contaminant-microfiber interface
$r_{cs}$	Contact radius of the contaminant-substrate interface
$r_c$	Apparent contact radius
$S$	Microfiber edge-to-edge spacing distance
$t_c$	time pull-off force is recorded
$V$	Drag speed
$v$	Crack propagation speed
$v_0$	Crack propagation speed
$w$	Work of adhesion
$w_{cf}$	Work of adhesion at the contaminant-microfiber interface
$w_{cs}$	Work of adhesion at the contaminant-substrate interface
$z_0$	Effective range of action of adhesive forces
$\gamma_f$	Microfiber surface energy
$\nu_f$	Microfiber Poisson's ratio
$\nu_s$	Substrate Poisson's ratio
$C_f$	Stem compliance (single microfiber)
$E_f$	Microfiber Young's modulus
$E_s$	Substrate Young's modulus
$f_{cf}$	Critical shear force for particle sliding across microfiber
$f_{cs}$	Critical shear force for particle sliding across substrate
$f_R$	Critical shear force for particle rolling
$K$	Reduced elastic modulus
$(p_x, p_y)$	$x$ and $y$ coordinates of the indenter relative to the microfiber array.
DMT	Derjaguin-Muller-Toporov
JKR	Johnson-Kendall-Roberts
LDU	Load-drag-unload procedure
LU	Load-unload procedure
SEM	Scanning electrom microscopy

# Chapter 1

## Introduction

### 1.1 Motivation

The attachment mechanisms of some natural organisms have fueled the curiosity of investigators for several centuries [5]. From large mammals to tiny insects, natural organisms possess remarkable systems, some of which are beyond the explanation of present day science. A very good example is the ability of a 50 g Tokay Gecko to walk on vertical and inverted flat surfaces, seemingly defying gravity. Interest in geckos' adhesion system grew significantly after the initial work of Autumn et al. in 2000, [10] characterizing the adhesive force of a single gecko hair; and later in 2002, [15] demonstrating that the gecko's remarkable adhesion system is mostly due to van der Waals intermolecular forces. The gecko's unique attachment system has been the inspiration for the design of dry microfiber adhesives over the last two decades [2, 20, 21, 43, 66, 77, 78, 104, 115, 116, 120, 122, 124, 139]. Some featured characteristics of gecko-inspired adhesives include: strong, directional, controllable and residue-free adhesion to smooth and rough surfaces in air, vacuum, and underwater; ability to retain good adhesive strength after repeated use; and anti-fouling and recovery of adhesive strength after contamination. Given these outstanding qualities, fibrillar adhesives promise an extensive range of applications in industrial [78, 83, 96], robotic [9, 18, 48, 54, 97, 98, 100, 101, 117, 118, 135], man-

ufacturing [69, 78], medical applications [26, 30, 82, 91], and consumer products. Significant advancements have been made in the various characteristic properties of gecko-inspired fibrillar adhesives with the exception of the anti-fouling and self-cleaning characteristics. [20, 115].

The gecko maintains a contamination-free adhesion system through a mechanism that allows it to clean off contaminants from its toes during normal use [52]. This feature is very crucial to the gecko ability to remain sticky in various environments. Similarly, a good cleaning mechanism for fibrillar adhesives will lead to robust performance in various areas of application. Presently, microfiber adhesives can only be used in clean environments, extremely limiting practical use. A thorough understanding and model of cleaning for fibrillar adhesives will help in the design of synthetic microfiber adhesives that (I) maintain high adhesive strength in the presence of contaminants, and (II) can easily recover its lost adhesive strength after contamination. Such a model can also help to extend the number of usage cycles for microfiber adhesives. The importance of self-cleaning for practical application of fibrillar adhesives, and the limited understanding in this area is the inspiration and motivation for this work.

In this chapter, we present previous work, the current state, as well as the prospective areas of application of microfiber adhesives. We conclude this chapter with the objectives and expected contributions of this research.

## **1.2 Background of Adhesion of Biological Gecko Foot-Hairs**

Under the toes of the Tokay Gecko are arrays of fine, hair-like, fibrillar structures known as setae (see Figure 1.1). Made of beta-keratin, the seta is a long stiff microfiber with a Young's modulus varying between 1 and 4 GPa, and a diameter ranging from 0.2 to 5  $\mu\text{m}$ . Each seta branches into finer microfibers with 100 to 300 nm tips called spatulae [7, 10, 109]. The ability of the geckos' toes to "stick" to contacting surfaces is due to intermolecular forces of adhesion, mostly van der Waals forces, between the setae and the contacting surfaces [10, 15]. The high aspect ratio fibrillar structures allow the geckos' adhesive to conform to irregular surfaces and

maintain intimate tip contact, a phenomenon known as *contact splitting* [6, 8, 15]. As a result of its unique adhesion system, the gecko's toes remain sticky both in vacuum and underwater unlike many other adhesives.

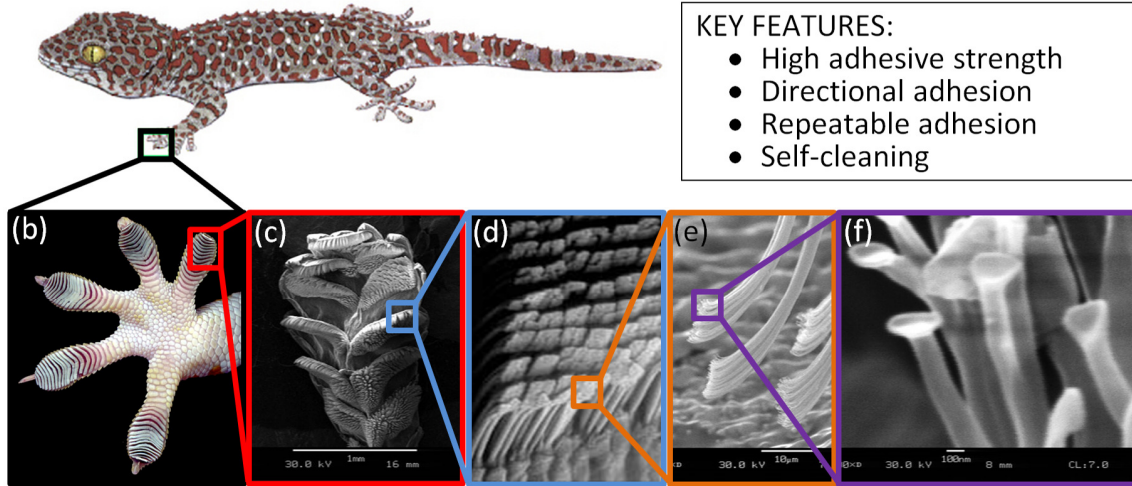


Figure 1.1: Images showing the gecko's remarkable adhesion system. (a) An image of a tokay gecko. Under each toe of a gecko (b), are neatly packed arrays of hair-like setae (c - d). Each seta branches out into finer fibrillar structures (e) that terminate in saucer-shaped spatula tips (f). Some features of the gecko's adhesion mechanism includes high adhesive strength, directionality, repeatability and self-cleaning. (Reprinted with permission from [10]. Copyright 2000)

The gecko's toe pad also possesses a remarkable adhesive strength. Studies have shown that two gecko feet (approximately  $227 \text{ mm}^2$ ) can produce up to 20.1 N of adhesive force, enough to support over ten times their body weight on a vertical surface [63]. Apart from its adhesive strength, the gecko's setae produces direction dependent adhesion, such that pulling a seta in a certain direction can yield negligible adhesion - a feature that is believed to be crucial for the gecko's ability to attach and detach from surfaces rapidly [11, 14]. In fact, a study by Autumn et al. [12] showed that the gecko is able to run across a vertical surface at speeds up to  $77 \text{ cm s}^{-1}$ .

Its fine fibrillar interface, as opposed to a continuous surface, makes the gecko's adhesion system robust to small imperfections on contacting surfaces through a mechanism known as *crack trapping* - a crack initiated on a microfiber is not directly propagated onto an adjacent

microfiber, i.e. the crack is arrested [60]. Due to the nano-scale size as well as its hierarchical structure, the effective modulus of a setae array is very low (less than 100 kPa) [13]. Low effective modulus makes the setae array compliant enough to make intimate contact with rough surfaces, thereby giving the gecko its ability to climb on irregular surfaces in various terrains. On the other hand, the high tensile strength of an individual seta allows it to withstand high stresses and support high loads without breaking. Lastly, the geckos' adhesion system has been shown to possess a self-cleaning mechanism, which is described in the following section.

### **1.3 Self-Cleaning in Geckos**

Despite the remarkably sticky nature of the gecko setae, observation of the gecko feet and setae over a period of months between molt cycles showed that it stays clean [52]. Most researchers believe that cleaning of the gecko setae occurs during normal use, but have different views on the mechanics and cleaning process. Similar to the lotus leaf [25] whose remarkable self-cleaning characteristic is as a result of micro- and nano-scale hierarchical structures on the leaf, self-cleaning in geckos has been attributed to the surface topography of the gecko feet. Hansen and Autumn [52] have shown that geckos are able to clean their contaminated feet by stepping on clean dry surfaces as can be seen in Fig. 1.2. In their work, they examined both live animals and isolated setae. Their observation of self-cleaning in an array of setae isolated from the gecko led to their conclusion that self-cleaning in geckos is intrinsic to the setal structure. Hansen and Autumn also suggested that the mechanics of self-cleaning is a “disequilibrium of energy” between the adhesive force attracting a dirt particle to the substrate and those attracting the same particle to one or more spatulae. In a later work, Hui et al. [62] suggested that the mechanism of self-cleaning in gecko may involve a rolling process due to the tendency of the contaminants to adhere to the seta compared to a non-adhesive surface. Hu et al. [58] also showed that geckos shed dirt from their feet, but through a dynamic self-cleaning mechanism labeled “digital hyperextension”. They showed analytically that when a seta is



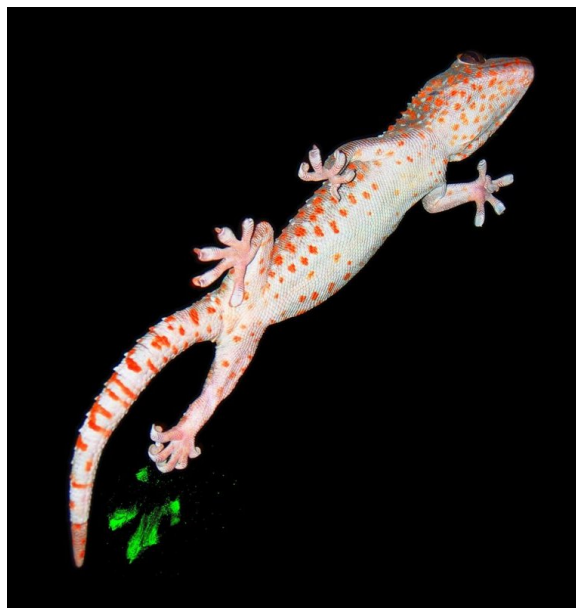


Figure 1.2: Self-cleaning in Geckos. Hansen and Autumn [52] have shown that geckos are able to clean their contaminated feet by stepping on a clean dry surface. (Printed with permission. Copyright ©2000-2008 Kellar Autumn)

suddenly released from an attached substrate, it can generate enough inertial force to dislodge dirt particles from its spatulae. Regardless of the mechanism involved, it is evident that gecko setae can self-clean, a feature that enables the gecko's adhesive system to perform excellently in various environments, and promises a broader range of application for its synthetic equivalent.

## 1.4 Introduction to Synthetic Microfiber Adhesives

Inspired by the numerous qualities of the gecko's adhesion system, researchers have been working tirelessly towards the development of synthetic fibrillar adhesives that mimics that of the gecko. The initial step towards fabrication of synthetic fibrillar adhesives was made by Sitti et al. in 2002 [122]. Using flat wax surfaces indented by an Atomic Force Microscopy (AFM) probe as a template, they molded polymer nanostructures that resulted in synthetic nano-hairs after etching away the template. The measured adhesive force of each nano-hair prototype developed was  $\approx 100$  nN. This initial attempt to make synthetic gecko adhesives was followed by

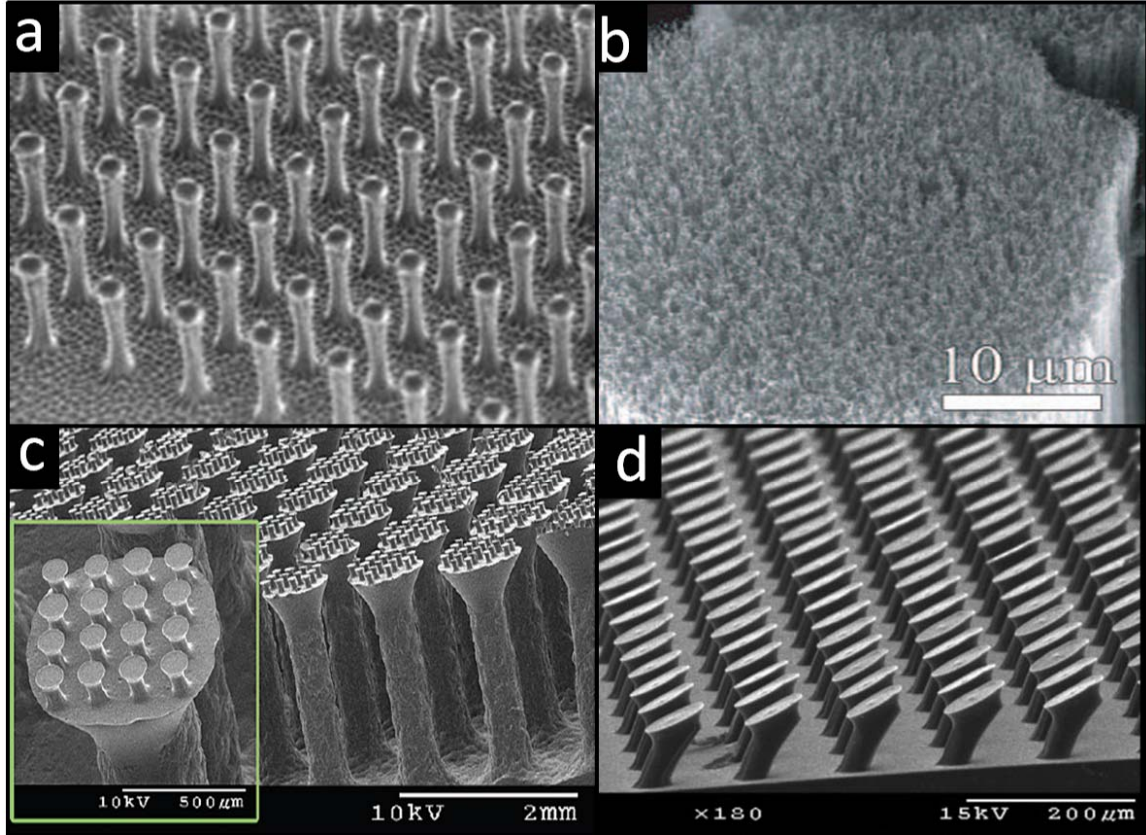


Figure 1.3: SEM images of synthetic gecko adhesives. **(a)** An array of synthetic nanopillars fabricated using oxygen plasma etching of polyimide [41]. **(b)** Image of synthetic gecko tape fabricated by transferring micropatterned carbon nanotube arrays onto a flexible polymer. The fabricated tape is reported to withstand repeated use as well as possess adhesive properties better than the natural gecko. [40]. **(c)** Array of two-level hierarchical gecko-inspired adhesives with each level terminating in flat mushroom-like tips. [104]. The microfiber stems were fabricated using DRIE techniques, while the mushroom tips were achieved by a dip-transfer soft-molding process. **(d)** Using a novel fabrication technique that incorporates lithography, molding, and dip-transfer, Murphy et al. [103] fabricated angled synthetic gecko adhesives that combine high interfacial strength of mushroom tip microfibers with directionality. (All images are reprinted with permission)

the use of other fabrication techniques to develop gecko-inspired fibrillar templates, such as:

1. Casting polymer onto a negative template created by photolithography of SU-8 [2, 28, 29, 33, 45, 46, 47, 51, 84, 102, 103, 104, 106, 126], or deep reactive ion etching (DRIE) of silicon [69, 75, 84] (Fig. 1.3a and Fig. 1.3c),
2. Hot-embossing and elongation of thermoplastic materials [67, 68, 72],
3. Thermocompression molding of thermoplastic elastomers [71],
4. Filling of porous polycarbonate membrane [88, 92, 120, 123], and
5. Growth of carbon nanotubes (CNTs) [40, 112, 140, 141] (Fig. 1.3b).

A detailed review of some of these fabrication processes has been presented by Boesel et al. [20].

To enhance compliance and improve contact with rough surfaces, researchers have also developed methods to achieve hierarchical structure (Fig. 1.3c) through micro-molding on stacked porous alumina templates [56, 64, 79, 86], shape deposition manufacturing [85], 3D laser writing [114], molding on etched silicon substrates or DRIE [69, 104], and by bundling micro-patterned carbon nanotube arrays onto flexible polymer tape [40]. After several design attempts, better adhesion of fibrillar templates compared to flat substrates was achieved by integrating large mushroom-like tips to the fibrillar structures [31, 48, 75] (Fig. 1.3d). Recently, researchers have presented fibrillar adhesives with strong adhesion in liquid, and a higher adhesive force than the natural gecko in air [87] on smooth surfaces. Control of adhesion for fibrillar adhesives has also been demonstrated using techniques such as incorporating angled microfibers [2, 69, 90, 96, 102, 103, 106, 119, 126], thermally-responsive microfibers made with shape memory polymer (SMP) [77, 113], design of microfibers with anisotropic geometry [81], and varying pull-off speed [1, 78].

Overall, significant progress has been made towards the development of synthetic gecko-inspired fibrillar adhesives with similar characteristics as that of the gecko except for its self-cleaning abilities. A cleaning feature is greatly desired for synthetic gecko adhesives whose

use is currently restricted to clean environments. The need for a thorough understanding of the mechanisms of cleaning, leading to the design of synthetic gecko adhesives with easy cleaning and anti-fouling capabilities, is the motivation for this work.

## **1.5 Applications of Microfiber Adhesives**

The advantages and unique characteristics of microfiber adhesives promises an extensive range of application both in areas where conventional adhesives are being used, and in new areas where the use of conventional adhesives is impossible. For example, the clean adhesion mechanism of microfiber adhesives allows its use in cleanroom environments where conventional adhesives cannot be used due to residual contaminants. Furthermore, the ability of microfiber adhesives to function in air, water and vacuum, expands the current areas of use for this category of adhesives. In this section, we discuss the various areas of application of microfiber adhesives.

### **Medical Applications**

Gecko inspired microfiber adhesives are already finding use in medical devices. Synthetic gecko adhesives can be attached to the legs of active endoscopic capsules as presented by Cheung et al. [26] to provide strong attachment to the walls of the esophagus sufficient to withstand peristaltic forces (Fig. 1.4b). Researchers have also demonstrated the use of microfiber adhesives as a medical skin patch [82, 91]. In their publication, Kwak et al. [82] showed that, compared to traditional acrylic adhesives, gecko-inspired adhesives allowed better air circulation to the skin and peeled away more easily, reducing skin irritation in patients (Fig. 1.4a).

### **Industrial Applications**

The use of microfiber adhesives for object manipulation has been demonstrated by several research groups and is currently an area of significant interest to the fibrillar adhesion com-

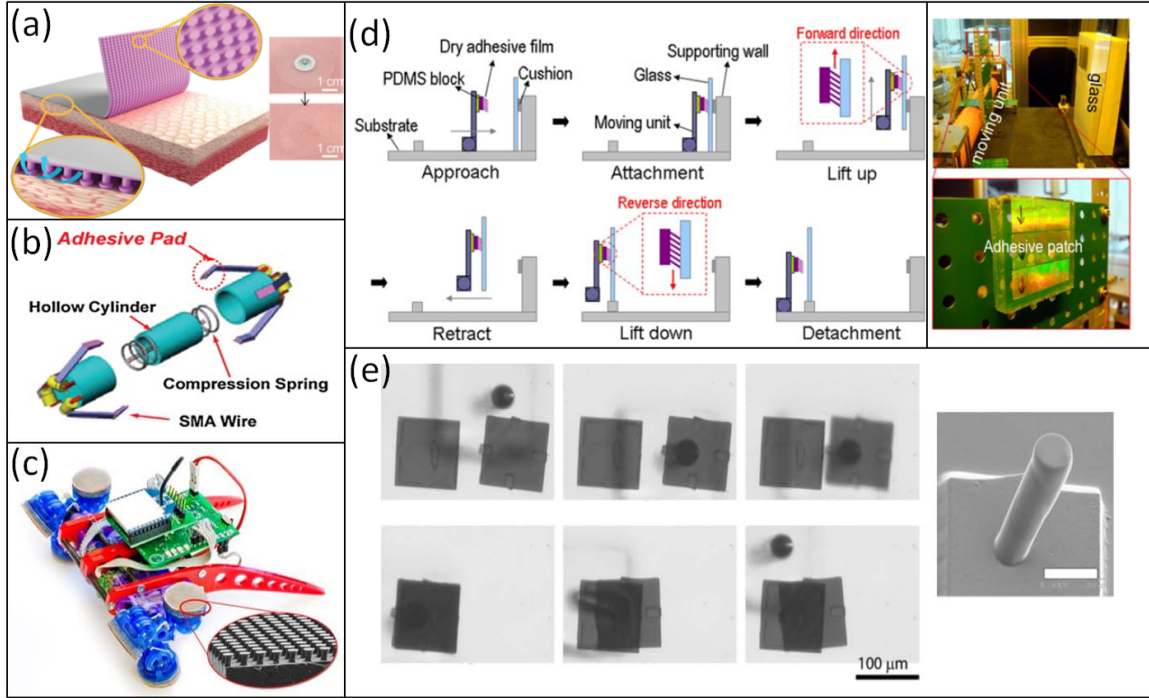


Figure 1.4: Images showing some applications of fibrillar adhesives. **(a)** Using high-density, mushroom-like micropillars, Kwak et al. developed a medical skin patch that allows better air circulation to the skin, leading to reduction in skin irritation when compared to acrylic adhesives [82]. **(b)** An endoscopic microcapsule designed using synthetic fibrillar adhesives for enhanced traction and locomotion within the digestive tract [26]. **(c)** Waalbot II - An untethered wall climbing robot that is able to climb on smooth vertical surfaces at speed up to 5 cm/s, using fibrillar adhesives [101]. **(d)** Jeong et al. demonstrated the use of angled fibrillar adhesives patch for the clean transport of LCD glass [69]. **(e)** Menguc et al. showed the use of manipulators with a single angled elastomer micropillar to transport micrometer-scale silicon microplatelets from one location to another [96]. (All images are reprinted with permission)

munity. Utilizing directional, preload, shear, and rate dependences of fibrillar adhesives, researchers have demonstrated the use of fibrillar adhesives attached to manipulators to pick and release micro objects, with an attachment to detachment force ratio of up to 1000:1 (Fig. 1.4e) [78, 96, 138]. This feature has been harnessed for clean transfer printing in LCD glass manufacturing (Fig. 1.4d) [69].

### **Mobile Robots**

Because the natural use of the gecko's adhesive is for locomotion, the use of gecko-inspired adhesives for mobility is not far fetched. Using fibrillar adhesives in wall climbing robots was one of its first applications (Fig. 1.4c) [100, 101]. Since then, fibrillar adhesives have been used in other mobile robots such as the highly actuated Stickybot with morphology similar to that of the actual gecko [73].

### **Other Applications**

Due to its characteristics, gecko adhesives can find applications in other areas such as space exploration, in household appliances (i.e. non-destructive and detachable wall hangers), gripping gloves (i.e. by soccer goalkeeper) and for traction enhanced shoes (i.e. hiking shoes).

## **1.6 Research Objectives**

Inspired by the self-cleaning characteristics of the gecko's adhesion system and its benefits, the goal of this thesis is the development of design parameters that will lead to the fabrication of gecko-inspired microfiber adhesives with anti-fouling and self-cleaning features. To achieve this goal, mechanisms of contact self-cleaning and anti-fouling of microfiber adhesives are proposed and models describing these mechanisms are developed. The developed model will also show light into the mechanism of self-cleaning in the natural gecko's system. We will conduct detailed experiments of contact self-cleaning of microfiber adhesives to study the

proposed mechanisms and to gain insight on the mechanics involved. From the model and experiments, we investigate several parameters that are necessary to promote contact self-cleaning and anti-fouling of microfiber adhesives. Finally, design considerations are given for the design of microfibers with contact self-cleaning and anti-fouling characteristics for use in various environments.

Thus, the main objectives of this thesis are:

- Unveiling the processes, procedures and mechanisms of contact self-cleaning of gecko-inspired microfiber adhesives
- Modeling the mechanics of contact self-cleaning of microfiber adhesives
- Obtaining underlying parameters that influence contact self-cleaning and anti-fouling of microfiber adhesives
- Providing insight into design factors that can be implemented to achieve self-cleaning and anti-fouling of microfiber adhesives

With this background, we present a model of adhesion for an array of microfiber adhesives in Chapter 2. We also model the rate dependence of adhesion for microfiber adhesives. The developed adhesion model is used in modeling the mechanics of contact self-cleaning presented in Chapter 3. In Chapter 3, we also report the mechanisms, processes, procedures of achieving self-cleaning in microfiber adhesives. Experiments of contact self-cleaning of microfiber adhesives are carried out and analyzed in Chapter 4. A method for simulating contact self-cleaning is also introduced along with the simulation results. In Chapter 5, design considerations for microfiber adhesives with enhanced contact self-cleaning and anti-fouling capabilities are given based on environmental and application considerations. This thesis work is summarized and an outlook is reported in Chapter 6.

## **1.7 Expected Contributions**

The major contributions of this work is the development of the mechanics of contact self-cleaning for microfiber adhesives and unveiling of critical factors that serves as a guideline for the design of microfiber adhesives with contact self-cleaning and anti-fouling capabilities. The effects of contaminant size, microfiber geometry, and loading conditions to contact self-cleaning are presented. We will consider various cleaning procedures and mechanisms, and conduct experiments to uncover the underlying mechanism of contact self-cleaning.

In summary, this thesis provides contributions to the following areas of gecko-inspired microfiber adhesives:

### **Adhesion Modeling of Microfiber Adhesives**

- An improved adhesion model for microfiber adhesives.
- Modeling of the load-deformation relationship for microfiber adhesives under a spherical indenter.
- Modeling and experimentation of the loading rate dependence of adhesion of microfiber adhesives.

### **Dry-Contact Cleaning of Microfiber Adhesives**

- Definition of self-cleaning for microfiber adhesives.
- An in-depth study of the processes, mechanisms and procedures of contact self-cleaning of microfiber adhesives.
- Modeling of the mechanics of contact self-cleaning of microfiber adhesives.
- Experimentations of contact self-cleaning of microfiber adhesives
- Simulations of contact self-cleaning of microfiber adhesives.
- Design considerations for microfiber adhesives with enhanced contact self-cleaning and



anti-fouling capabilities, based on application environment and procedure.

## **Chapter 2**

# **Adhesion of Gecko-Inspired Microfiber Adhesives**

### **2.1 Introduction**

The goal of this chapter is to develop a model of adhesion that will be used later in studying the mechanics of dry-contact cleaning of microfiber adhesives. Although there have been significant works in adhesion modeling for fibrillar adhesives, previous models have failed to take into account some of the factors that contribute to the adhesive force of a fibrillar adhesive. The adhesive force of a fibrillar interface has been shown to depend on several key factors including the microfiber geometry, microfiber spacing, the effective modulus of the microfiber, the work of adhesion of the contact interface, the thickness and material properties of the backing layer, the preload force, the retraction speed at which the adhesive is pulled away from a contacting substrate, and the shape of the contacting substrate. Most of the previous models, especially those that considered contact with spherical surfaces, failed to take some of these factors into consideration. Lee and Fearing [88] modeled the adhesive force of their high aspect ratio fibrillar adhesives with spherical contaminants; but in their model, the adhesive force for a single sphere was taken as the sum of the adhesive forces of individual contacting microfibers. A

similar approach was also taken by Hansen and Autumn for adhesion of the natural gecko setae with spherical particles [52]. Both groups assumed that all the contacting microfibers break off from the substrate simultaneously, which is not the case for a spherical indenter. Their models also neglected the effect of the preload force which plays a crucial role in the adhesion of spheres with fibrillar adhesives. Hui et al. [62] also developed a model of self-cleaning and anti-fouling with cylindrical rods as contaminants. Hui et al. assumed that the contaminant was centrally aligned to a microfiber in the array. In their model, the adhesive force was the sum of forces acting on contacting microfibers, when the load on the center microfiber is zero. Their assumption that the critical pull-off force occurs when the indentation distance of the particle is zero does not correlate with experimental observations. Their model also assumed a uniform backing layer displacement and did not take into account the effect of the preload force. A more accurate adhesion model for contact with spherical surfaces was presented by Aksak et al. [2]. In their model, they simulated the indentation and retraction of a sphere from a fibrillar adhesive, and obtained the adhesive force from the simulation results. However, a uniform deformation of the backing layer was assumed, and the sphere was positioned directly on top of a single microfiber during the simulation. An analytically detailed model of adhesion of fiber array was also developed by Majidi et al. [93], however, the model was for high aspect ratio gecko inspired adhesives, where the fibers are highly compliant and adhesion is achieved through side contact.

In Section 2.2, we develop a new model of adhesion for a single microfiber adhesive and expand the model for a microfiber adhesives array in contact with flat and spherical surfaces in Section 2.3. In Section 2.4, we model the effect of retraction speed on the adhesive force of a single microfiber adhesive. Increasing the speed at which the fibrillar adhesive is pulled away from a contacting substrate has been shown to enhance adhesive force by several orders of magnitude [50, 78, 111]. Known as the *retraction speed effect*, this behavior has been attributed to the viscoelastic material properties of the fibrillar adhesives [24], and in another work, solely

to the *mechanical behavior* of the interface [38]. Until now, no work has been done to show the mechanics behind the retraction speed effect for fibrillar adhesives experimentally, or theoretically. We will investigate crack propagation at the interface of a cylindrical micro-post and a smooth substrate, and study the critical crack propagation speed at which the maximum tensile force (adhesive force) was measured. The Chapter summary is presented in Section 2.5.

## 2.2 Adhesive Force of a Single Elastomeric Microfiber

To model the adhesive force of a microfiber array, we will begin with analyzing and modeling the load-deformation relationship of an individual microfiber. Figure 2.1 shows a schematic of a single elastomer microfiber adhesive under compressive normal load. In the model, we assume that both the microfiber tip and contacting substrate are atomically smooth and make perfect contact so that the effect of surface roughness is neglected. The model will be developed in 3 steps:

- Using the flat punch theory, we will obtain the adhesive strength and pull-off force of the microfiber,
- With the classical beam theory, we will obtain the relationship between applied load and the deformation of the microfiber and underlying substrate
- We will combine the cylindrical flat punch theory and the beam theory to obtain the load-deformation curve of a single adhesive microfiber

Maugis [94] has shown that the adhesive force  $F_c$  of a cylindrical flat punch in contact with a flat surface is given by

$$F_c = \sqrt{6\pi a_t^3 K w} \quad (2.1)$$

where  $w$  is the work of adhesion of the contact interface,  $a_t$  is the radius of the microfiber tip, which is the same as the microfiber stem radius in the case of a flat punch, and  $K$  is the reduced

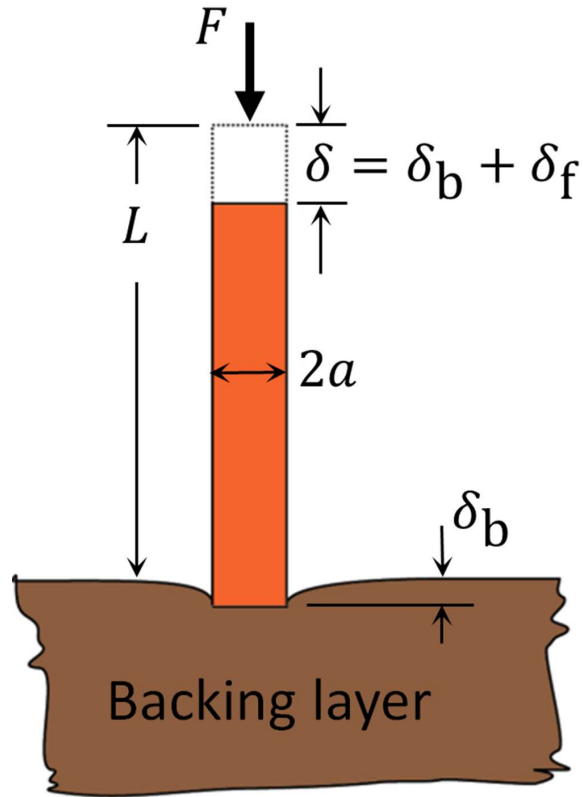


Figure 2.1: Schematics of loading and deformation of a single microfiber and backing layer (the deformation of the backing layer in this diagram is exaggerated). The microfiber is modeled as a soft cylindrical flat punch.

elastic modulus of the contact interface given as

$$\frac{1}{K} = \frac{3}{4} \left( \frac{1 - \nu_s^2}{E_s} + \frac{1 - \nu_f^2}{E_f} \right) \quad (2.2)$$

here,  $\nu_s$  and  $\nu_f$  are the Poisson's ratios, and  $E_s$  and  $E_f$  are the Young's moduli of the substrate and microfiber materials, respectively. Although Equation 2.1 was developed for a rigid cylindrical flat punch in contact with a soft frictionless elastic surface, it is a good first order approximation for the case of a soft elastic punch in contact with a rigid surface [2, 127].

To obtain the deformation of a single microfiber under normal load, the microfiber is modeled as a fixed-fixed cylindrical column. We will assume that the tip of the microfiber remains parallel to the substrate during loading or unloading until the microfiber buckles or pulls off. Under normal loading conditions, the microfiber stem deformation  $\delta_f$  for an applied normal load  $F$  can be obtained using a linear spring model as

$$\delta_f = C_f F \quad (2.3)$$

where  $C_f = L / (\pi a^2 E_f)$  is the compliance of the microfiber stem, and  $L$  is the initial length of the microfiber. Deformation also occurs at the backing layer. The backing layer deformation  $\delta_b$  due to  $F$  can be obtained from Maugis' flat punch model [94] as

$$\delta_b = C_b F, \quad (2.4)$$

where  $C_b = 2 / (3aK)$  is the compliance of the backing layer. The total deformation of a single microfiber  $\delta$  which includes the backing layer deformation is a sum of  $\delta_f$  and  $\delta_b$ , i.e.  $\delta = \delta_f + \delta_b$ ; and the overall microfiber compliance  $C$  is given as

$$C = \frac{L}{\pi a^2 E_f} + \frac{2}{3aK}. \quad (2.5)$$

It is important to note that for a microfiber with very thin or rigid backing layer, the value of  $\delta_b$  becomes negligible. The load-deformation equation for a single adhesive microfiber can thus be given as

$$\delta = \left( \frac{L}{\pi a^2 E_f} + \frac{2}{3aK} \right) F. \quad (2.6)$$

It is also important to note that Equation 2.6 is valid for compressive load until buckling occurs. The critical deformation for buckling to occur  $\delta_{cr}$  is given as

$$\delta_{cr} = CF_{cr} \quad (2.7)$$

where  $F_{cr}$  is the buckling load obtained from Euler's buckling formula for a fixed-fixed beam, given as

$$F_{cr} = -\frac{\pi^3 E_f a^4}{L^2}. \quad (2.8)$$

For a buckled microfiber, the normal load acting on the microfiber is approximated as  $F_{cr}$ .

The maximum tensile deformation  $\delta_c$  of the microfiber before it detaches from the contacting substrate can be expressed as

$$\delta_c = CF_c. \quad (2.9)$$

## 2.3 Adhesive Force of a Microfiber Array

Now that we have successfully modeled the load-deformation behavior of a single microfiber, we can go on to derive a model for an array of microfibers. The adhesive force of a microfiber array will be dependent not only on the adhesive force of each microfiber in the array, but also on other parameters such as the microfiber packing (or arrangement pattern), microfiber spacing, indentation depth (or the corresponding preload force), and the shape of the indenter.

Intuitively, one might like to maximize the number of microfibers in an array in order to increase the overall adhesive force. However, the density of microfibers in a given array is limited

due to adhesive interactions between adjacent microfibers. When in close proximity, microfibers become stuck to each other, lowering their adhesion performance. This phenomenon is known as *lateral collapse* or *fiber clumping*. Previous work by Glassmaker et al. [47] showed that the lateral stability between adjacent cylindrical microfibers requires;

$$\left(\frac{\pi^4 E_f^* a}{2^{11} \gamma_f}\right)^{1/12} \left(\frac{3 E_f a^3 S^2}{\gamma_f}\right)^{1/4} > L, \quad (2.10)$$

where  $E_f^* = E_f/(1 - \nu_f^2)$ ,  $\gamma_f$  is the surface energy of the microfiber material, and  $S$  is the edge-to-edge distance between the microfibers.

For simplification, we will make the following assumptions for our microfiber array:

- All microfibers in the array have the exact same geometry. This includes microfiber height, radius and tip shape.
- All microfibers have similar material properties. i.e. similar values of Young's modulus, surface energy, etc.
- Microfibers are axially symmetric
- The indenter surface is perfectly aligned to the microfiber array, such that there are no misalignment effects.
- The surface of the indenter as well as the microfiber tip are atomically smooth.

### 2.3.1 Adhesion with a Flat Surface

For a microfiber array indented by a flat probe, all the microfibers within the contact area make contact and pull-off simultaneously. The adhesive force between the array  $P_c$  and the indenter is given as

$$P_c = N_f F_c, \quad (2.11)$$



where  $F_c$  is the adhesive force of individual microfibers, and  $N_f = \rho A$  is the number of microfibers in contact with the indenter, and  $A$  is the apparent contact area between the microfiber array and the indenter. Here, the microfiber density  $\rho$  is the number of microfibers per unit area of the pad, and is a function of the spacing between adjacent microfibers and the microfiber packing pattern. I.e.,

$$\rho = \begin{cases} 1/d^2 & \text{for square packing,} \\ \frac{2\sqrt{3}}{3d^2} & \text{for hexagonal packing,} \end{cases} \quad (2.12)$$

where  $d = S + 2a$  is the distance between the centers of adjacent microfibers. The adhesive strength  $p_c$  of the array can then be obtained as

$$p_c = \frac{P_c}{A} = \rho F_c. \quad (2.13)$$

### 2.3.2 Adhesion with a Spherical Surface

Spherical indenters are considered a special type of rough surfaces. The use of spherical indenters eliminates misalignment errors present in experiments with flat indenters, and as a result, they are preferred and widely used in adhesion experiments. In this work, we will assume that the sphere radius  $R$  is significantly larger than the microfiber tip radius, such that there is a full contact between the microfiber tips and the indenter surface, so that the flat punch theory in Eqn. 2.1 is valid. A schematic of an adhesive microfiber array indented by a spherical surface is shown in Figure 2.2.

A typical adhesion measurement using a spherical probe involves a loading step during which the probe is pressed against the microfiber array until a desired indentation depth or compressive load is reached. This is followed by an unload step during which the probe is pulled away from the microfiber array until all previously contacting microfibers have lost contact. The maximum compressive force during loading is referred to as *preload*. The adhesive force (also known as the *pull-off* force) is recorded as the maximum tensile force during the unloading

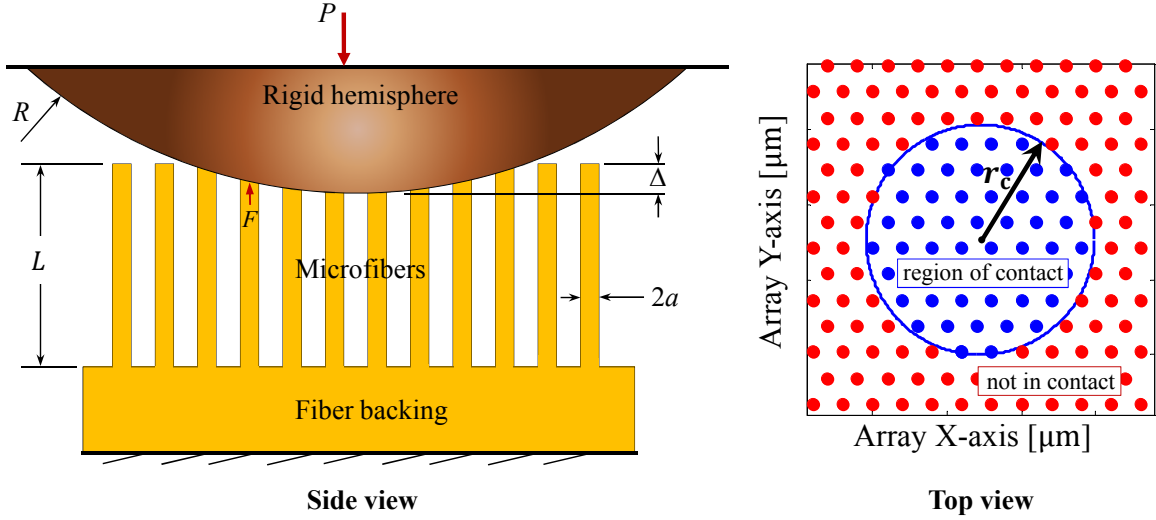


Figure 2.2: Schematics of loading and deformation of a microfiber array by a spherical indenter showing the top and side view.  $L$  is the microfiber length,  $a$  is the microfiber radius,  $R$  is the radius of curvature of the indenter,  $\Delta$  is the indentation depth, and  $r_c$  is the apparent contact radius of the interface. (The deformation of the microfiber backing is not shown).

step.

**Derivation of Load-Deformation Relationship for a Spherical Surface:** The force  $P$  exerted by a spherical indenter on a microfiber array during loading, is the sum of the individual reaction forces,  $F$  exerted by each contacted microfiber on the indenter, i.e.,  $P = \int F dN$ . By substituting  $F = \delta/C$ , the applied normal load can be rewritten as

$$P = \int \frac{1}{C} \delta dN, \text{ for all contacting microfibers.} \quad (2.14)$$

Given the indenter radius, the indentation distance  $\Delta$ , and the radial distance from the center of the sphere to the center of the microfiber  $r$ , the deformation of a single microfiber can be obtained from geometric analysis as

$$\delta = \Delta - R + \sqrt{R^2 - r^2}, \quad (2.15)$$

which after expanding  $\sqrt{R^2 - r^2}$  becomes

$$\delta = \Delta - \frac{r^2}{2R} - \frac{r^4}{8R^3} + O(r^5) \quad (2.16)$$

For  $R \gg r$ , we can drop the  $r^4$  term and up, so that

$$\delta = \Delta - \frac{r^2}{2R}. \quad (2.17)$$

The number of microfibers in contact with the sphere within a radial distance  $r$  from the center of the sphere, can be obtained as  $N_f(r) = \rho\pi r^2$ , so that

$$dN_f = 2\pi r \rho dr. \quad (2.18)$$

Substituting Eq. 2.17 and Eq. 2.18 into Eq. 2.14, and integrating from  $r = 0$  to  $r_c$ , where  $r_c$  is the apparent contact radius of the indenter, we have

$$\begin{aligned} P &= \int_0^{r_c} \frac{1}{C} \left( \Delta - \frac{r^2}{2R} \right) 2\pi r \rho dr \\ &= \pi \rho \frac{r_c^4}{4CR}. \end{aligned} \quad (2.19)$$

For  $R \gg r_c$ ,  $\Delta$  is equal to  $r_c^2/2R$ , similar to equation 2.17 with  $\delta = 0$  when  $r = r_c$ . So that we obtain  $P$  in terms of  $\Delta$  as

$$P = \frac{1}{C} \pi \rho R \Delta^2. \quad (2.20)$$

Equations 2.19 and 2.20 gives the contact radius and the indentation depth of the indenter, respectively, for a given preload value  $P$ .

**Numerical Simulation of Load-Deformation for a Spherical Surface:** Numerical simulations can also be used to find the value of  $\Delta$  for a given  $P$ . A Matlab routine was developed

to obtain the indentation distance of a spherical indenter for a specified microfiber geometry. A flowchart of the simulation is shown in Fig. 2.3, and details of the simulation steps can be found in Appendix A.1.

**Adhesive Force of a Microfiber Array with a Spherical Surface:** The adhesive force between the microfiber array and the spherical indenter is obtained from a numerical simulation of both the loading and unloading steps. To achieve this, we first obtain the indentation distance  $\Delta_p$  for the desired preload force  $P_p$  from Eqn. 2.20 or using the simulation routine shown in Fig 2.3. The apparent contact area  $A_{\max}$  at  $\Delta_p$  is also obtained.

Secondly, we simulate loading by gradually increasing the indentation distance from  $\Delta = 0$  to  $\Delta_p$  and recording the normal load  $P(\Delta)$  for each value of  $\Delta$ . Next, we simulate unloading by decreasing the indentation distance in very small decrements of  $d\Delta$  and recording the value of  $P$  after each retraction step, until all initially contacting microfibers are detached. During unloading, the microfibers are allowed to stretch until they reach a critical deformation given in 2.9 at which the microfibers break contact with the probe. Finally the adhesive force is obtained as the maximum tensile force recorded during the unloading cycle. For this purpose, it is important to select a small value of  $d\Delta$ . The adhesive strength of the array is obtained by dividing the adhesive force by the maximum contact area as

$$p_c = \frac{P_c}{A_{\max}}. \quad (2.21)$$

Figure 2.4 shows a graph of  $P$  plotted against  $\Delta$  for a loading and unloading simulation of a microfiber array with  $L = 100 \mu\text{m}$ ,  $a = 12.5 \mu\text{m}$ ,  $d = 90 \mu\text{m}$ ,  $E_f = 2.9 \text{ MPa}$ ,  $\nu_f = 0.49$ , and  $w = 96 \text{ mJ/m}^2$ ; indented by a sphere of  $R = 6 \text{ mm}$ ,  $E_s = 73 \text{ GPa}$ , and  $\nu_s = 0.17$  with a preload force  $P_p = 4.46 \text{ mN}$ . In the graph, compressive force is positive, while tensile force is negative. The preload force is the maximum (compressive) force recorded, while the adhesive force is the minimum force (maximum tensile force) recorded. An adhesive force of  $P_c = 3.58$

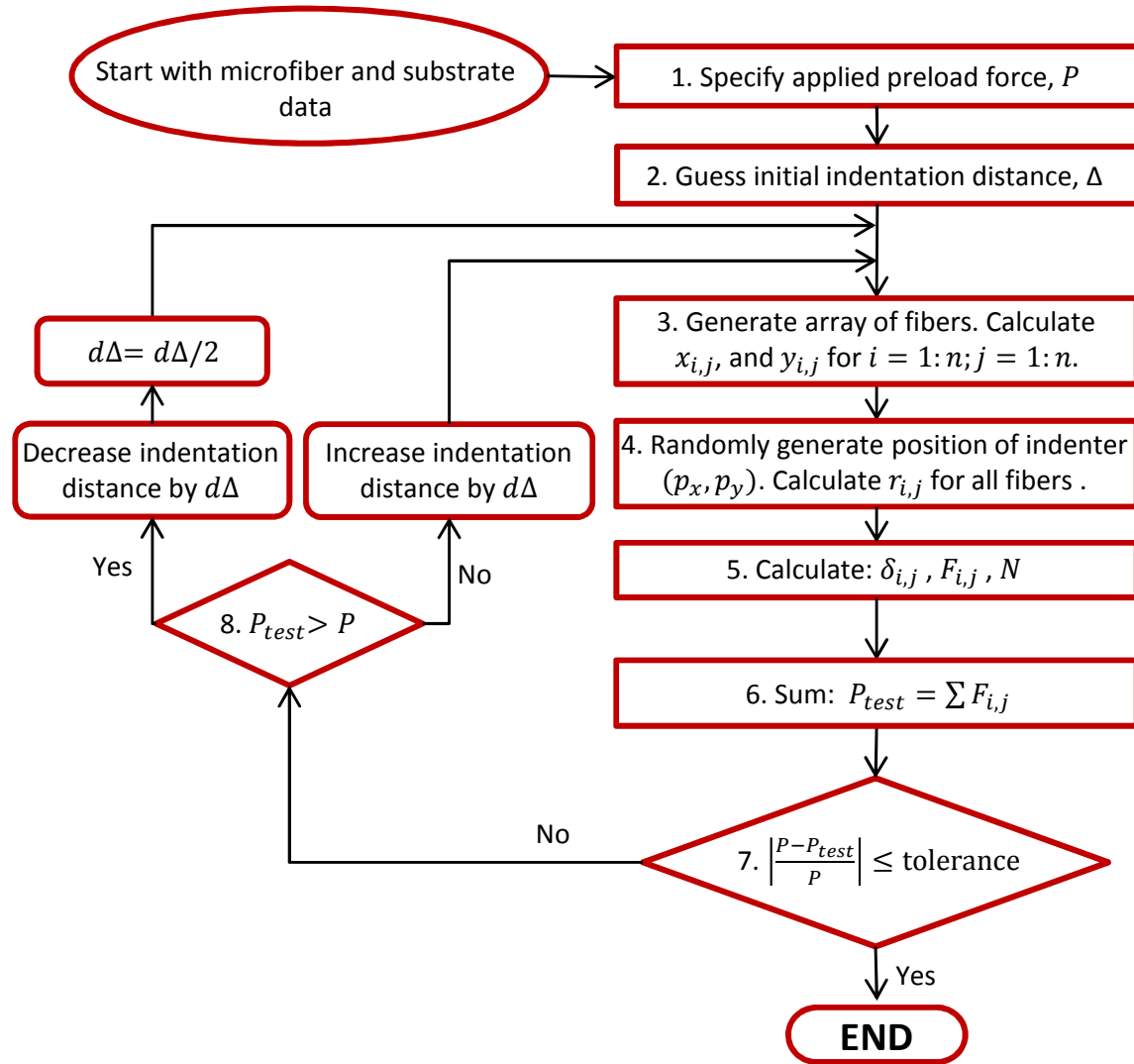


Figure 2.3: Flowchart for finding the indentation distance  $\Delta$  of a spherical indenter of radius  $R$  for a given normal load  $P$ .  $r_{i,j}$ ,  $\delta_{i,j}$ , and  $F_{i,j}$  are the radial distance from the center of the sphere, the indentation distance and the reaction force, respectively, of a microfiber in row  $i$  and column  $j$ .  $(p_x, p_y)$  are the  $x$  and  $y$  coordinates of the indenter in the microfiber array.  $N_f$  is the number of microfibers in contact with the substrate.  $P_{test}$  is the estimated preload obtained from each iteration. This routine is valid for compressive load only.

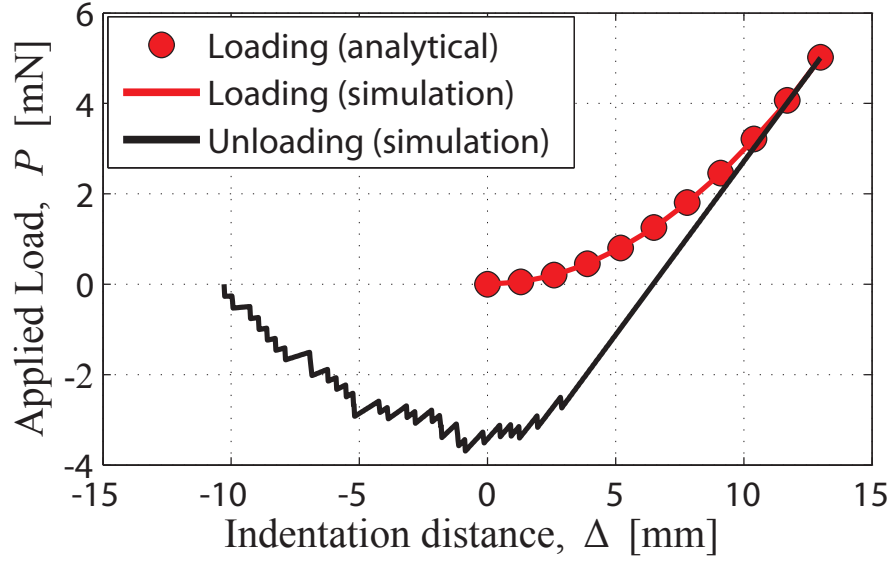


Figure 2.4: Graph of load plotted against indentation distance for a single loading and unloading simulation cycle. The value of  $\Delta$  is gradually increased until the desired preload force is reached. Afterwards,  $\Delta$  is reduced until all initially contacting microfibers are pulled off. The graph is for a microfiber array of  $L = 100 \mu\text{m}$ ;  $a = 12.5 \mu\text{m}$ ; and  $d = 90 \mu\text{m}$ , indented by a sphere of  $R = 6 \text{ mm}$  with a preload force  $P_p = 5 \text{ mN}$ . In this plot, compressive force is positive, while tensile force is negative. The preload force is the maximum compressive force, and the adhesive force is the maximum tensile force obtained during a loading and unloading cycle. The perturbations in the unloading curve is due to the detaching of microfibers in the array.

Parameter	Values				
Fiber radius, $a$ [ $\mu\text{m}$ ]	7.5	10	<b>12.5</b>	15	17.5
Length, $L$ [ $\mu\text{m}$ ]	25	50	75	<b>100</b>	125
Young's modulus, $E_f$ [MPa]	<b>3</b>	10	50	100	500
Spacing, $S$ [ $\mu\text{m}$ ]	<b>15</b>	20	25	30	35
Sphere radius, $R$ [mm]	0.5	1	1.5	<b>2</b>	2.5
Work of adhesion, $w$ [mJ/m <sup>2</sup> ]	40	65	80	<b>95</b>	110

Table 2.1: Simulated parameter values used to study the effects of microfiber length, microfiber radius, microfiber Young's modulus, microfiber spacing, interface work of adhesion, indenter radius, and preload force on adhesion. The value highlighted for each parameter is the default value used when testing other parameters

mN was obtained in this simulation.

### 2.3.3 Results and Discussions

We now go on to investigate the effect of the microfiber length, microfiber radius, microfiber Young's modulus, microfiber spacing, interface work of adhesion, indenter radius, and preload force on adhesion. We conduct our investigation for an array indented by a sphere only since the results for a flat indenter can be directly obtained from Equations 2.11 and 2.13. The various parameter values simulated are listed in Table 2.1 (value highlighted for each parameter is the default value used while testing other parameters). For each parameter value listed, several simulations are conducted for various preload force  $P_p$  values of 0.1, 0.25, 0.5, 0.75, 1, 1.5, 2, 2.5, 5, 3.5, 4, and 5 mN.

#### Effect of Preload Force

To study the effect of preload force, we varied the preload applied in our simulation from 0.1 mN to 5 mN, while keeping the microfiber and indenter properties constant. As we increase the preload force in the simulation, we expect an increase in  $\Delta_p$  which will lead to an increase in  $N$ , and ultimately an increase in the adhesive force. This expected outcome is observed in

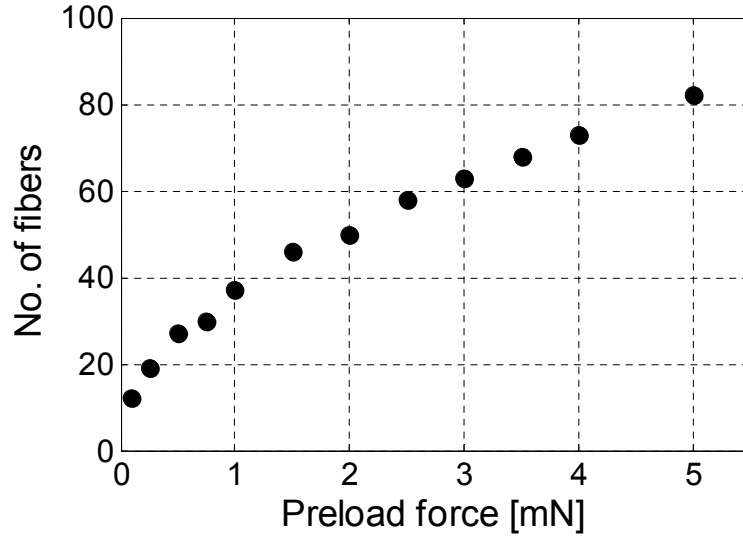
Fig. 2.5. Figure 2.5a is a graph of  $N$  plotted against  $P_p$ , and Fig. 2.5b is a graph of  $P_c$  plotted against  $P_p$ . The graphs show a direct proportionality between  $P_p$  and  $N$ . The simulation result also shows increase in  $P_c$  as  $P_p$  is increased. The increase in adhesive force tend to plateau as for higher values of  $P_p$ . This trend is expected since the effect of preload force is limited by several factors such as the microfiber length, spacing, indenter radius, etc, as we will see in the rest of this section.

### Effect of Microfiber Radius

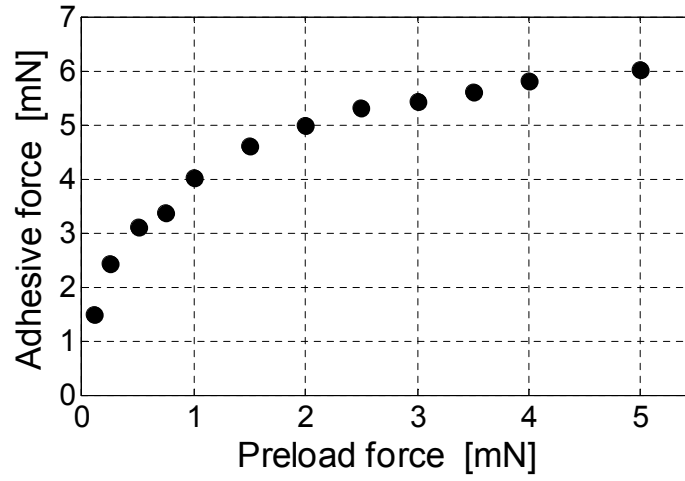
To study the effect of microfiber radius, we varied the radius of the microfibers from  $7.5\mu\text{m}$  to  $17.5\mu\text{m}$  while other parameters were kept constant. For each microfiber radius, adhesion simulation were performed for preload forces ranging from 0.1 mN to 5 mN. As we increase the microfiber radius, we expect the adhesive force of individual microfibers to increase according to Equation 2.1. On the other hand, an increase in the microfiber radius will lead to an increase in the effective stiffness of the microfiber array, thereby decreasing the number of microfibers in contact with the indenter for a given preload. Two cases dependent on microfiber-to-fiber spacing were studied.

In the first case, the center-to-center distance of the microfiber was kept constant at  $d = 40\mu\text{m}$  while the microfiber radius was changed. The result for this case is shown in Fig. 2.6. Figure 2.6a shows a plot of  $P_c$  against  $P_p$  for various values of  $a$ , while Fig. 2.6b shows a plot of  $P_c$  against  $a$  for various values of  $P_p$ . Results from the graph show an increase in adhesive force for larger microfiber radius. Evidently in this case, the positive effect of an increase in adhesive force of individual microfiber outweighs the negative effect of increasing the microfiber stiffness. The result also shows a stronger dependence on preload for microfibers with a large radius compared to microfibers with a small radius. For a  $17.5\mu\text{m}$  radius, the adhesive force goes from 2 mN to 8.5 mN - order of 4, whereas for a  $7.5\mu\text{m}$  radius the adhesive force goes from 1.3 mN to 4 mN - order of 3, as  $P_p$  is increased from 0.1 mN to 5 mN. Such a





(a)



(b)

Figure 2.5: Effect of preload force on adhesion. Simulation results for a microfiber array of  $a = 12.5 \mu\text{m}$ ;  $L = 100 \mu\text{m}$ ;  $S = 15 \mu\text{m}$ ;  $E_f = 2.9 \text{ MPa}$ ;  $\nu_f = 0.49$ ; and  $w = 96 \text{ mJ/m}^2$ , indented by a sphere of  $R = 2 \text{ mm}$ ;  $E_s = 73 \text{ GPa}$ ; and  $\nu_s = 0.17$ . **(a)** Graph of  $N$  plotted against  $P_p$ . **(b)** Graph of  $P_c$  plotted against  $P_p$ . The graphs shows an increase in the number of contacting microfibers, and the adhesive force as the preload force is increased.

response to preload indicates that the use of preload to achieve adhesion control is favored for larger microfibers compared to smaller microfibers.

For the second case, the edge-to-edge distance between adjacent microfibers was kept constant at  $S = 15\mu\text{m}$  while the microfiber radius was changed. Result for this case is shown in Fig. 2.7. Figure 2.7a shows a plot of  $P_c$  against  $P_p$  for various values of  $a$ , while Fig. 2.7b shows a plot of  $P_c$  against  $a$  for various values of  $P_p$ . In this case, there is a negative effect on adhesion by increasing microfiber radius. This negative trend is more pronounced as the preload force is increased (See Fig. 2.7b for  $P_p = 5\text{ mN}$ ). Compared to the previous case, the adverse effect on array stiffness and consequently on the number of contacting microfibers is more significant and less compensated by the increase in the adhesive force of individual microfibers.

### Effect of Microfiber Length

To study the effect of microfiber length, we varied the length of the microfibers from  $25\mu\text{m}$  to  $125\mu\text{m}$  while other parameters were kept constant. For each length, adhesion simulation were performed for preload forces ranging from 0.1 mN to 5 mN. An increase in the length of the microfiber will reduce the stiffness of the array. As a result, more microfibers are expected to make contact with the indenter, thereby increasing adhesion. Results of the simulations are shown in Fig. 2.8. Figure 2.8a is a graph of  $P_c$  plotted against  $P_p$  for various values of  $L$ , and Fig. 2.8b is a graph of  $P_c$  plotted against  $L$  for various values of  $P_p$ . The graphs show a direct proportionality between the adhesive force and microfiber length. Increasing the length of microfiber for fibrillar adhesive is limited by *lateral collapse*, a phenomenon discussed earlier in this chapter. The graphs also show a high to low adhesion ratio of 4.1 for  $L = 125\mu\text{m}$  and 2.2 for  $L = 25\mu\text{m}$ , which suggests that adhesion control using preload force is enhanced for longer microfibers.

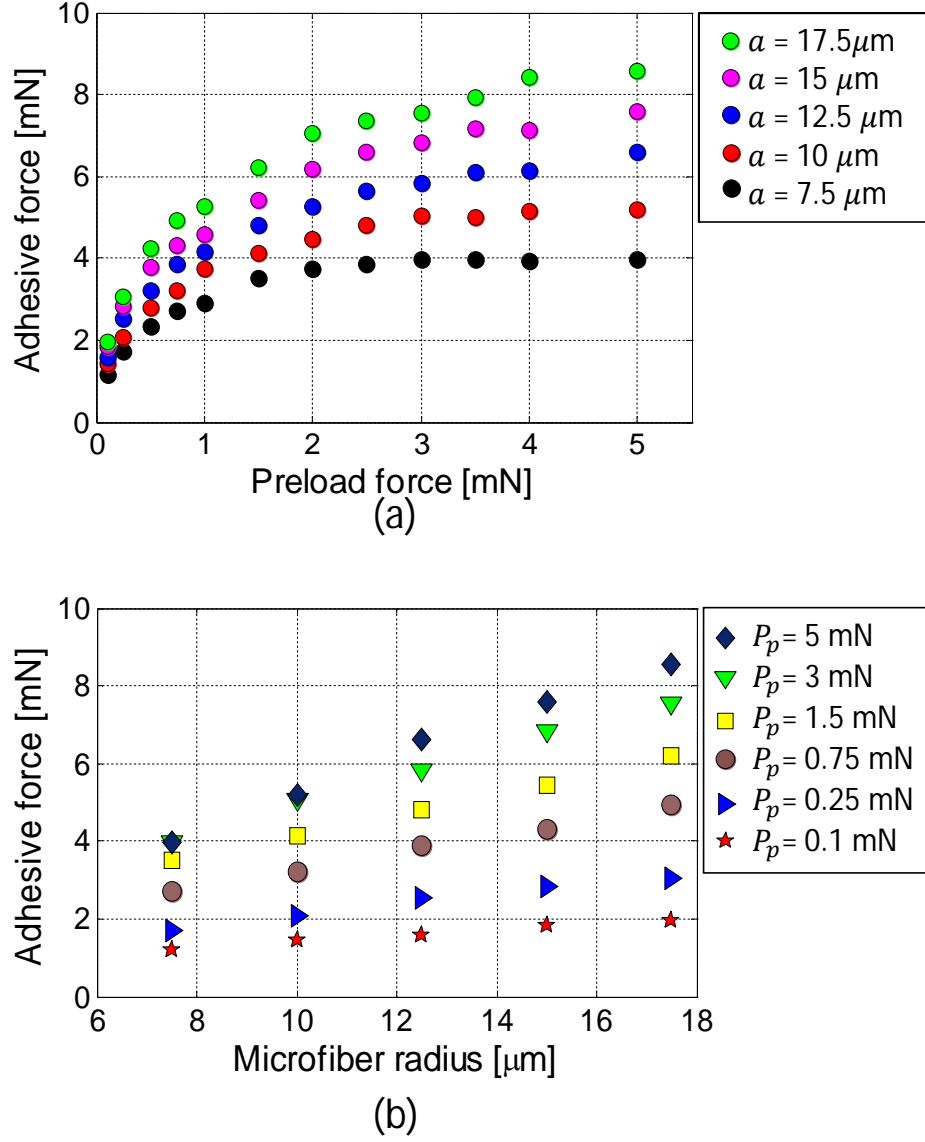


Figure 2.6: Effect of microfiber radius on adhesion with constant center-to-center spacing. Simulation results for a microfiber array of  $L = 100 \mu\text{m}$ ;  $d = 40 \mu\text{m}$ ;  $E_f = 2.9 \text{ MPa}$ ;  $\nu_f = 0.49$ ; and  $w = 96 \text{ mJ/m}^2$ , indented by a sphere of  $R = 2 \text{ mm}$ ;  $E_s = 73 \text{ GPa}$ ; and  $\nu_s = 0.17$ . **(a)** Graph of  $P_c$  plotted against  $P_p$  for various values of  $a$ . **(b)** Graph of  $P_c$  plotted against  $a$  for various values of  $P_p$ . The graphs show an increase in adhesive force as the microfiber radius is increased. The dependence of adhesion on preload force increases as the microfiber radius is increased.

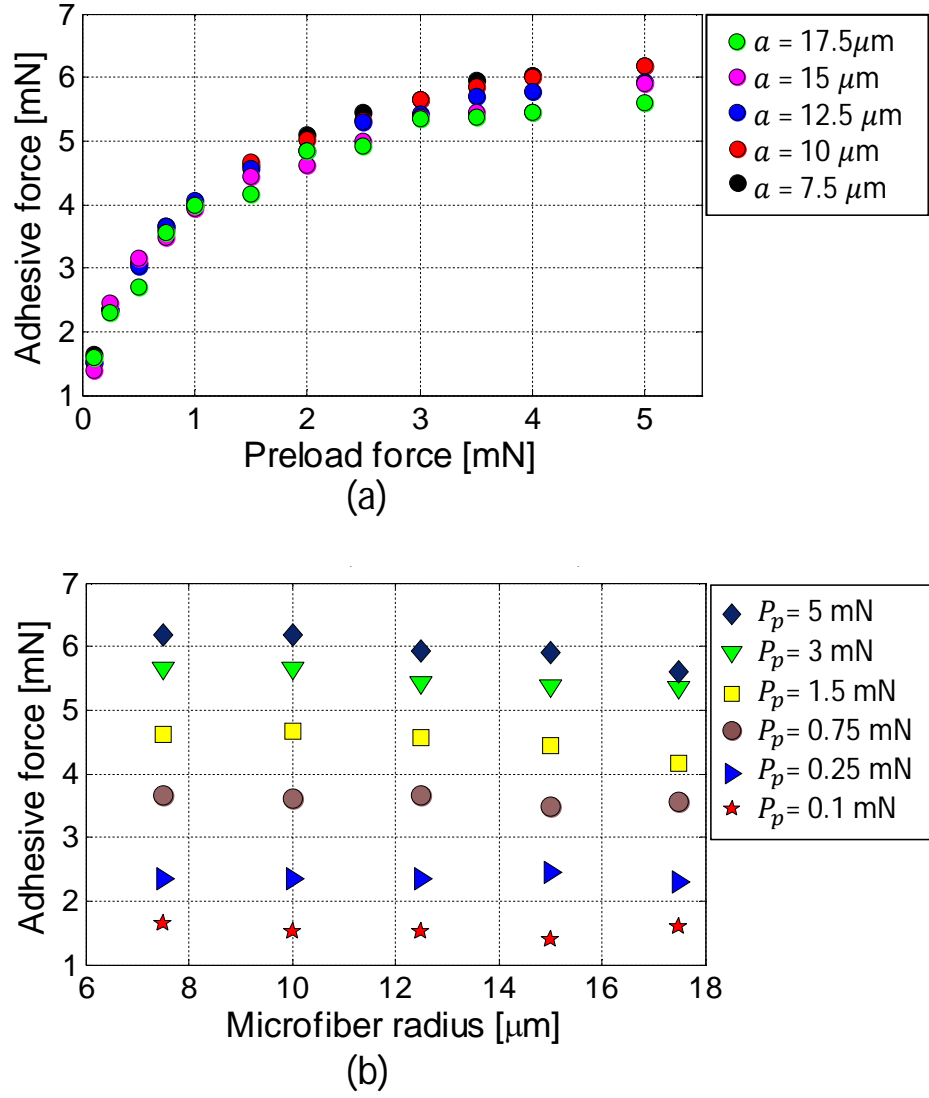


Figure 2.7: Effect of microfiber radius on adhesion with constant edge-to-edge spacing. Simulation results for a microfiber array of  $L = 100 \mu\text{m}$ ;  $d = 40 \mu\text{m}$ ;  $E_f = 2.9 \text{ MPa}$ ;  $\nu_f = 0.49$ ; and  $w = 96 \text{ mJ/m}^2$ , indented by a sphere of  $R = 2 \text{ mm}$ ;  $E_s = 73 \text{ GPa}$ ; and  $\nu_s = 0.17$ . **(a)** Graph of  $P_c$  plotted against  $P_p$  for various values of  $a$ . **(b)** Graph of  $P_c$  plotted against  $a$  for various values of  $P_p$ . The graphs show a decrease in adhesive force as the microfiber radius is increased, for large preload forces.

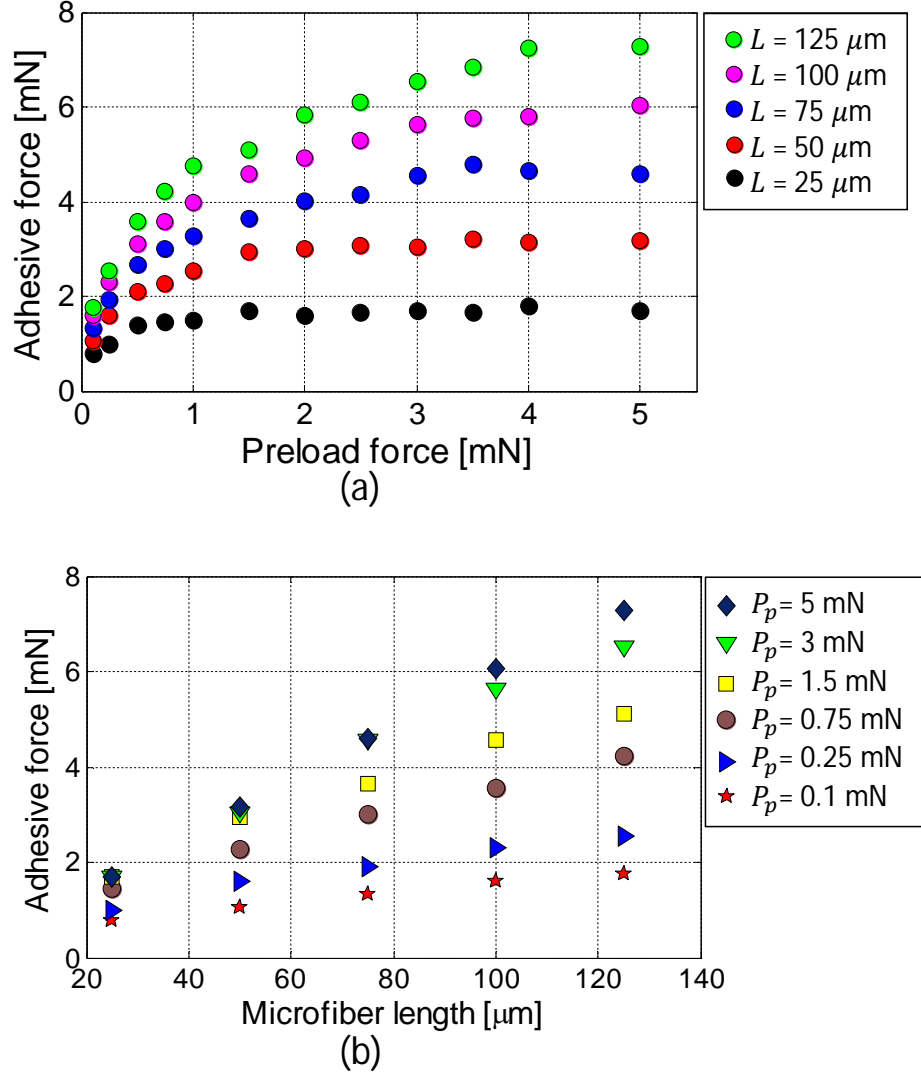


Figure 2.8: Effect of microfiber length on adhesion. Simulation results for a microfiber array of  $a = 12.5 \mu\text{m}$ ;  $S = 15 \mu\text{m}$ ;  $E_f = 2.9 \text{ MPa}$ ;  $\nu_f = 0.49$ ; and  $w = 96 \text{ mJ/m}^2$ , indented by a sphere of  $R = 2 \text{ mm}$ ;  $E_s = 73 \text{ GPa}$ ; and  $\nu_s = 0.17$ . **(a)** Graph of  $P_c$  plotted against  $P_p$  for various values of  $L$ . **(b)** Graph of  $P_c$  plotted against  $L$  for various values of  $P_p$ . The graphs show a direct proportionality between the adhesive force and microfiber length.

## Effect of Young's Modulus

To observe the effect of changes in Young's modulus of the microfiber array, we varied the value of  $E_f$  from 3 MPa to 0.5 GPa. Increasing the Young's modulus of the microfibers will result in an increased value of  $K$ . This increase is relative to the elastic modulus of the indenter, which in this case is significantly greater ( $E_s = 77 \text{ GPa} \gg E_f = 3 \text{ MPa}$ ). Subsequently, increasing  $K$  will lead to an increase in  $F_c$  according to Equation 2.1. On the other hand, an increase in  $E_f$  will increase the stiffness of the array, thereby reducing the number of microfibers in contact with the substrate at a given preload. Increasing  $E_f$  increases  $K$  and reduces  $N$ , so that the net effect on the adhesive force is not intuitively obvious.

Results of the simulations are shown in Fig. 2.9. Figure 2.9a is a graph of  $P_c$  plotted against  $P_p$  for various values of  $E_f$ , and Fig. 2.9b is a graph of  $P_c$  plotted against  $E_f$  for various values of  $P_p$ . Trends from both graphs suggest an increase in the adhesive force for very large increases of the microfiber Young's modulus.

## Effect of Microfiber Spacing

By varying the values of the edge-to-edge spacing  $S$  from  $3 \mu\text{m}$  to  $35 \mu\text{m}$ , we studied the effect of microfiber spacing on adhesion. Based on intuition, one would expect a decrease in the number of microfibers in contact with the substrate, as well as an increase in the compliance of the microfiber array for an increase in  $S$ . Overall, increasing  $S$  is not desirable for a fibrillar interface, except to solve the problem of *lateral collapse*. The results of the simulated variations in  $S$  are shown in Fig. 2.10. Figure 2.10a is a graph of  $P_c$  plotted against  $P_p$  for various values of  $S$ , and Fig. 2.10b is a graph of  $P_c$  plotted against  $S$  for various values of  $P_p$ . As expected, the adhesive force decreases significantly, with a 50% decrease for large preload values.

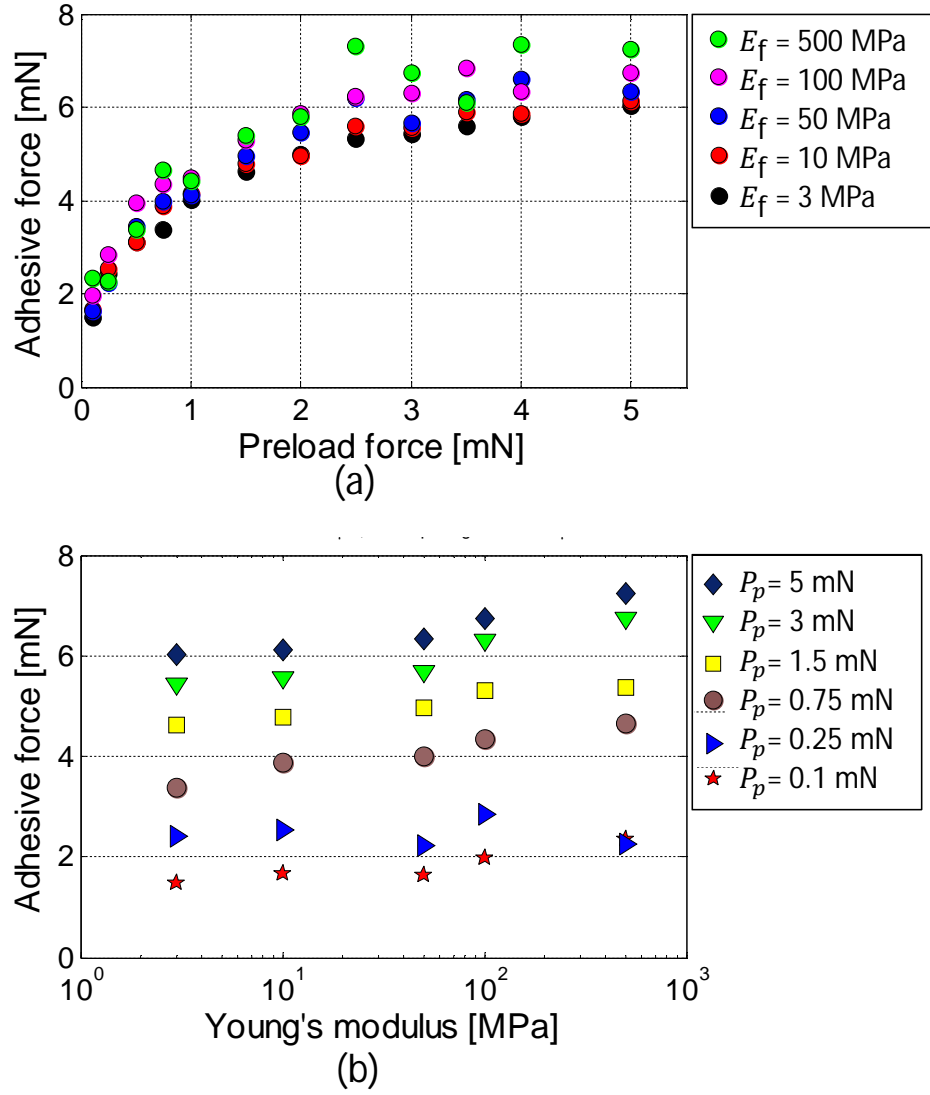


Figure 2.9: Effect of microfiber Young's modulus on adhesion. Simulation results for a microfiber array of  $a = 12.5 \mu\text{m}$ ;  $L = 100 \mu\text{m}$ ;  $S = 15 \mu\text{m}$ ;  $\nu_f = 0.49$ ; and  $w = 96 \text{ mJ/m}^2$ , indented by a sphere of  $R = 2 \text{ mm}$ ;  $E_s = 73 \text{ GPa}$ ; and  $\nu_s = 0.17$ . **(a)** Graph of  $P_c$  plotted against  $P_p$  for various values of  $E_f$ . **(b)** Graph of  $P_c$  plotted against  $E_f$  for various values of  $P_p$ . The graphs show an increase in  $P_c$  as  $E_f$  is increased.

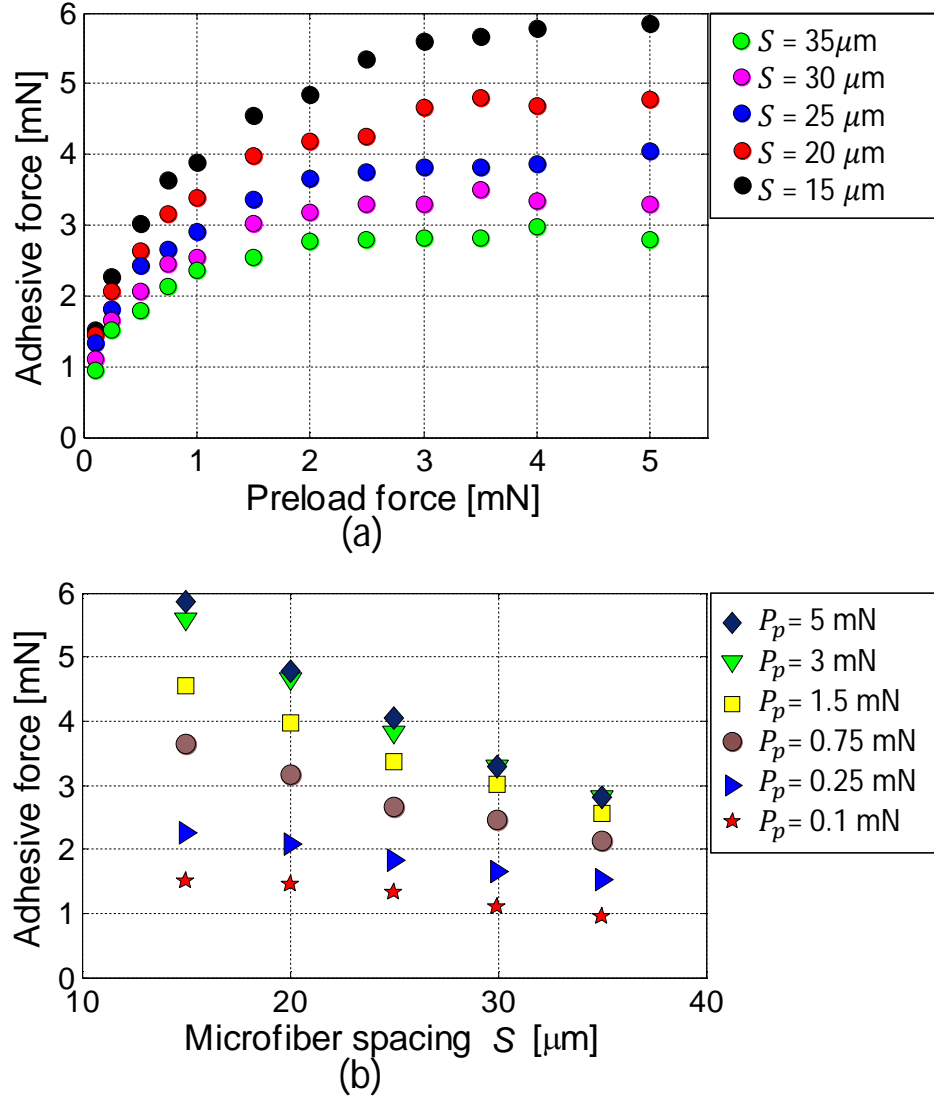


Figure 2.10: Effect of microfiber spacing on adhesion. Simulation results for a microfiber array of  $a = 12.5 \mu\text{m}$ ;  $L = 100 \mu\text{m}$ ;  $E_f = 2.9 \text{ MPa}$ ;  $\nu_f = 0.49$ ; and  $w = 96 \text{ mJ/m}^2$ , indented by a sphere of  $R = 2 \text{ mm}$ ;  $E_s = 73 \text{ GPa}$ ; and  $\nu_s = 0.17$ . **(a)** A graph of  $P_c$  plotted against  $P_p$  for various values of  $S$ . **(b)** A graph of  $P_c$  plotted against  $S$  for various values of  $P_p$ . The results from the graphs show an inverse proportionality between  $P_c$  and  $S$ .



## Effect of Sphere Radius

Apart from studying the effect of variation in microfiber properties, it is also important to know the effect of the size of the spherical indenter. In addition to the advantage of developing an adhesion model for the microfiber-sphere interface, knowledge of the effect of sphere radius will throw light on the performance of fibrillar adhesives in contact with rough surfaces. In this regard, a small spherical indenter is analogous to very rough surfaces while a large indenter is analogous to smooth surfaces ( $R \rightarrow \infty \implies$  smooth flat surface). Simulations were carried out for  $R$  values of 0.5 mm to 2.5 mm. For each value of  $R$ , the preload force was varied from 0.1 mN to 5mN while other parameters were kept constant. Results of the simulations are shown in Fig. 2.11. Figure 2.11a is a graph of  $P_c$  plotted against  $P_p$  for various values of  $R$ , and Fig. 2.11b is a graph of  $P_c$  plotted against  $R$  for various values of  $P_p$ . The results show an increase in adhesive force for higher indenter sizes as anticipated. Dependence of  $P_c$  on preload force is highly pronounced for large  $R$  values with approximately 4 orders of magnitude increase in adhesive force as  $P_p$  is increased from 0.1 mN to 5 mN.

## Effect of Work of Adhesion

The work of adhesion of the interface is dependent on the surface energy of the contacting materials in the form  $w = \gamma_1 + \gamma_2 - \gamma_{12}$ . Where  $\gamma_1$  and  $\gamma_2$  are the adhesive energy of the two surfaces, and  $\gamma_{12}$  is the interfacial energy ( $\gamma_{12} = 0$  for similar surfaces). Here, we study the effect of  $w$  on adhesion of fibrillar adhesives. As shown in Equation 2.1, the adhesive force of each microfiber is directly proportional to the square root of  $w$ , so that increasing  $w$  leads to an increase in  $F_c$ . A similar effect is expected for the microfiber array. Simulations were carried out for  $w$  values of 40 mJ/m<sup>2</sup> to 110 mJ/m<sup>2</sup>, while other properties were kept constant. Similar to previous studies, the preload force was varied from 0.1 mN to 5mN for each value of  $w$ . Results of the simulations are shown in Fig. 2.12. Figure 2.12a is a graph of  $P_c$  plotted against  $P_p$  for various values of  $w$ , and Fig. 2.12b is a graph of  $P_c$  plotted against  $w$  for various values

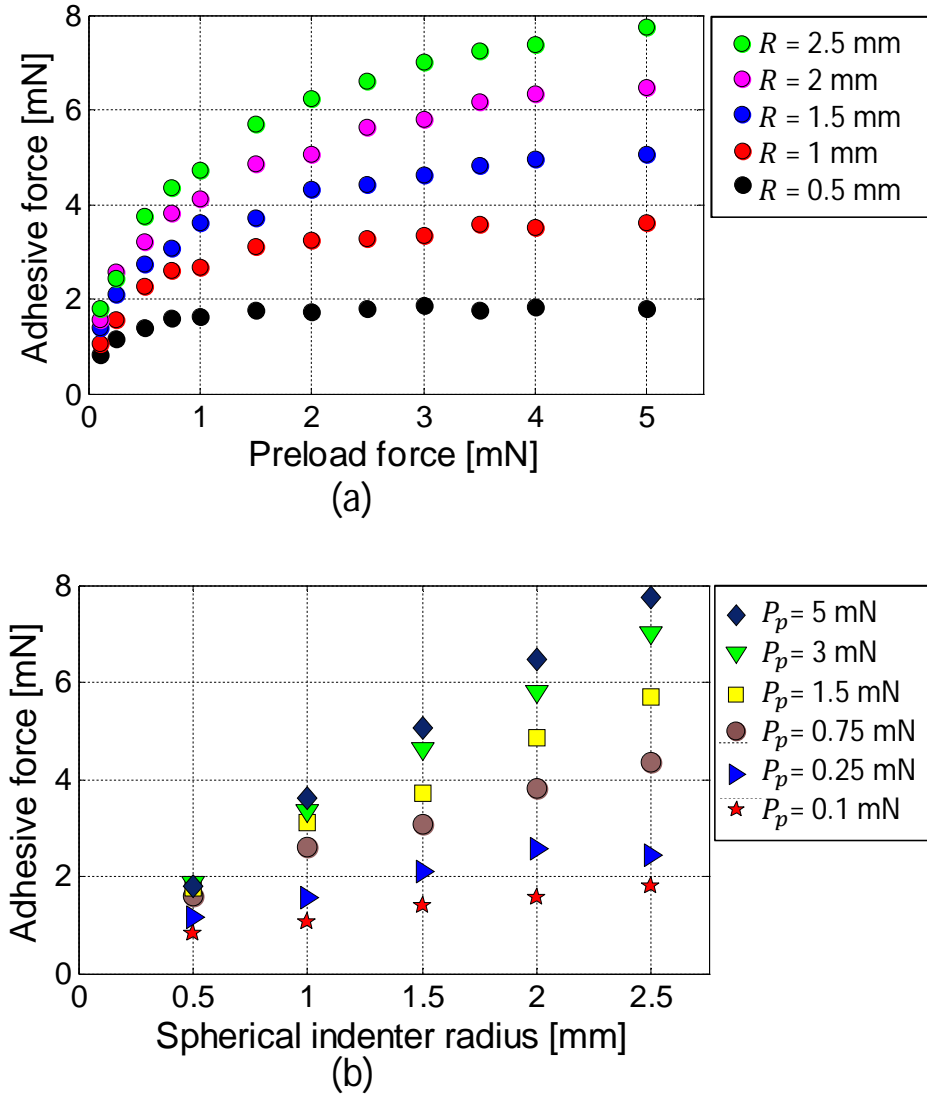


Figure 2.11: Effect of indenter radius on adhesion. Simulation results for a microfiber array of  $a = 12.5 \mu\text{m}$ ;  $L = 100 \mu\text{m}$ ;  $S = 15 \mu\text{m}$ ;  $E_f = 2.9 \text{ MPa}$ ;  $\nu_f = 0.49$ ; and  $w = 96 \text{ mJ/m}^2$ , indented by a various size spheres with  $E_s = 73 \text{ GPa}$ ; and  $\nu_s = 0.17$ . **(a)** A graph of  $P_c$  plotted against  $P_p$  for various values of  $R$ . **(b)** A graph of  $P_c$  plotted against  $R$  for various values of  $P_p$ . The results from the graphs show an increase in adhesive force as the sphere radius is increased. The magnitude of change in adhesion for larger spheres increases as the preload force is increased.

Parameter	Adhesive force
$\uparrow$ Fiber radius, $a$ [ $S = \text{Const.}$ ]	$\downarrow$
$\uparrow$ Fiber radius, $a$ [ $d = \text{Const.}$ ]	$\uparrow$
$\uparrow$ Length, $L$	$\uparrow$
$\uparrow$ Young's modulus, $E_t$	$\uparrow$
$\uparrow$ Spacing, $S$	$\downarrow$
$\uparrow$ Sphere radius, $R$	$\uparrow$
$\uparrow$ Work of adhesion, $w$	$\uparrow$

Table 2.2: Effect of various microfiber parameters on adhesion. Arrow indicates increasing ( $\uparrow$ ) or decreasing ( $\downarrow$ ) values.

of  $P_p$ . The results show an increase in adhesive force as the work of adhesion is increased. Dependence of  $P_c$  on preload force is also pronounced for large  $w$  values as  $P_p$  is increased from 0.1 mN to 5 mN.

Table 2.2 shows a list summarizing the effect of increasing the geometric and material properties on the adhesive force of a microfiber array.

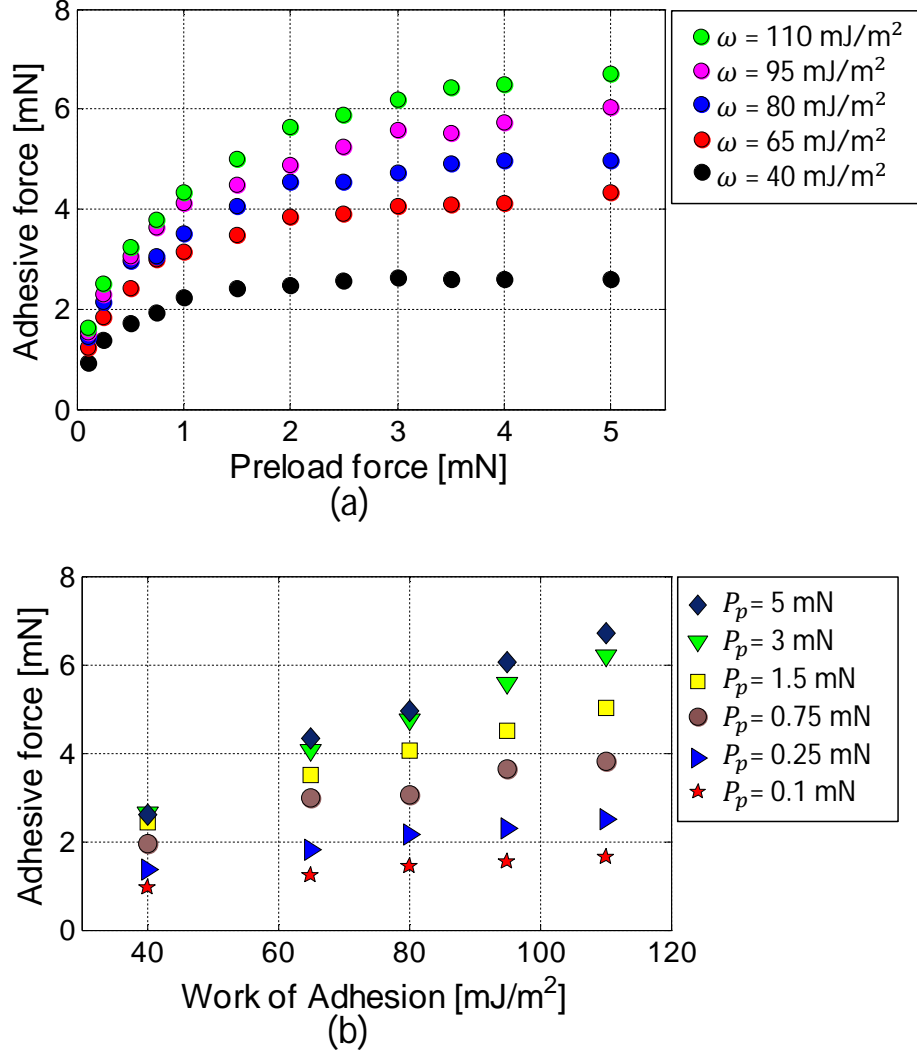


Figure 2.12: Effect of  $w$  on adhesion. Simulation results for a microfiber array of  $a = 12.5 \mu\text{m}$ ;  $L = 100 \mu\text{m}$ ;  $d = 40 \mu\text{m}$ ;  $E_f = 2.9 \text{ MPa}$ ; and  $\nu_f = 0.49$ , indented by a sphere of  $R = 2 \text{ mm}$ ;  $E_s = 73 \text{ GPa}$ ; and  $\nu_s = 0.17$ , for various values of  $w$ . **(a)** Graph of  $P_c$  plotted against  $P_p$  for various values of  $w$ . **(b)** Graph of  $P_c$  plotted against  $w$  for various values of  $P_p$ . Results show an increase in adhesive force as the work of adhesion is increased

### 2.3.4 Conclusion

Using the flat punch theory along with elastic theories, we developed a new model of adhesion for fibrillar adhesives that takes several factors that influence microfiber adhesion into account. A simulation procedure was also developed for obtaining the adhesive force of a microfiber array in contact with a spherical surface. From the model and simulation, the effects of microfiber's material and geometric properties as well as the indenter size were studied, giving insights into the design of microfiber adhesives with controllable adhesive strength.

## 2.4 Rate-dependent Adhesion of Microfiber Adhesives

### 2.4.1 Introduction

Recent studies have shown a strong rate-dependence of adhesion for synthetic microfiber adhesives. The use of high retraction speed to enhance the adhesive strength of fibrillar adhesives for transfer printing applications has also been demonstrated [24, 38, 78], and a pick-to-release force ratio of up to 1000:1 has been reported when combined with optimized geometric features [78]. Previous work studying rate-dependent adhesion focused on the contribution of material properties [24], and experiments were conducted only for fibrillar structures with a thin film covering [137]. By varying the bulk viscoelastic material properties of their fibril samples, Castellanos et al. [24] showed that the rate dependence of adhesion in fibrillar adhesives is a function of the viscoelastic material properties. Feng et al. [38] showed the dependence of peeling velocity on the critical energy release rate of their elastomer stamps, and applied this feature in controlled transfer printing. They suggested that rate-dependent adhesion was due to the *mechanical behavior* at the interface only and that bulk material properties had negligible influence. The adhesion of gecko and gecko-inspired adhesion has also been shown and modeled to be dependent on sliding friction and a result of nano-scale stick-slip mechanics of fibrillar adhesive [50, 111]

So far, no detailed work has been reported on the underlying mechanism for rate induced change in adhesive strength of elastomer fibrillar structures (by using tensile loading rate or strain rate). In this work, we verified that the retraction speed effect is due to mechanics at the contact interface. We studied the effect of retraction speed on the real contact area  $A_{\text{real}}$ , the rate of change in contact area  $dA_{\text{real}}/dt$ , and the crack propagation speed  $v$  at the interface between a single, high-aspect-ratio elastomer post and a rigid, smooth and flat substrate. Large structures (up to 5 times larger than that present in fibrillar adhesives) were used in our experiments to allow for a better view of the contact interface and to monitor crack propagation. By using high aspect ratio structures, we expect the behavior of our post to be similar to that of smaller microfiber structures present in fibrillar adhesives. This correlation has been shown by previous investigators [3, 132].

## 2.4.2 Experiments

### Sample Fabrication

Large cylindrical posts made from polyurethane elastomer (BJB Enterprises; ST 1087) with a radius of 0.7 mm and a length of 7 mm, were fabricated by molding [3]. Figure 2.13 shows the fabrication steps. A smooth steel rod is press-fitted vertically into an acrylic dish, and liquid silicone rubber is poured into the dish until it is filled. A flat acrylic cover with a through-hole is fitted through the top of the rod and pressed onto the dish (Fig. 2.13a). After curing for 24 hrs, the silicon rubber mold is removed and placed on a flat substrate. Liquid polyurethane is then poured into the mold, and acrylic glass is placed on it for backing support (Fig. 2.13b). After 24 hrs, the polyurethane is peeled off from the mold to obtain soft cylindrical posts with an aspect ratio (length/radius) of 10, and with a backing layer thickness of  $400\ \mu\text{m}$  (Fig. 2.13c). The sample was glued to a glass slide before mounting to the adhesion measurement setup. A separate glass slide (Microscope Slides; Fisher Scientific), cleaned with ethyl alcohol and deionized water and dried using compressed air, was used as the contacting surface.

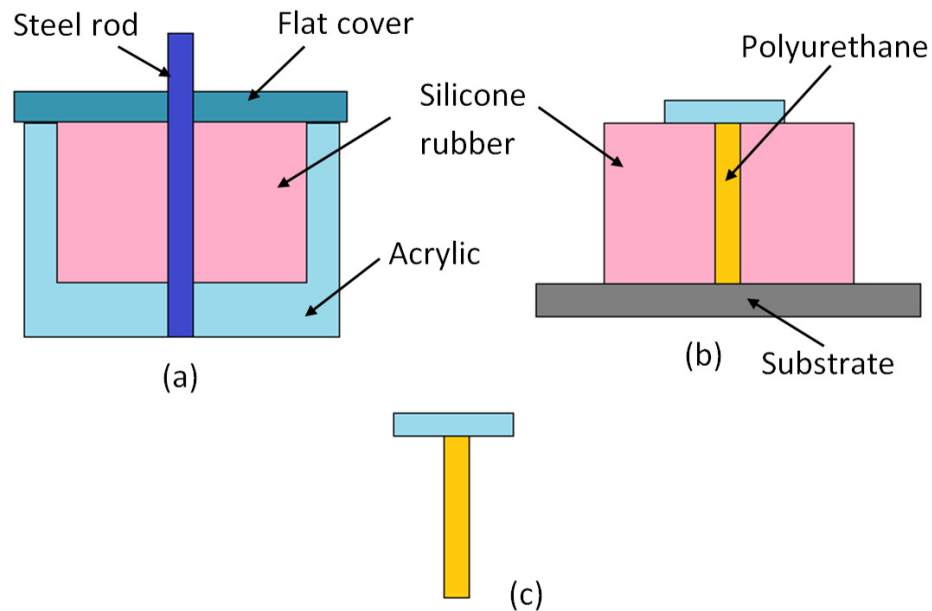


Figure 2.13: Procedures for fabricating a single cylindrical microfiber post with flat tip. **(a)** A smooth steel rod is press fitted vertically into an acrylic dish, and liquid silicone rubber is poured into the dish until it is filled. Flat acrylic cover with a through-hole is fitted through the top of the rod, and pressed onto the dish. **(b)** After curing for 24 hrs, the silicon rubber mold is removed and placed on a flat substrate. Liquid polyurethane is then poured into the mold, and an acrylic glass is placed on it for backing support. **(c)** After 24 hrs, the polyurethane is peeled off from the mold.

## Experimental Procedure

A custom adhesion measurement system consisting of automated high precision stages (MFA-CC; Newport), an inverted microscope (Nikon Eclipse TE200), a high-resolution load cell (GSO-25; Transducer Techniques Inc), and a controller was used in the experiment (Fig. 2.14). Details of the adhesion measurement setup have been previously reported [2]. The microfiber sample is mounted on the loadcell, and a glass slide is mounted onto the microscope stage. The automated stage is controlled using custom adhesion software. A high speed camera (pco.dimax) was used to record images of the contact area through the inverted microscope at a frame rate of 100 frames per second. A monochromatic 546 nm light source was channeled through the inverted microscope onto the contact interface to observe the real contact area [63].

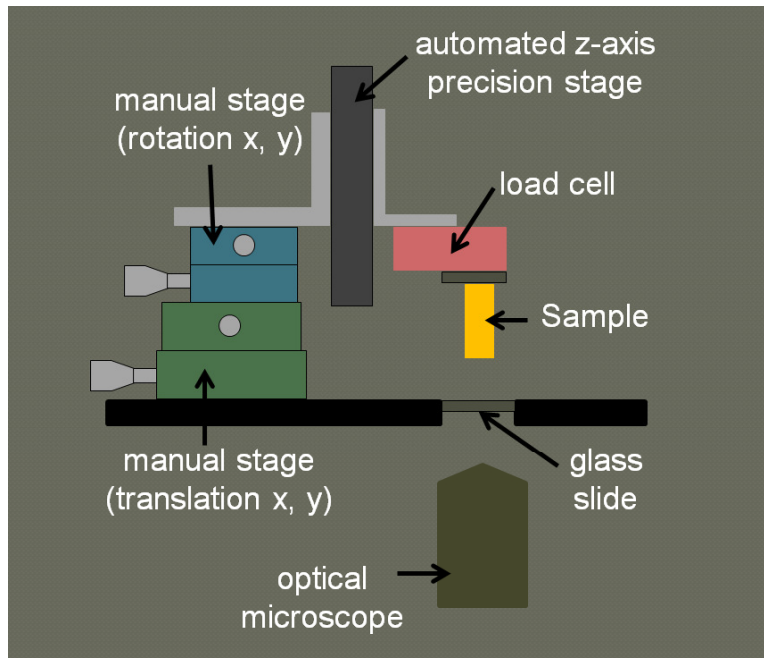


Figure 2.14: Schematic drawing of a custom built experimental setup for studying the effect of retraction speed on adhesion.

During the experiments, the sample was lowered at a constant velocity of  $10 \mu\text{m/s}$  until it made full contact with the glass slide. Due to the flatness of the microfiber and the fine alignment of the adhesion measurement system, full contact was achieved at a significantly low



preload force of 2 mN. A wait time of 10 s was observed before the sample was pulled vertically away from the substrate at retraction speeds ranging from 5 to 450  $\mu\text{m/s}$ . Three experiments were conducted at each of the nine retraction speeds studied.

A graph of the force data plotted against time is shown in Fig. 2.15. From the graph, the preload force - labeled A, is the maximum compressive load before retraction is initiated; the adhesive force - labeled E, is the maximum tensile force during retraction. We denote the time when the adhesive force is reached as  $t_c$ . Fig. 2.15 also includes real-time images of the contact interface at various times during a single experiment cycle.

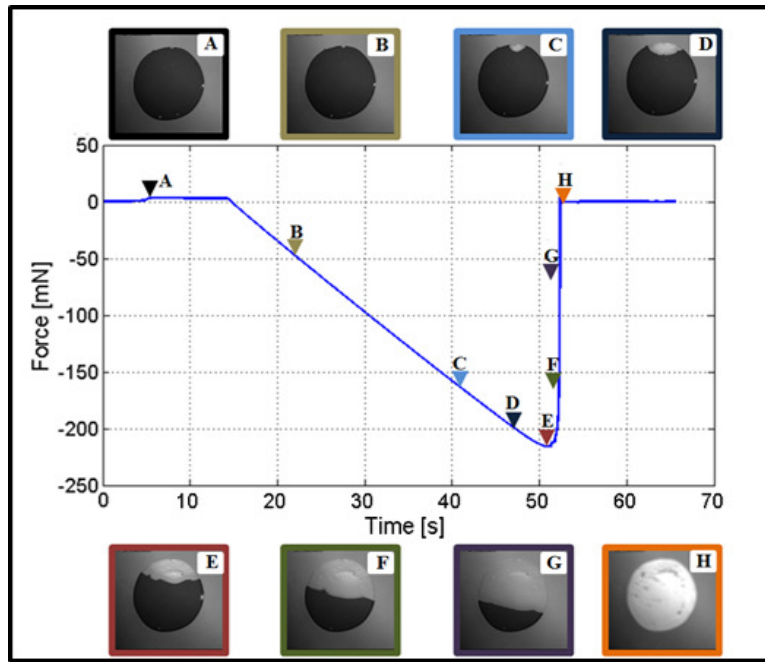


Figure 2.15: A graph of measured force in real time with corresponding images, for a retraction speed of 10  $\mu\text{m/s}$ . **A** is the contact image when the preload force is reached; **E** is the contact image at the time the adhesive force is recorded; **H** is the contact image after detachment.

### 2.4.3 Theoretical Model

Using basic models of adhesion and a power law relationship for the dependence of surface energy on crack propagation speed, we present a simple model for the adhesion dependence on crack propagation speed for a single cylindrical adhesive structure. Maugis [94] showed that

the critical energy release rate  $G$  for a circular flat punch is related to the pull-off force  $F_c$  given by

$$G = \frac{F_c^2}{6\pi a^3 K} \quad (2.22)$$

where  $a$  is the punch radius and  $K$  is the reduced elastic modulus earlier defined by Equation 2.2. Also, the dependence of  $G$  on crack propagation speed  $v$  can be represented by

$$G(v) = G_0 \left[ 1 + \left( \frac{v}{v_0} \right)^n \right], \quad (2.23)$$

where  $G_0$  is the critical energy release rate as  $v \rightarrow 0$ ,  $n$  is a scaling parameter that is empirically fitted to the experimental data,  $v_0$  is the crack propagation speed at which  $G$  doubles to  $G_0$ . Such a power law has been shown to hold for polymer materials at low crack propagation speeds [16, 38, 42].

Combining Equations 2.22 and 2.23, we obtain an equation that relates the pull-off force to the crack propagation speed as

$$P = \sqrt{6\pi a^3 K G_0 \left[ 1 + \left( \frac{v}{v_0} \right)^n \right]}, \quad (2.24)$$

which can be represented as

$$F_c = \chi \sqrt{\left[ 1 + \left( \frac{v}{v_0} \right)^n \right]} \quad (2.25)$$

where  $\chi = \sqrt{6\pi a^3 K G_0}$  is a constant and a function of the post geometry and material properties.

#### 2.4.4 Results and Discussions

A graph of adhesive force measured at various retraction speeds is shown in Fig. 2.16a. The graph shows an increase in adhesive force as we increased the retraction speed from 5  $\mu\text{m/s}$  to 450  $\mu\text{m/s}$ , similar to a previously reported trend [24]. The real contact area of the interface

was extracted from the recorded high speed video. The progression of  $A_{\text{real}}$  until detachment is shown for each retraction speed in Fig. 2.16b. We observe that detachment occurs faster for increasing retraction speed, with  $dA_{\text{real}}/dt$  approaching infinity at detachment.

We also obtain the critical contact area  $A_{\text{real}}^c$  at the time the pull-off force is recorded, i.e. at  $t_c$  from the recorded video. Fig. 2.16c shows a plot of  $A_{\text{real}}^c$  normalized by the cross sectional area of the sample, for various retraction speeds. The plot shows that the real contact area at  $t_c$  remains approximately constant as the retraction speed is increased. The result suggests that there is a critical contact area at which the maximum adhesive force is recorded for a given geometry and material property. The result also indicates that the contact area at  $t_c$  has negligible contribution to rate dependence of adhesion. The crack propagation speed was also extracted from high speed video. A plot of the critical crack propagation speed  $v_c$  at time  $t_c$  is plotted against retraction speed in Fig. 2.16d. From the plot, we see a dependence of  $v_c$  on the retraction speed. This observation shows that for cylindrical flat punch, similar to the peeling of a thin film, the crack propagation speed at the contact interface contributes to rate-dependence of adhesion.

We compared the theoretical model to our experiment for validation. Using Equation 2.22 for a post radius of 0.7 mm, we obtained the energy release rate of our experiments for each retraction speed, and by plotting against the crack propagation speed, we found the value of  $G$  at  $v = 0$  to be  $G_0 = 1.335 \text{ J/m}^2$ . The speed at which  $G_0$  doubles was also found to be  $v_0 = 3.37 \times 10^{-3} \mu\text{m/s}$ , when  $n = 0.69$ . Figure 2.17a shows a plot of the critical energy release rate against crack propagation speed for experimental data and the theoretical model from Equation 2.23. The plot shows high correlation between the experimental data and the power law for crack propagation speeds up to  $0.1 \mu\text{m/s}$ . Figure 2.17b shows that the predicted adhesive force from Equation 2.25 matches closely with our experimental results.

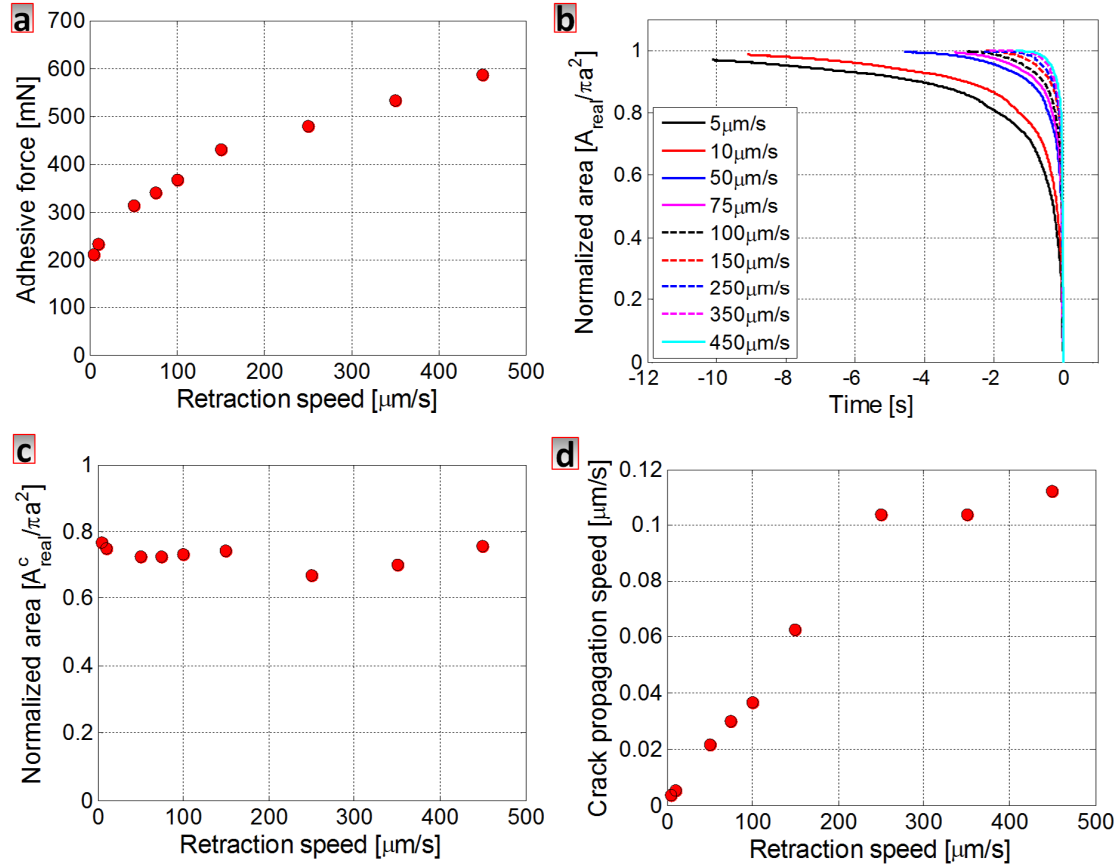
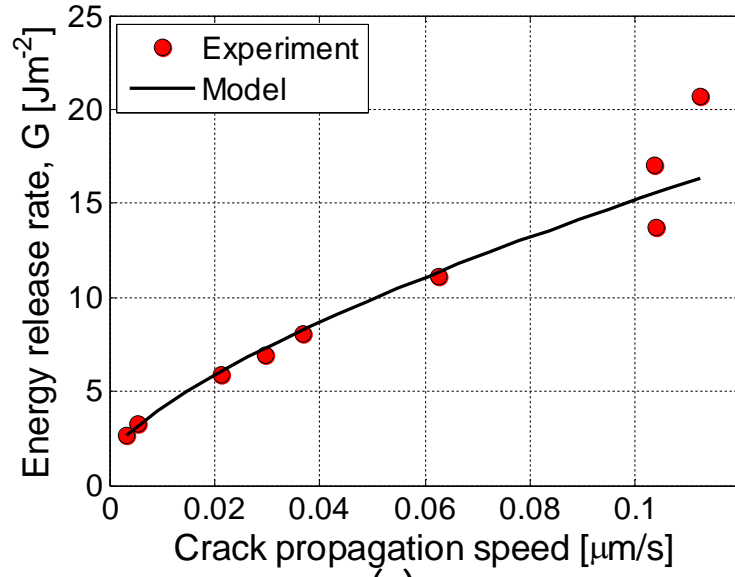
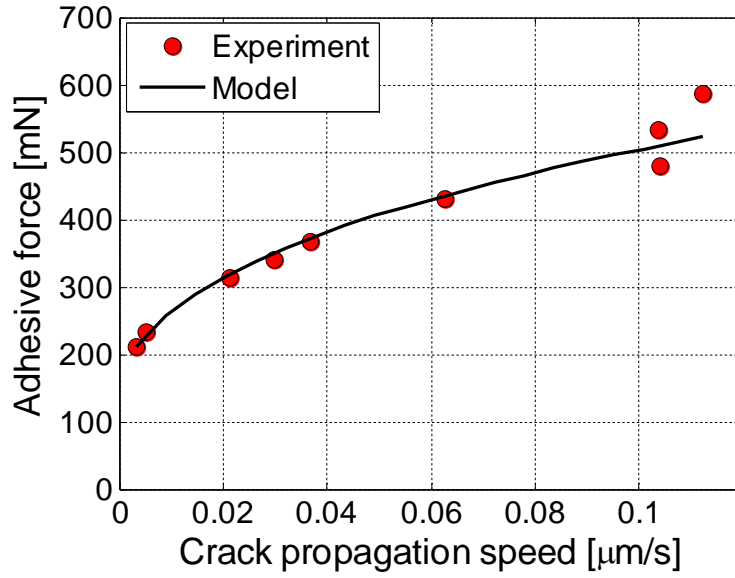


Figure 2.16: Graph showing the effect of retraction speed on adhesive force. Each point represents the mean of adhesive forces measured from 3 experimental cycles at the same retraction speed and on the same location. **(a)** Graph of adhesive force at various retraction speeds show an increase in adhesive force as the retraction speed is increased. **(b)** Graph of normalized contact area for various retraction speeds indicates longer detachment times for slower retraction speeds and vice versa. The graph also shows that  $dA_{\text{real}}/dt$  approaches infinity at detachment, for all retraction speeds. **(c)** Graph of normalized contact area measured at  $t_c$  for various retraction speeds shows no significant change in contact area at various retraction speeds. **(d)** Graph of crack propagation speed at  $t_c$  for various retraction speeds shows an increase in the crack propagation speed as the retraction speed is increased. This result indicates a significant dependence of the crack propagation speed on retraction speed.



(a)



(b)

Figure 2.17: Graph showing the effect of crack propagation speed on energy release rate. **(a)** Graph of experimental energy release rate and theoretical power-law fit for  $n = 0.69$ ,  $G_0 = 1.335 \text{ J/m}^2$ , and  $v_0 = 3.37 \times 10^{-3} \mu\text{m/s}$ . The graph shows a power law relation as Equation 2.23 for the energy release rate as a function of crack propagation speed. **(b)** Graph of adhesive force as a function of crack propagation speed for our experimental cylindrical fibril matches closely with our theoretical model in Equation 2.25, for  $\chi = 0.149 \text{ N}$ .

## **2.4.5 Conclusion**

In conclusion, we have shown using a single cylindrical elastomer adhesive flat punch structure that the rate-dependence of adhesion of elastomer fibrillar structures is a function of the crack propagation speed at the interface. By using high aspect ratio structures, we expect the behavior of our post to be similar to that of smaller microfiber structures present in fibrillar adhesives. A model of the dependence of adhesive force on crack propagation speed for a cylindrical fibril was developed, which matched well to experiments. Our result verifies that the mechanism of the retraction speed effect is due to mechanical interactions at the interface and that the influence of the bulk material properties is negligible.

## 2.5 Summary

We have developed a new model of adhesion for microfiber adhesives that serves as an improvement to previous models. In our new model, the deformation of the backing layer is non-uniform unlike previous models, and the material properties of the backing layer are taken into consideration. A simulation procedure was also developed for obtaining the adhesive force of a microfiber array in contact with a spherical surface. The model of adhesion will be used in our study in the following chapters to study the mechanics of dry-contact cleaning.

The effect of retraction speed on the adhesive force of microfiber adhesives was also studied. We showed that the rate-dependence of adhesion of elastomer fibrillar structures is a function of the crack propagation speed at the interface. A model of the adhesive force of a microfiber adhesive that incorporates the effect of crack propagation speed has been developed, with results that match well with our experiments.

The models in this section can be extended to microfibers with spherical tips by replacing the equation of the pull-off force for a single flat-tip microfiber (Equation 2.1) with the following equation for spherical contacts [70]:

$$F_c = \frac{3}{2}\pi\rho_a w, \quad (2.26)$$

where  $\rho_a$  is the radius of curvature of the microfiber tip. The model can also be extended to microfibers with mushroom tips. In this case, the pull-off force for a single microfiber is given as [60]

$$F_c = \sigma_0 \pi a_t^2, \quad (2.27)$$

where  $\sigma_0$  is the interfacial strength of a single mushroom tip microfiber.

# Chapter 3

## Mechanisms and Mechanics of Contact

## Self-cleaning in Microfiber Adhesives

### 3.1 Introduction

This chapter presents an in-depth study of self-cleaning of microfiber adhesives. We begin by defining self-cleaning as applied to microfiber adhesives and present an overview of previous studies on the subject. 3.2 presents three major categories of self-cleaning and seven distinct mechanisms under these categories. In Section 3.3, we will develop models of contact self-cleaning of fibrillar adhesives for various scenarios based on the contaminant to microfiber size ratio. A chapter summary is presented in Section 3.4.

#### 3.1.1 What is Self-cleaning?

The word “self-cleaning” has been generally used both in the research community where it is popularly used in connection with the lotus effect (discussed later), and in present-day society where it has gained popularity in connection with the *self-cleaning* cooking oven, and recently with *self-cleaning* windows or paint coatings. However, when referring to self-cleaning, espe-



cially of objects, there is the question of the object's ability to make itself free of dirt in and of itself, in the absence of an external (human or natural) impetus or stimulus. Before defining self-cleaning, it is useful to first define "cleaning" in microfiber adhesives

Regardless of the process or mechanism involved, the goal of cleaning contaminated microfiber adhesives is to recover any adhesion performance that have been lost as a result of contamination. In other words, after cleaning, the contaminants should no longer be detrimental to the performance of the adhesive. For microfiber adhesives, we propose two modes of contaminant displacements, namely (see (Fig 3.5(c))):

- **Deposition:** the complete removal of the dirt particles from microfiber adhesive array, and
- **Embedding:** the dirt particles are removed from the microfiber tips and become lodged between adjacent microfibers or pockets within the array.

So that cleaning in microfiber adhesives is not restricted to the removal of dirt completely from the adhesive array. This understanding expands on previous studies of self-cleaning in microfiber adhesives which until now, considered cleaning only by deposition. Although it has not been regarded as a cleaning measure, embedding of contaminants has been observed in the natural gecko, and we believe that it plays a crucial role in the gecko's self-cleaning characteristics (discussed later). The principal goal of cleaning for the gecko and for synthetic microfiber adhesives is to recover adhesion as quickly as possible, which can be achieved by simply removing contaminants from the tips of the adhesive structures. The short-term destination of contaminants is not critical for the effectiveness of the gecko toe or its synthetic equivalent. However, it is important to note that particle embedding is only a temporary cleaning process, hence the shedding of the gecko toe skin (*molting*) every two months.

Thus, for cleaning to be considered as self-cleaning, it should occur with minimal influence from the user of the adhesive. Taking insight from the lotus leaf, we can limit self-cleaning in microfiber adhesives to when:

- the adhesive gets cleaned while in its natural state, or
- the adhesive gets cleaned in the process of use.

This is similar to a lotus leaf getting cleaned while it is in its natural muddy environment, or while performing its fundamental task of supplying nutrients to the plant through photosynthesis.

Based on this understanding, we will now go on to define self-cleaning in microfiber adhesives as:

*“the removal of contaminants from the tips of microfiber adhesives in the process of use or in their natural state, such that the contaminants are no longer detrimental to the immediate performance of the adhesives.”*

The above definition allows for a broad range of self-cleaning mechanisms, while limiting the cleaning method to application-based procedures only.

### 3.1.2 Self-cleaning in Nature

Considering the large effort and financial cost currently placed on cleaning in today’s society, we can certainly use some insights from natural organisms that possess highly efficient and effective cleaning strategies. Using physical, chemical and geometric characteristics, many plants, birds, large-winged insects and other organisms achieve cleaning effortlessly [17, 25, 130]. Some of nature’s self-cleaning organisms include butterfly wings, fish and shark skins, the lotus leaf and the cicada (Fig. 3.1). These remarkable self-cleaning biological materials have inspired research efforts aimed at developing materials or material coatings that mimic natural cleaning strategies.

#### Self-cleaning of the Lotus Leaves

The lotus plant (*Nelumbo nucifera*) is one of nature’s highly efficient cleaners (Fig. 3.1). Despite growing in muddy environments, it is able to maintain clean leaves and flowers [17]. On

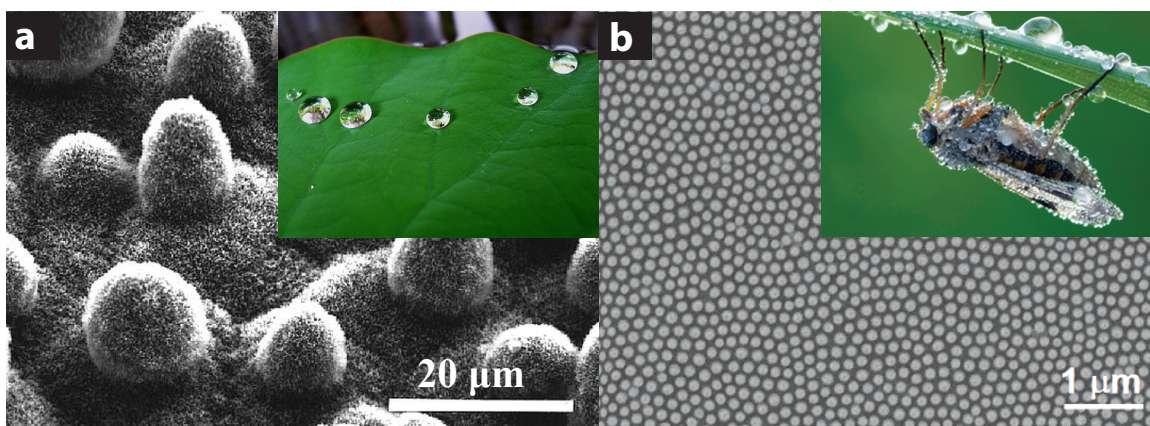


Figure 3.1: SEM images showing the surface topography of natural organisms with self-cleaning characteristics. **(a)** Hierarchical micro- and nanostructures on the lotus leaf (*Nelumbo nucifera*) [17]. (Inset) Water droplets on a lotus leaf (*Nelumbo nucifera*). **(b)** Nanostructure on the superhydrophobic wings of cicada (*Cicada orni*) [17]. (Inset) Water droplets on a cicada (*Cicada orni*). Insets courtesy of tanakawho on Flickr, and blogspot.com.

the surface of a lotus leaf are micro/nano-scale structures (Fig. 3.1a) which, along with a waxy surface chemistry, gives the leaf a superhydrophobic behavior that prevent dirt and water from adhering to the leaf. When rainwater comes in contact with the lotus plant, it balls up into droplets due to the air trapped in the rough surface of the leaf. Dirt particles on the leaf's surface adhere to these water molecules, and any slight tilting of the leaf causes the water to roll off, taking the contaminants along with it. This remarkable process, known as the *lotus effect*, has led to the development of consumer products with the unique qualities of repelling and dislodging stains and dirt [125].

### Self-cleaning in Geckos

Recently, researchers discovered that the gecko feet can remain clean despite its remarkably sticky characteristics. Observation of the gecko feet and its setae over a period of months between molt cycles shows that it stays clean [52]. This novel discovery brought excitement, along with questions to researchers in the microfiber adhesion community. First, the discovery of the unique cleaning feature in the gecko's adhesive pad has significantly broadened the potential

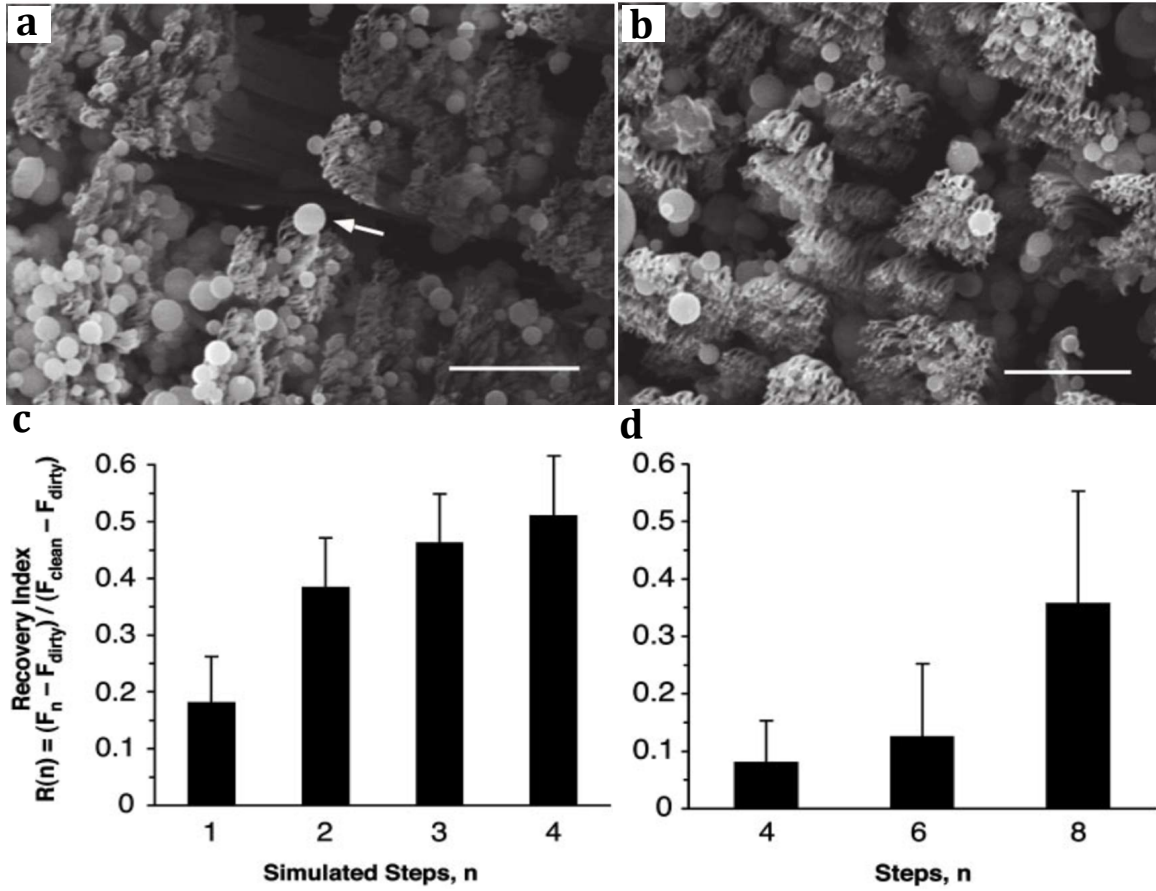


Figure 3.2: Evidence of self-cleaning in gecko setae. Using microspheres as contaminants on a gecko setae array, Hansen and Autumn [52] showed that the gecko setae can recover up to 51% of lost shear force after 4 simulated steps. **(a)** SEM image of a contaminated setae array. Arrow indicates a microsphere adhering to several spatulae. **(b)** SEM image of an array from the same animal in (a) after five cleaning steps showing that spatular surfaces are mostly clean, although microspheres are still present. **(c)** Graph of recovery index as a function of cleaning steps for an isolated setal array. **(d)** Graph of recovery index as a function of simulated steps for digits of live geckos. In this figure,  $R(n)$  is the recovery index,  $F_n$ ,  $F_{dirty}$ , and  $F_{clean}$  are the measured adhesive force after a cleaning step, immediately after contamination, and before contamination, respectively after  $n$  cleaning cycles, Scale bars = 10  $\mu\text{m}$ .

application of microfiber adhesives; adding yet another reason for researchers to invest time and resources in this area of study. On the other hand, the discovery of the gecko's self-cleaning ability has raised several questions such as: (I) how does the gecko setae achieve cleaning? and (II) what properties of the setae are crucial for the gecko's unique cleaning characteristic? The discovery also suggests that synthetic microfiber adhesives with similar cleaning ability can be developed, and has raised the standard for researchers whose goal is the development of synthetic microfiber adhesives with similar (or improved) characteristics compared to that of the natural gecko.

### **3.1.3 Self-cleaning of Synthetic Microfiber Adhesives**

Inspired by the self-cleaning functionality of the gecko setae, several researchers have begun working towards achieving this important characteristic in synthetic microfiber adhesives [44, 59, 76, 88, 89, 95, 121, 134]. Shortly after the unveiling of self-cleaning in geckos, Tsai et al. [134] presented the first investigation of self-cleaning in synthetic microfiber adhesives. Taking inspiration from the lotus plant, their approach involved the design of microfiber adhesives with optimal hydrophobicity in order to facilitate cleaning with the use of water droplets or in the presence of a liquid medium. The work by Tsai et al. was accompanied by several efforts [76, 89, 121] to develop microfiber adhesives with superhydrophobic behavior, with the aim of achieving self-cleaning in liquid environments.

Researchers have also investigated self-cleaning of synthetic adhesives that involves dynamic effects such as sample vibration [121] and digital hyperextension [59] which we discuss later in this Chapter. Another approach taken toward achieving self-cleaning in microfiber adhesives is inspired by the initial work on self-cleaning in geckos [52], and involves the self-cleaning of microfiber adhesives as a result of contact with a clean dry substrate [44, 88, 95].

Anti-fouling (also known as contamination resistance) refers to the ability of the adhesive to maintain some amount of adhesion after contamination. Anti-fouling has also been reported

in synthetic gecko adhesives with mushroom tips [48], with a supporting model by Carbone et al. [22].

## 3.2 Mechanisms of Self-cleaning of Microfiber Adhesives

The mechanisms of self-cleaning of microfiber adhesives can be grouped into three major categories namely; (I) wet self-cleaning, (II) dynamic self-cleaning and (III) contact self-cleaning. Figure 3.3 shows an example cleaning mechanism for each of the categories. The various categories along with their associated self-cleaning mechanisms are discussed below.

### 3.2.1 Mechanisms of Wet Self-cleaning

As the name implies, wet self-cleaning involves the self-cleaning of microfiber adhesives in the presence of a liquid medium. It is the most studied and the most understood self-cleaning process for microfiber adhesives [56, 76, 80, 89, 121, 134]. Wet self-cleaning in microfiber adhesive is attained by optimizing the density of microfibers in the arrays in order to achieve a superhydrophobic behavior [134] or tuning the tip geometry of the microfibers [76]. The superhydrophobicity of the array helps to foster the attachment of dirt particles in the array to water molecules and the removal of water molecule along with the contaminants from the microfiber array. The associated mechanisms of wet self-cleaning include:

**(I) Rolling of Water Droplets:** Similar to the lotus effect, it involves the rolling of water droplet(s) across the tip of a contaminated microfiber adhesive, effectively removing the contaminants in its path (Fig. 3.3(a)). This mechanism has been studied for microfiber adhesives made from synthesized e-beam photoresist and high aspect ratio carbon nanotubes [133], high aspect ratio microfibers made from high density polyethylene [89], and mushroom tipped microfibers made from polyurethane elastomer [76]. In these cases, adhesion recovery ranging from 98 – 100% were reported.

**(II) Capillary Adhesion:** Unlike the lotus effect which involves water molecules, capillary adhesion requires partial or full immersion of the adhesive in a liquid medium. Self-cleaning through the process of capillary adhesion has been reported for microfiber adhesives made from vertically aligned carbon nanotubes [121]. Sethi et al. [121] demonstrated adhesion recovery of their microfiber adhesives by rinsing the contaminated adhesive with water and reported a 60% adhesion recovery.

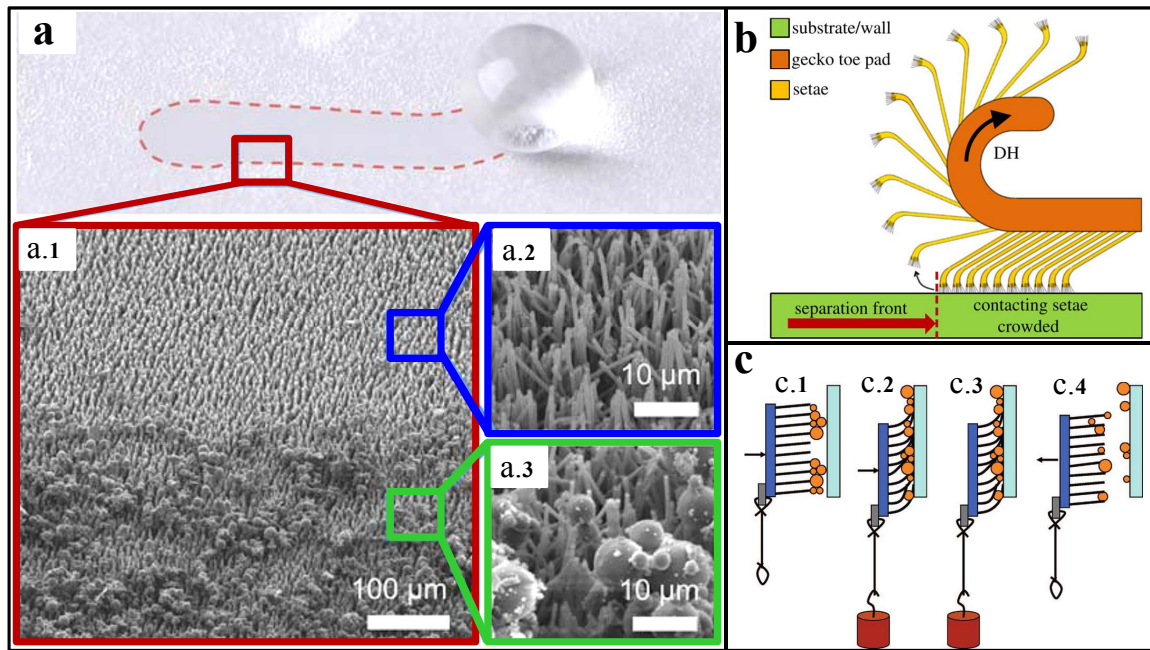


Figure 3.3: Mechanisms of self-cleaning of microfiber adhesives. **(a)** Wet self-cleaning of high aspect ratio microfiber adhesives made from high density polyethylene by rolling of water molecules [89]. The figure shows an SEM image of a single water droplet ( $\sim 9 \mu\text{L}$ ) rolling on the microfiber adhesive contaminated with ceramic microspheres showing (a.1) the microfiber array with (a.2) a self-cleaned upper half and (a.3) a dirty lower half. **(b)** Schematics of dynamic self-cleaning in gecko via the mechanism of digital hyperextension [59]. Hu et al. proposed that when setae are suddenly released from an attached substrate, they generate enough inertial force to dislodge dirt particles that are on the spatulae. **(c)** Simulation steps for contact self-cleaning of high aspect ratio microfiber adhesives made from polypropylene [88] using a load-drag-unload procedure. A single cleaning cycle involves (c.1) applying a normal compressive force to press a contaminated adhesive against a clean substrate, (c.2) adding a shear load to the compressive load to drag the adhesive against the substrate, (c.3) removing the compressive load, and (c.4) detaching the sample from the substrate.

### 3.2.2 Mechanisms of Dynamic Self-cleaning

Self-cleaning of microfiber adhesive can also occur as a result of dynamic processes. Dynamic self-cleaning has been investigated for synthetic microfiber adhesives as well as for the gecko adhesive system [58, 121]. Two self-cleaning mechanisms in this category are:

**(III) Vibration and Agitation:** This involves self-cleaning of an array of microfibers due to vibrations of the system on which the adhesive is mounted. Self-cleaning by sample vibration has been studied by Sethi et al. for microfiber adhesives made from high aspect ratio carbon nanotubes, in which a 90% recovery was reported [121]. However, details of the vibration frequencies used were not given. Although it has not been widely investigated, sample vibration is a very practical and promising self-cleaning process.

**(IV) Digital Hyperextension:** Dynamic self-cleaning of microfiber adhesive by the mechanism of digital hyperextension [59] occurs when setae suddenly released from an attached substrate and generate enough inertial force to dislodge dirt particles attached to the spatulae (Fig. 3.3(b)). In their study, Hu et al. [59] showed that geckos that were able to use digital hyperextension experienced a self-cleaning rate that was approximately twice as fast as those that were restricted, with up to 80% adhesion recovery. Although dynamic self-cleaning by digital hyperextension has been proposed as a self-cleaning mechanism in geckos, it is also applicable to synthetic microfiber adhesives under peeling.

### 3.2.3 Mechanisms of Contact Self-cleaning

This category of self-cleaning is inspired by the initial work on self-cleaning in geckos by Hansen and Autumn [52]. Contact self-cleaning involves cleaning as a result of contact with a clean and dry substrate (Fig. 3.3(c)). The mechanisms of contact self-cleaning include:



**(V) Substrate Adhesion:** Self-cleaning via substrate adhesion occurs when the force of attraction between the dirt particles and a contacting substrate is greater than the force of attraction between the dirt particles and the microfiber adhesive. This is also known as *energy disequilibrium*. Substrate adhesion is currently the most widely used approach for manual cleaning of contaminated synthetic microfiber adhesives [53], but has recently been studied as a self-cleaning mechanism [44, 62, 88, 95]. Lee and Fearing [88] reported up to 35% recovery after cleaning their microfiber adhesive array made from polypropylene. Although they credited the recovery to the effect of substrate adhesion, the sole contribution of substrate adhesion is not known as their cleaning method involved a dragging step.

**(VI) Particle Sliding on Microfibers:** Contaminants and dirt particles can be removed from a microfiber adhesive in a process that involves the particles sliding across the tips of the adhesive, under shear loading. Particle sliding across the microfiber tips under the right loading conditions could potentially lead to the adhesion recovery, although it has so far been overlooked.

**(VII) Particle Rolling:** This self-cleaning mechanism which involves the rolling of contaminants was first proposed by Hui et al. based on the result of their work on the mechanics of self-cleaning in geckos [62]. Since that time, other researchers have attributed the self-cleaning of their microfiber adhesives under shear loading to a rolling mechanism, although no work has been done to verify this hypothesis.

## Summary

In summary, we identified and grouped seven (7) unique self-cleaning mechanisms for microfiber adhesives into three (3) major categories, namely wet, dynamic and contact self-cleaning. Based on our analysis, we believe that contact self-cleaning is a more practical approach to cleaning microfiber adhesives as it applies to a wider range of applications, and require little or no additional human intervention. For this reason, our work on self-cleaning

will henceforth be focused on dry contact-based self-cleaning mechanisms which include: *substrate adhesion*, *particle sliding on microfibers*, and *particle rolling*.

### **3.3 Mechanics of Contact Self-Cleaning of Microfiber Adhesives**

#### **3.3.1 Introduction**

##### **Overview of Previous Self-Cleaning Models**

Hansen and Autumn [52] developed the first model of contact cleaning for microfiber adhesives in their novel work on self-cleaning in geckos. The model described the substrate adhesion mechanism as the disequilibrium between the force pulling a dirt particle to a contacted wall and the force pulling the same particle to the adhesive. Based on this assumption, the number of spatulae  $N$  that must be attached to a single particle in order to prevent cleaning was determined. In their model, the adhesive force of the dirt particle with the wall was obtained using the Johnson-Kendall-Roberts (JKR) theory, and the adhesive force of the particle with the microfiber array was obtained as a product of  $N$  and the pull-off force of individual fibrils. Their model for the adhesive force of the microfiber interface was oversimplified since their microspheres were several times larger than the microfiber tip, so that all contacting fibrils do not pull-off simultaneously. Finally, in the model, the effect of preload force on adhesion at the microfiber interface was not taken into consideration. As discussed in Chapter 2, the adhesive force of a microfiber array with a sphere is strongly dependent on preload force.

Lee and Fearing [88] also developed a self-cleaning model for microfiber adhesives based on substrate adhesion. In their model, the JKR theory was used to obtain both the adhesive force at the microfiber/sphere interface and the sphere/wall interface. Similar to Hansen and Autumn, the use of the JKR theory for the sphere/wall interface limits the model to soft contaminants

only, which was not the case for their gold and polystyrene contaminants. Also, their model did not take the effect of preload force into consideration.

Hui et al. [62] developed a model of cleaning based on adhesion and rolling processes. In their model, they assumed that the contaminating particle was cylindrical and developed a model of adhesion for the microfiber interface using the JKR theory and elasticity, from a 2-dimensional perspective. Their model is based on the assumption that the pull-off force is obtained when the center microfiber has zero load. Previous experiments [51, 105] as well as results from our model in Chapter 2 shows that the deformation of the center microfiber as well as the number of contacting microfibers at pull-off is a function of the applied normal load. We also believe that a 3D pull-off analysis for spherical contaminants will more accurately describe the cleaning process.

The lack of a thorough analysis of contact cleaning and a supporting model is the inspiration for this section. Here, our goal is to present a detailed analysis that addresses the drawbacks of previous models, touches on the various contact self-cleaning mechanisms, and presents a clearer view of contact self-cleaning in microfiber adhesives.

### **Contaminants and their Size Regimes**

Similar to previous self-cleaning reports [44, 52, 59, 76, 88, 89, 95, 121], we will consider our ideal contaminant as a spherical particle. Apart from simplifying the model, the use of spherical contaminants allows for direct comparison of this work with previous self-cleaning experimental reports, all of which have used spherical contaminants. We will further group our contaminants into two (2) regimes based on the ratio  $\kappa$  of contaminant diameter  $D_s$  to microfiber-tip diameter  $D_f$ , i.e.  $\kappa = D_s/D_f$  (Fig. 3.4). In the small contaminant regime, the particle is much smaller than the microfiber tip, i.e.  $\kappa \ll 1$ . In the large contaminant regime, the contaminant is much larger than the microfiber tip i.e.  $\kappa \gg 1$ . The conditions for  $\kappa \approx 1$  leads to a more complicated analysis that will not be covered in this work.

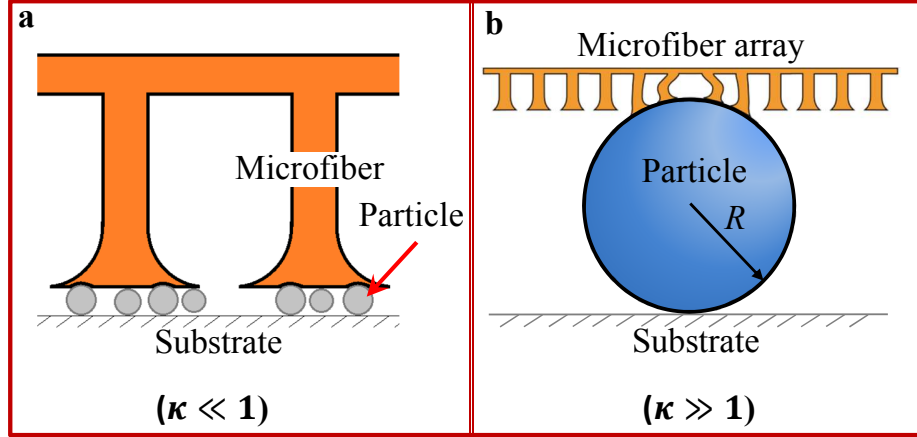


Figure 3.4: Schematics of contaminated microfiber adhesives showing contaminant size regimes.  $\kappa$  is the ratio of the contaminants diameter to microfiber-tip diameter. (a) Schematic of the small contaminant regime where the particles diameters are much smaller than the microfiber tip diameter and  $\kappa \ll 1$ . (b) Schematic of a single particle in contact with multiple microfibers in the large contaminant regime, where  $\kappa \gg 1$ .

### Contact Self-cleaning Procedures

Based on the definition of self-cleaning in Section 3.1.1, a "self-cleaning" procedure should involve the same steps implemented during the use of the adhesive. As shown in Fig. 3.5, the steps implemented for several applications of microfiber adhesives can be grouped into two procedures namely:

1. Load-Unload (LU) Procedure, and
2. Load-Drag-Unload (LDU) Procedure.

In the LU procedure (Fig 3.5(a)), the adhesive is loaded (pressed) against a contacting substrate until a desired preload force (or indentation distance) is reached, and later unloaded by pulling the adhesive away from the substrate perpendicularly. Such procedure is used for applications such as object manipulation and locomotion [78]. The LU procedure only involves normal load, and as a result, contact self-cleaning can only occur by the mechanism of substrate adhesion during the unloading step. In the LDU procedure (Fig 3.5(b)), after loading the adhesive against a contacting substrate it is dragged a desired distance, before it is finally unloaded. This

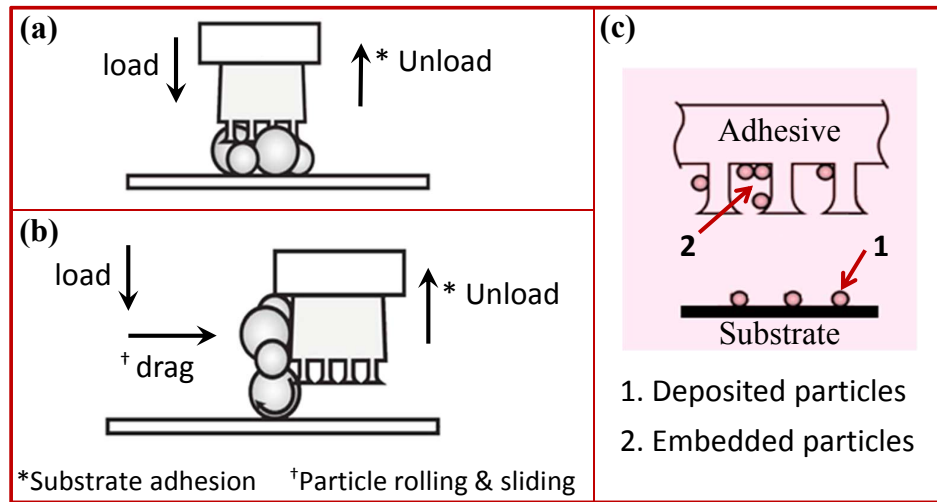


Figure 3.5: Schematic diagrams illustrating the contact self-cleaning procedures and particle displacements. **(a)** Diagram illustrating the load-unload contact self-cleaning procedure which involves loading a microfiber adhesive against a substrate until a desired preload force (or indentation distance) is reached, and later unloading by pulling the adhesive away from the substrate perpendicularly. **(b)** Diagram illustrating the load-drag-unload cleaning procedure, in which case, the adhesive is dragged a desired distance after loading, before it is finally unloaded. **(c)** Diagram shows self-cleaning particles that have been *deposited* unto a contacted substrate or *embedded* between adjacent microfibers.

procedure is commonly implemented in application of microfiber adhesives for wall climbing robots. As with the LU procedure, self-cleaning can occur by substrate adhesion during the unloading step, but self-cleaning can also occur during the dragging step by particle sliding and particle rolling mechanisms.

In the current analysis, we will assume a LDU procedure since it includes all possible mechanisms for contact self-cleaning.

### **Model Assumptions**

For the purpose of simplicity, we will make the following assumptions in our model:

1. All contacting surfaces are atomically smooth
2. The contaminant is a spherical particle
3. Deformations at the microfiber and substrate interface are small
4. Each microfiber is a homogeneous elastic cylinder with uniform circular cross section and flat mushroom-shaped tips
5. The particles and substrates are both rigid and has a modulus much larger than that of the microfibers
6. The weight of the particle is negligible

Henceforth, we shall refer to the contaminant-fiber boundary as the  $CF$  interface, and the contaminant-substrate boundary as the  $CS$  interface.

### **3.3.2 Contact Self-cleaning Model for Small Contaminants ( $\kappa \ll 1$ )**

In this regime, the particle diameter is much smaller than that of a single microfiber tip as shown in Figure 3.6. Also, recall our assumption that the modulus of the particle is much larger than that of the microfibers. As a result of these two conditions, we will treat the  $CF$  interface as that of a hard sphere indenting a half-space. The JKR model [70] is thus an appropriate model

for the  $CF$  interface because the microfibers are soft and have large adhesion energy, with a Tabor parameter  $\mu_{\text{Tabor}} > 5$  as given by the equation [131]

$$\mu_{\text{Tabor}} = \left( \frac{Rw^2}{E^{*2}z_0^3} \right)^{1/3}, \quad (3.1)$$

where  $z_0$  is the effective range of action of the adhesive force (mostly van der Waals force) and between 0.3 to 0.5 nm,  $R$  is the sphere radius,  $E^*$  is the effective modulus of the interface, and  $w$  is the work of adhesion of the interface. On the other hand, the  $CS$  interface is modeled using the (DMT) theory [34] which is applicable for the contact of a hard sphere with a hard substrate, with  $\mu_{\text{Tabor}} < 0.1$ .

**Self-cleaning by Substrate Adhesion:** The mechanics of the substrate adhesion mechanism is based on the disequilibrium of the forces attracting the particle to the microfiber array and the forces pulling the particle to a substrate. We denote the adhesive force at the  $CF$  interface as  $P_{\text{cf}}$  and the adhesive force at the  $CS$  interface as  $P_{\text{cs}}$ . Cleaning occurs when  $P_{\text{cs}} > P_{\text{cf}}$  (See Fig 3.6(a)). Using the JKR theory,  $P_{\text{cf}}$  is given as [70]

$$P_{\text{cf}} = \frac{3}{2}\pi w_{\text{cf}}R, \quad (3.2)$$

and  $P_{\text{cs}}$  is given by the DMT model as

$$P_{\text{cs}} = 2\pi w_{\text{cs}}R. \quad (3.3)$$

where  $w_{\text{cf}}$  and  $w_{\text{cs}}$  are the work of adhesion of the  $CF$  and  $CS$  interfaces, respectively.  $w$  is dependent on the surface energy of the contacting materials in the form  $w = \gamma_1 + \gamma_2 - \gamma_{12}$ , where  $\gamma_1$  and  $\gamma_2$  are the surface energy of the two surfaces, and  $\gamma_{12}$  is the interfacial energy ( $\gamma_{12} = 0$ ) for similar surfaces.

Let us define a cleaning coefficient  $\varrho$  such that cleaning occurs when  $\varrho > 1$ . The cleaning

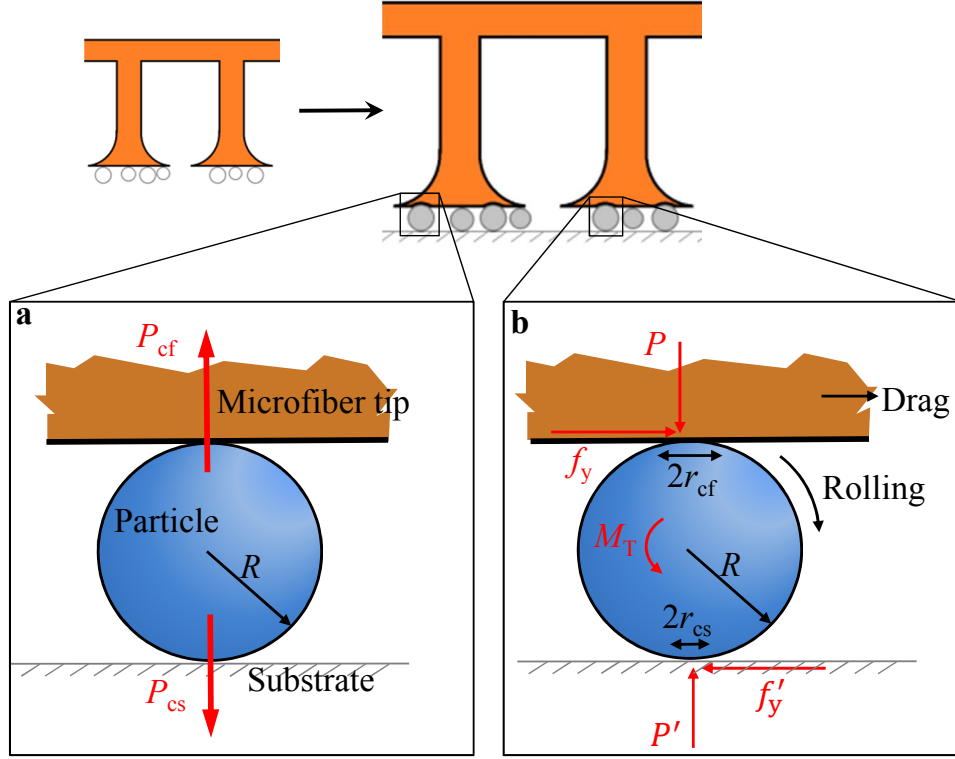


Figure 3.6: Loading conditions for a single particle sandwiched between a microfiber tip and a glass substrate during the load-drag-unload cleaning processes for the small contaminant regime ( $\kappa \ll 1$ ). **(a)** Schematic diagram of the forces acting on the particle during the unloading step. The forces acting on the particle are the adhesive force at the contaminant-substrate interface  $P_{cs}$  and the adhesive force at the contaminant-fiber interface  $P_{cf}$ . Self-cleaning occurs when  $P_{cs} > P_{cf}$ . **(b)** Forces acting on the particle during the drag step.  $P$  is the applied normal load,  $P'$  is the normal reaction force at the contaminant-substrate interface,  $r_{cs}$  and  $r_{cf}$  are the contact radii of the contaminant-substrate and contaminant-fiber interfaces, respectively,  $f_y$  is the applied shear force,  $f'_y$  is the friction force at the contaminant-substrate interface,  $M_T$  is the total rolling resistance on the particle, and  $R$  is the particle radius.



coefficient for the substrate adhesion mechanism in the small contaminants regime,  $\varrho_{\text{adh, I}}$  is the ratio of  $P_{\text{cs}}$  to  $P_{\text{cf}}$ , which can be obtained from Eqn.s 3.2 and 3.3 as

$$\varrho_{\text{adh, I}} = \frac{4}{3} \frac{w_{\text{cs}}}{w_{\text{cf}}}. \quad (3.4)$$

Equation 3.4 shows that cleaning by substrate adhesion mechanism is possible in the small contaminant regime if the work of adhesion of the  $CS$  interface is greater than 3/4 times the work of adhesion of the  $CF$  interface. Equation 3.4 also shows that the size of the particle does not influence the cleaning coefficient as long as the particles remain within the small contaminant regime.

**Self-cleaning by Particle Sliding and Rolling:** When a contaminated microfiber array is pressed against a substrate and sheared, there is a possibility for the particle to slide across either the microfiber, or the substrate surface, or roll on both surfaces. However, cleaning occurs only when the particle slides across the microfiber surface or rolls on both surfaces. Both cases require that the particle does not slide relative to the substrate.

Let  $f_y$  be the applied shear force on the microfiber (See Fig 3.6(b)). Under a small normal load  $P$ , the critical shear force  $f'_{\text{cf}}$  required for the particle to slide with respect to the microfiber is given as

$$f'_{\text{cf}} = \tau_{\text{cf}} (\pi r_{\text{cf}}^2) + \mu_{\text{cf}} P, \quad (3.5)$$

and the critical shear force required for the particle to slide along the substrate  $f'_{\text{cs}}$  is given as

$$f'_{\text{cs}} = \tau_{\text{cs}} (\pi r_{\text{cs}}^2) + \mu_{\text{cs}} P. \quad (3.6)$$

where  $\tau$ ,  $\mu$ ,  $r$  are the shear strength, coefficient of friction and the contact radius, respectively of the interface. In equations 3.5 and 3.6, the first term accounts for the constant friction stress, while the second term accounts for the Coulomb friction contributions at the interfaces. The

constant friction stress term dominates for soft and adhesive contact interfaces at low normal load, while Coulomb friction dominates for hard contact interfaces and high normal loads. In this analysis, the first term will dominate in equation 3.5 for a soft  $CF$  interface, whereas the second term will dominate in equation 3.6 for the hard  $CS$  interface, for small normal loads. The contact radius for each interface can be obtained from the JKR and DMT contact models for the  $CS$  and  $CF$  interfaces, respectively as [94]

$$r_{cf}^3 = \frac{R}{K_{cf}} \left[ P + 3w_{cf}\pi R + \sqrt{6w_{cf}\pi RP + (3\pi w_{cf}R)^2} \right], \quad (3.7)$$

and

$$r_{cs}^3 = \frac{R}{K_{cs}} (P + 2w_{cs}\pi R), \quad (3.8)$$

where  $1/K_{12} = (3/4) [(1 - \nu_1^2)/E_1 + (1 - \nu_2^2)/E_2]$ ,  $E$  is the Young's modulus and  $\nu$  is the Poisson's ratio of the respective contacting surfaces noted by subscripts 1 and 2.

Based on experimental and theoretical values of reported shear strength at different scales of contact radii, Sumer and Sitti [129] have shown that the interface shear strength is a function of the contact radius except for very small contact radii (less than 20 nm) where  $\tau \approx G_{12}/43$  [57] and large contact radii (larger than 40  $\mu\text{m}$ ) where  $\tau \approx G_{12}/1290$  [23].

$$\tau = \begin{cases} G_{12}/43 & r < 20 \text{ nm} \\ G_{12}10^n \left(\frac{r_{12}}{b}\right)^m & 20 \text{ nm} < r < 40 \mu\text{m} \\ G_{12}/1290 & r > 40 \mu\text{m} \end{cases} \quad (3.9)$$

where  $m = \tan^{-1}[(G_{12}/43 - G_{12}/1290)/(8 \times 10^4 b - 28b)]$ ,  $n = 28b$  and  $b = 0.5 \text{ nm}$  is the Burgers vector,  $G_{12} = 2G_1G_2/(G_1 + G_2)$ ,  $G_1$  and  $G_2$  are the shear moduli of the materials, and  $G_i = E_i/2(1 + \nu_i)$ .

In the case of particle rolling, Dominik and Tielens [35] have shown using the JKR theory

that the rolling resistance  $M$  for micron and submicron sized spherical particles is given by

$$M = 6\pi R w \xi \quad (3.10)$$

where  $\xi$  is the critical rolling distance for irreversible rolling. In their work, Dominik and Tielens accounted for both the work done in breaking the bond behind the rolling contact and the work done by the adhesive forces forming ahead of the rolling contact. The value of  $\xi$  ranges from the interatomic distance  $\varepsilon$  to the contact radius such that  $\varepsilon \leq \xi \leq r$ . We denote  $M_{cs}$  and  $M_{cf}$  as the rolling resistances at the  $CS$  and  $CF$  interfaces, respectively. From Equation 3.10,  $M_{cs} = 6\pi R w_{cs} \xi_{cs}$  and  $M_{cf} = 6\pi R w_{cf} \xi_{cf}$ , and the overall rolling resistance  $M_T$  due to the two interfaces is given as

$$M_T = 6\pi R (\xi_{cf} w_{cf} + \xi_{cs} w_{cs}) . \quad (3.11)$$

Static equilibrium requires that  $M_T = 2f_y R$ . By substituting for  $M_T$  in the above equation, we obtain the critical shear force for rolling  $f'_R$  as

$$f'_R = 3\pi (\xi_{cf} w_{cf} + \xi_{cs} w_{cs}) \quad (3.12)$$

Combining equations 3.5, 3.6 and 3.12, the conditions for self-cleaning based on sliding or rolling mechanism is obtained as

$$\tau_{cs} (\pi r_{cs}^2) + \mu_{cs} P > f_y \geq \begin{cases} \tau_{cf} (\pi r_{cf}^2) + \mu_{cf} P & \text{Sliding on microfiber,} \\ 3\pi (\xi_{cf} w_{cf} + \xi_{cs} w_{cs}) & \text{Rolling.} \end{cases} \quad (3.13)$$

As shown in equation 3.13, cleaning does not occur if  $f_y$  is greater than the critical sliding force at the substrate interface given in equation 3.6. The cleaning coefficient for particle sliding in

the small contaminants regime is given as

$$\varrho_{\text{slide, I}} = \frac{f_y}{\tau_{\text{cf}} (\pi r_{\text{cf}}^2) + \mu_{\text{cf}} P} \quad (3.14)$$

and the cleaning coefficient for particle rolling in the small contaminants regime is

$$\varrho_{\text{roll, I}} = \frac{f_y}{3\pi (\xi_{\text{cf}} w_{\text{cf}} + \xi_{\text{cs}} w_{\text{cs}})} \quad (3.15)$$

The above model for cleaning under shear loading is applied to a glass particle with  $D_s = 46.2 \mu\text{m}$ , the Young modulus  $E_s = 73 \text{ GPa}$ , Poissons ratio  $\nu_s = 0.17$ , friction coefficient with substrate  $\mu_{\text{cs}} = 0.9$  and work of adhesion with substrate  $w_{\text{cs}} = 56 \text{ mJm}^{-2}$ . The particle is sandwiched between a glass substrate and a single elastomer microfiber with  $D_f = 95 \mu\text{m}$ , microfiber length  $L = 105 \mu\text{m}$ , microfiber edge-to-edge spacing  $S = 75 \mu\text{m}$ , Young modulus  $E_f = 2.9 \text{ MPa}$ , Poissons ratio  $\nu_f = 0.49$ , friction coefficient with glass  $\mu_{\text{cf}} = 0.9$  [110] and work of adhesion with glass  $w_{\text{cf}} = 93 \text{ mJm}^{-2}$ . Figure 3.7 shows a shear-based cleaning map obtained from equation 3.13 using the above parameters. The graph shows that cleaning can occur by particle sliding on the microfiber or rolling, where particle sliding across the microfiber dominates when  $P < 15 \mu\text{N}$  (inset), particle rolling dominates for  $P > 15 \mu\text{N}$ , and the particle can be cleaned by particle rolling with slipping along the microfiber tip at  $P = 15 \mu\text{N}$ .

### 3.3.3 Contact Self-cleaning Model for Large Contaminants ( $\kappa \gg 1$ )

For particles with diameter much larger than the microfiber tip as shown in Fig. 3.8, several microfibers can simultaneously be in contact with the particle. In this case, the  $CS$  interface is the same as with the small contaminants regime, on the other hand, the  $CF$  interface is more complex and will be addressed using the model developed in Chapter 2.

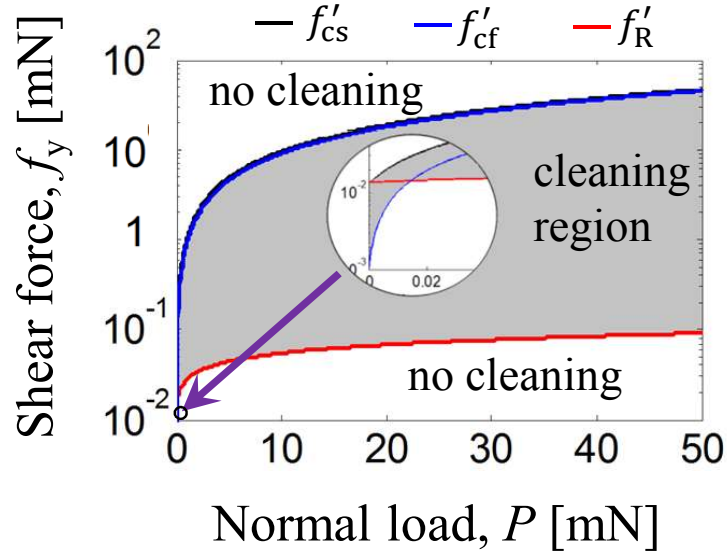


Figure 3.7: Contact self-cleaning map for a  $46.2 \mu\text{m}$  diameter glass particle in the small contaminant regime shows the vertical and lateral loads that result in contact self-cleaning (grey region) by particle rolling or sliding as predicted by equation 3.13.  $f'_{cs}$  (black line),  $f'_{cf}$  (blue line) and  $f'_R$  (red line) represents the critical shear forces required for the particle to slide with respect to the glass substrate, slide with respect to the microfiber surface, and roll on both surfaces, respectively. The graph shows that the cleaning mechanism during dragging motion would be dominated by rolling when  $f_y > 0.015 \mu\text{N}$  (see inset) and by sliding along the microfiber interface otherwise. The result is for a glass particle with  $D_s = 46.2 \mu\text{m}$ , the Young modulus  $E_s = 73 \text{ GPa}$ , Poissons ratio  $\nu_s = 0.17$ , friction coefficient with substrate  $\mu_{cs} = 0.9$  and work of adhesion with substrate  $w_{cs} = 56 \text{ mJm}^{-2}$ ; that is sandwiched between a glass substrate and a single elastomer microfiber with  $D_f = 95 \mu\text{m}$ , microfiber length  $L = 105 \mu\text{m}$ , microfiber edge-to-edge spacing,  $S = 75 \mu\text{m}$ , Young modulus  $E_f = 2.9 \text{ MPa}$ , Poissons ratio,  $\nu_f = 0.49$ , friction coefficient with glass  $\mu_{cf} = 0.9$  [110] and work of adhesion with glass  $w_{cf} = 93 \text{ mJm}^{-2}$ .

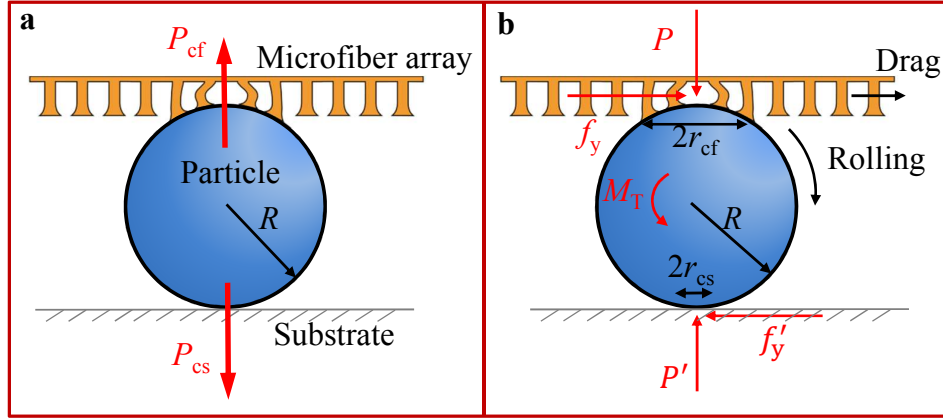


Figure 3.8: Loading conditions for a single particle sandwiched between a microfiber array and a glass substrate during the load-drag-unload cleaning processes for the large contaminant regime ( $\kappa \gg 1$ ). **(a)** Schematic diagram of the forces acting on the particle during the unloading step. The forces acting on the particle are the adhesive force at the contaminant-substrate interface  $P_{cs}$  and the adhesive force at the contaminant-fiber interface  $P_{cf}$ . Self-cleaning occurs when  $P_{cs} > P_{cf}$ . **(b)** Forces acting on the particle during the drag step.  $P$  is the applied normal load,  $P'$  is the normal reaction force at the contaminant-substrate interface,  $r_{cs}$  and  $r_{cf}$  are the contact radii of the contaminant-substrate and contaminant-fiber interfaces, respectively,  $f_y$  is the applied shear force,  $f'_y$  is the friction force at the contaminant-substrate interface,  $M_T$  is the total rolling resistance on the particle, and  $R$  is the particle radius.

**Self-cleaning by Substrate Adhesion:** Similar to the small contaminants regime, a dirt particle can be self-cleaned by substrate adhesion when the adhesive force attracting the particle to the substrate is greater than the adhesive force attracting the particle to the microfibers. Here, adhesive force at the  $CS$  interface can be obtained from the DMT model, similar to that of the small contaminants regime as

$$P_{cs} = 2\pi w_{cs}R. \quad (3.16)$$

For the  $CF$  interface, several microfibers make contact with the particle and the adhesive force will be due to the contributions of all the individual microfibers in contact. From intuition, we may expect the adhesive force of the interface  $P_{cf}$  to be in the form  $N \times F_c$ , where  $N$  is the number of microfibers in contact with the particle and  $F_c$  is the adhesive force of individual microfibers. However, this is not the case since all the contacting microfibers do not pull-off simultaneously, as discussed in Section 2.3.2. Here, a more accurate value of the adhesive force for a sphere in contact with a microfiber interface is obtained from simulation. As previously shown,  $P_{cf}$  is a function of several factors such as the preload force, microfiber shape and material properties, as well as the size of the particle. A detailed procedure for obtaining  $P_{cf}$  has been presented in Section 2.3.2. Similar to the small contaminants regime, the cleaning coefficient for the large contaminants regime  $\varrho_{adh, II}$  is given as

$$\varrho_{adh, II} = \frac{P_{cs}}{P_{cf}} \quad (3.17)$$

Figure 3.9 shows a cleaning map for a microfiber array with  $D_f = 25\mu\text{m}$ ,  $S = 15\mu\text{m}$ ,  $E_f = 2.9 \text{ MPa}$ ,  $\nu_f = 0.49$ ,  $w_{cf} = 93 \text{ mJ/m}^2$ , which is contaminated by glass spheres with radius ranging from 0.05 mm to 10 mm, for various preload forces. The contacting substrate is a glass slide with  $E_s = 73 \text{ GPa}$ ,  $\nu_s = 0.17$ ,  $w_{cs} = 56 \text{ mJ/m}^2$ . The result shows that cleaning by the adhesion process is achievable for large particles especially with low normal preloads. Under low loads, fewer microfibers are in contact with a single particle, so that the adhesive force

of the microfibers interface is more likely to be less than that of the substrate, which is the necessary condition for self-cleaning by substrate adhesion.

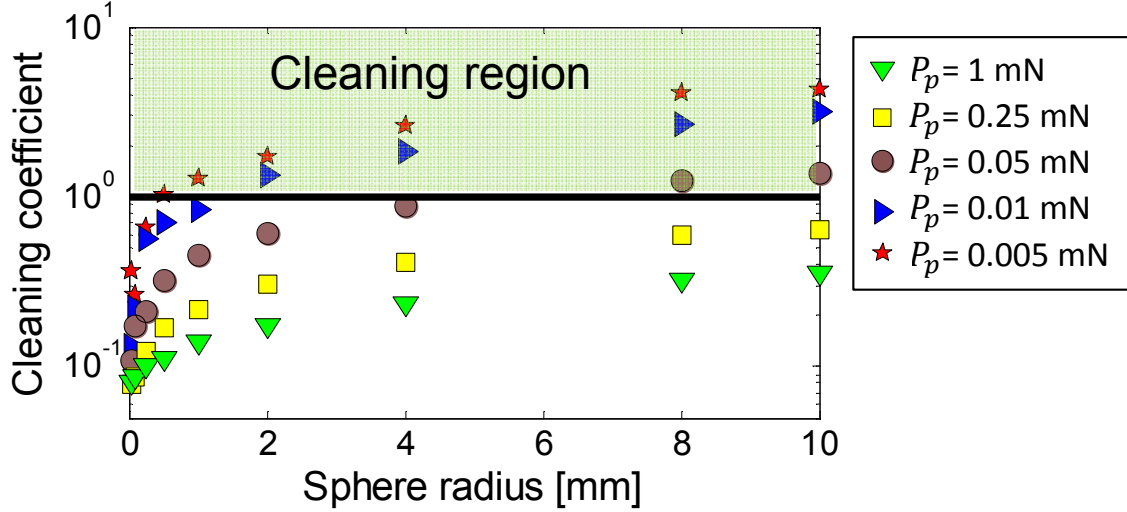


Figure 3.9: Coefficient of cleaning by adhesion process. The results show that cleaning by the adhesion process is achievable for large particles, and that lower preload force is favorable for cleaning. The result is for a microfiber array ( $D_f = 25\mu\text{m}$ ,  $S = 15\mu\text{m}$ ,  $E_f = 2.9\text{ MPa}$ ,  $\nu_f = 0.49$ ,  $w_{cf} = 93\text{ mJ/m}^2$ ), contaminated by glass spheres with diameter ranging from 0.05 mm to 10 mm, and contacting a glass substrate ( $E_s = 73\text{ GPa}$ ,  $\nu_s = 0.17$ ,  $w_{cs} = 56\text{ mJ/m}^2$ ). The preload force was varied from 0.005 mN to 1 mN. Each data point represents the mean of 10 simulations. The standard deviation of each data point is negligible.

**Self-cleaning by Particle Sliding and Rolling:** The critical shear force required to facilitate sliding at the contaminant-substrate interface for the large contaminants regime is the same as with the small contaminants regime and given as

$$f''_{cs} = \tau_{cs} (\pi r_{cs}^2) + \mu_{cs} P. \quad (3.18)$$

For the  $CF$  interface, we have several contacting fibrils in place of a single contact interface in the small contaminants regime. For simplicity, we will assume that the applied normal load is small so that none of the microfibers is buckled and linear elasticity is upheld. Next, let us represent the reaction force of each microfiber as a point load acting on the particle surface.



If we consider the distribution of the forces on the particle, it will be similar to a pressure distribution in Hertzian contact. Now, we can use a similar equation to the small contaminants regime as

$$f_{\text{cf}}'' = \tau_{\text{cf}} (\pi r_{\text{cf}}^2) + \mu_{\text{cf}} P. \quad (3.19)$$

In this case, the contact radius  $r_{\text{cf}}$  is obtained from the model for a microfiber array in Section 2.3.2 as

$$r_{\text{cf}}^4 = \frac{4CPR}{\pi\rho}, \quad (3.20)$$

where  $\rho$  is the density of the microfiber array and  $C$  is the compliance of a single microfiber given in equation 2.5.

Similarly, our assumption of elastic deformation of the microfibers allows us to adopt the rolling contact mechanics developed by Dominik and Tielens [35] as an approximate solution for rolling resistance in the large contaminants regime. As derived in the small contaminants regime, the critical shear force for rolling is

$$f_{\text{R}}'' = 3\pi (\xi_{\text{cf}} w_{\text{cf}} + \xi_{\text{cs}} w_{\text{cs}}). \quad (3.21)$$

However, the values of  $\xi_{\text{cf}}$  in Equation 3.21 is expected to be much larger compared to the small contaminants regime due to an increased contact radius at the  $CF$  interface.

Thus, the condition for self-cleaning by particle sliding and rolling in Equation 3.13 is also applicable to the large contaminants regime, where  $r_{\text{cf}}$  is obtained from equation 3.20. However, for the large contaminants regime, we expect higher values for the critical friction force at the adhesive interface, and the critical rolling force, so that the cleaning region shown in Fig. 3.7 will be smaller.

### 3.4 Summary

In this chapter, we covered the mechanisms of self-cleaning for microfiber adhesives and presented the mechanics of contact self-cleaning for microfiber adhesives. An overview of self-cleaning of fibrillar adhesives was presented along with a well-rounded definition of self-cleaning for fibrillar adhesives that took into account the two possible modes of contaminant displacement, namely deposition and embedding. We identified three (3) major categories of self-cleaning in microfiber adhesives namely wet, dynamic and contact self-cleaning, along with seven (7) self-cleaning mechanisms which includes rolling of water droplets and capillary adhesion under wet self-cleaning, sample vibration/agitation and digital hyperextension under dynamic self-cleaning, substrate adhesion, particle sliding on microfibers and particle rolling under contact self-cleaning. Of the self-cleaning categories, we believe that contact self-cleaning is the more practical approach to self-cleaning as it applies to a broad range of applications and can be achieved based on the current application procedure, with little or no additional human intervention.

To model the mechanics of contact self-cleaning, spherical particles were used as idealized contaminants for simplification and to allow for direct comparison of our model with previous self-cleaning studies, all of which used microspheres as contaminants. We will analyze one of such studies in the next chapter along with new experiments and compare the results with the model presented here. The contaminants were divided into small and large contaminant regimes (labeled small and large contaminants regimes, respectively), based on the ratio of the contaminant diameter to the diameter of the microfiber tips. This allowed for a thorough analysis of all loading scenarios. In each regime, we modeled cleaning by substrate adhesion, particle sliding and particle rolling mechanisms. In the small contaminants regime, cleaning by adhesion process was independent of the size of the particle or the geometric properties of the adhesive; rather it was solely dependent on the work of adhesion of the interfaces. Cleaning could only occur by adhesion in the large contaminants regime if the work of adhesion of the contaminant-

substrate interface was greater than  $3/4$  times that of the contaminant-fiber interface. Results from a case study for shear loading in the small contaminants regime showed that cleaning is achievable in most loading conditions, where sliding dominates for very small vertical loads and rolling dominates for high loads. The same was the case in the large contaminants regime, where the model results indicated that large particles can be cleaned easily by the adhesion process as long as the applied preload force was low. However, for self-cleaning by particle rolling and sliding in the large contaminants regime, the model predicts higher values for the critical friction force at the adhesive interface, and the critical rolling force, so that the cleaning region is smaller.

Although the model presented here is very thorough and extensive, future work in this area should include the effect of different particle shapes and roughness, as well as fiber and tip geometries. We will evaluate the proposed model through experiments in the following chapter.

# **Chapter 4**

## **Experiments and Simulation of Contact**

### **Self-cleaning of Microfiber Adhesives**

#### **4.1 Introduction**

In this chapter, we present contact self-cleaning experiments and simulations there were conducted using the load-drag-unload (LDU) procedure. First, results of initial experiments are presented and analyzed in Section 4.2 for the cleaning performance of the various contaminant regimes. The adhesion recovery and anti-fouling of the experiments will be compared to theoretical models presented in the previous chapters. Although the experiments give a good insight into contact self-cleaning and show the effect of contaminant sizes and the contribution of the normal loading and dragging steps, it does not tell much about the underlying mechanism of contact self-cleaning using the LDU procedure. As a result, further experiments are conducted and presented in Section 4.3 to uncover the underlying mechanism of contact self-cleaning based on the LDU procedure. The effect of normal load and dragging speed on the rolling friction of a particle on a microfiber adhesive are also presented and modeled. Based on insights from the experiments and the uncovered contact self-cleaning mechanism, a procedure for simulating contact self-cleaning for the case similar to the experiments is presented in

Section 4.4 and the results are compared to the experimental results. Finally, a summary of the results acquired from the experiments, models and simulation of contact self-cleaning will be presented in Section 4.5.

## **4.2 Experiment I: Effect of Contaminant Size Regimes on the Contact Self-cleaning Performance of Microfiber Adhesives**

This section presents an experimental procedure and results of the remarkable adhesion recovery of contaminated microfiber adhesives with high adhesive strength, via contact self-cleaning mechanisms. The experiments were designed and conducted by my collaborators (Y. Menguc and M. Rohrig) using a load-drag-unload cleaning procedure similar to the loading procedure of the gecko toes during use [52], or the loading procedure of microfiber adhesives in some areas of application such as robotics [136]. Although the experiments cover the large, small and intermediate contaminant regimes, we will focus our analysis on the small and large contaminant regimes both of which were modeled in the previous chapter. Apart from the self-cleaning, we will also investigate the anti-fouling performance which is the ability of a microfiber adhesive to retain some adhesiveness immediately after contamination.

### **4.2.1 Experimental Methodology**

Three sizes of polyurethane elastomer microfibers with mushroom-shaped tips and a flat unstructured reference patch were fabricated using a lithographic and dipping process combined with soft mold casting [102]. Table 4.1 shows the dimensions of the elastomer microfiber adhesives with tip diameters  $D_f$  of 20, 30 and 95  $\mu\text{m}$  and corresponding lengths  $L$  of 25, 50 and 105  $\mu\text{m}$  for the small, medium and large microfiber samples, respectively. The microfiber adhesives

were made from polyurethane (ST-1060, BJB Enterprises) with a Young modulus  $E_f$  of 2.9 MPa and a work of adhesion to glass  $w_{cf}$  of 93 mJ/m<sup>2</sup>. The adhesive samples, including a flat unstructured sample, were cut into squares of 0.5 mm  $\times$  0.5 mm, and affixed to a clear acrylic plate using a double-sided adhesive tape. Commercially pre-cleaned glass slides (Microscope Slide, Pearl) were used as substrates. Prior to using the glass slides, they were cleaned with lint-free lens paper and blasted with compressed air.

Glass spheres with diameters ranging from 3 to 215  $\mu\text{m}$  were used as contaminants in the experiments (Tab. 4.1). The microspheres were originally packed in dry air by the supplier and used as is. The mean diameters  $D_s$  and standard deviations of the microspheres were determined by analyzing microscope images with customized software as follows:

- S1:  $D_s = 2.8 \pm 1.7 \mu\text{m}$ , ‘GL-0191 1 15  $\mu\text{m}$ ’, MO-SCI Specialty Products
- S2:  $D_s = 46.2 \pm 5.8 \mu\text{m}$ , ‘SLGMS 45 - 53  $\mu\text{m}$ ’, Cospheric
- S3:  $D_s = 118.5 \pm 18.1 \mu\text{m}$ , ‘BBI-8541400’, Sartorius
- S4:  $D_s = 123.6 \pm 26.5 \mu\text{m}$ , ‘BBI-8541507’, Sartorius
- S5:  $D_s = 213.6 \pm 28.9 \mu\text{m}$ , ‘type 1922’, Potters Industries

The experiments were conducted using a custom-built 3-axis motion control system (similar to that shown in Fig 4.4 but with the exception of the horizontal axis load cell), that was mounted onto an inverted optical microscope (Eclipse LE200, Nikon). The system consisted of linear stages (MFA-CC and VP-25XA, Newport) that were used to move the adhesive sample in the vertical-axis for normal loading, and to move the substrate in the horizontal-axis during dragging. The normal force applied to the adhesive sample was captured using a load cell and signal amplifier (GSO-50 and TMO-2, Transducer Techniques) via a data acquisition board (NI PCI-6259, National Instruments). Alignment of the setup was achieved using two manual rotational stages (GON40-U, Newport) for rotation across the X- and Y-axis. A colored digital video camera (DFW-X710, Sony) was mounted onto the microscope and used to capture the visual information during the experiments. A customized software was used to control the system

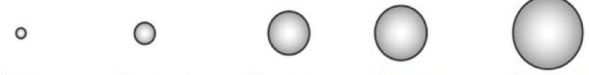
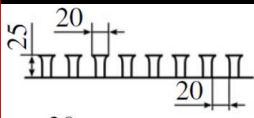
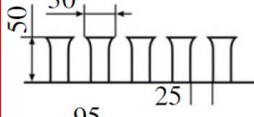
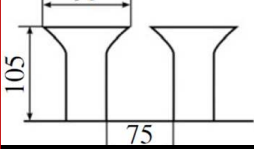
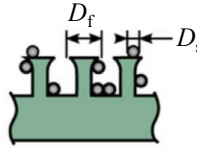
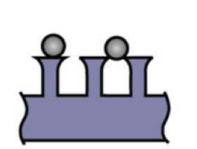
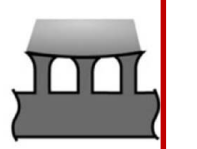
$D_s [\mu\text{m}]$						
$D_f [\mu\text{m}]$		$\varnothing 2.8$	$\varnothing 46.2$	$\varnothing 118.5$	$\varnothing 123.6$	$\varnothing 213.6$
		0.14	2.31	5.93	6.18	10.68
		0.09	1.54	3.95	4.12	7.12
		0.03	0.49	1.25	1.30	2.25
		$D_s \ll D_f$		$D_s \approx D_f$		$D_s \gg D_f$
Contaminant Regimes						
		$\kappa \ll 1$		$\kappa \approx 1$		$\kappa \gg 1$

Table 4.1: Dimensions of the microfiber adhesive samples and contaminating microspheres that were used in the experiments. The samples were grouped into small ( $\kappa \ll 1$ ), intermediate ( $\kappa \approx 1$ ) and large ( $\kappa \gg 1$ ) contaminant regimes.  $D_s$  is the microfiber tip diameter,  $D_s$  is the mean particle diameter and  $\kappa = D_s/D_s$ .  $\varnothing$  refers to the diameter dimension of the particles.

and to record time-stamped visual and force data for analysis.

Contamination of a sample was achieved by first pressing the sample against a monolayer of microspheres at a speed of  $25 \mu\text{m/s}$  until a predetermined compressive force was reached - 10 mN (25 kPa) for small samples, 15 mN (60 kPa) for medium samples, and 50 mN (200 kPa) for large samples. The sample was then retracted at the same speed as the loading speed. A disperse monolayer of glass spheres was created using one of the following three approaches depending on the size of the microspheres: for microspheres with  $D_s > 150 \mu\text{m}$ , it was sufficient to manually pour the particles onto a glass slide, where they settled through gravity into a monolayer; microspheres with  $15 \mu\text{m} < D_s < 150 \mu\text{m}$  were first poured onto a glass slide, and then pressed with a glass cover slip to create a monolayer; for microspheres with  $D_s < 15 \mu\text{m}$ , an aluminum

surface was first dusted with the spheres, next, a glass slide was electrostatically charged by rubbing it with a piece of lint-free lens paper, and the charged glass slide was brought near the dusted surface until the spheres were attached to the glass slide to create a monolayer.

Adhesion (pull-off force) measurements were carried out under normal loading by first compressing each sample against a clean glass substrate until a desired force (preload) was reached. Next, the sample was pulled away perpendicular to the substrate until it broke contact with the substrate. The preloads used in the experiments were 10 mN (40 kPa) for small adhesive samples, 15 mN (60 kPa) for the medium adhesive samples, and 50 mN (200 kPa) for the large adhesive samples. These preload values were chosen to maximize the attachment force and were determined by analyzing the adhesion for a wide range of preloads.

The entire cleaning experiments were conducted in following procedure. First, the initial adhesive force of a clean sample was measured and recorded as the *clean adhesion* ( $P_{\text{clean}}$ ). Secondly, the sample was contaminated by bringing it into contact with a monolayer of glass spheres. Thirdly, the adhesive force of the contaminated sample was measured immediately after contamination and recorded as the *contaminated adhesion* ( $P_{\text{dirty}}$ ). Fourthly, the sample was cleaned against a glass substrate using a load-drag-unload procedure. In the fifth step, the adhesion of the sample was measured again after cleaning as ( $P_{\text{cleaned}}$ ). Finally, the fourth and fifth steps were repeated successively with alternating drag directions. An alternating drag direction was used to prevent possible microfiber fatigue and failures of the double-sided adhesive tape used to attach the sample to the testing apparatus. Following this procedure, a total of 1040 experiments were performed on 24 adhesive samples ( $0.5 \text{ mm} \times 0.5 \text{ mm}$  area). The glass substrate was cleaned when contaminated, by wiping with a dry piece of lens paper and blasting with compressed air.

The contaminated samples were cleaned using a load-drag-unload procedure presented in Chapter 3. First, the sample was compressed (loaded) against a glass substrate at a rate of  $25 \mu\text{m/s}$  until a desired preload of 100 mN (400 kPa) was reached. Next, the glass substrate was



laterally displaced (dragged) while keeping the preload constant for 750  $\mu\text{m}$  at a drag speed of 50  $\mu\text{m/s}$ . Finally the sample was retracted (unloaded) at 25  $\mu\text{m/s}$  until there was no contact with the substrate. Each cleaning cycle was carried out on a clean section of the glass substrate. Apart from the specified preload, three samples were cleaned with lower preloads to test the sensitivity of the cleaning performance to this parameter: two samples of small-sized structures were cleaned at a preload of 20 mN (80 kPa) and a patch of medium sized structures was cleaned at a preload of 30 mN (120 kPa). Qualitatively and quantitatively, these adhesive samples were equivalent in their self-cleaning performance and were included in the test results.

## 4.2.2 Results and Discussions

To analyze the cleaning performance, let us define a *relative adhesion* as the measured adhesive force of the contaminated sample  $P_{\text{cleaned}}$  as a percentage of the measured adhesive force  $P_{\text{clean}}$  prior to contamination, so that

$$\text{Relative adhesion} = \frac{P_{\text{cleaned}}}{P_{\text{clean}}} \times 100\%. \quad (4.1)$$

Figure 4.1 shows graphs of the adhesion recovery for all contaminant regimes as well as the flat sample and Fig. 4.2 shows the Scanning Electron Microscopy (SEM) images of samples in the three (3) contaminant regimes before and after cleaning. Both figures show adhesion recovery for all samples. As shown in Figure 4.2, cleaning by *particle embedding* which was introduced in Chapter 3 was observed in the experiments. Let us now discuss the results of the adhesion recovery, and anti-fouling performances of the microfiber adhesives.

### Adhesion Recovery

Figure 4.1 shows the relative adhesion as a function of the cleaning cycles for all three contaminants size regimes, as well as the flat control sample. From the graphs, the large contaminant

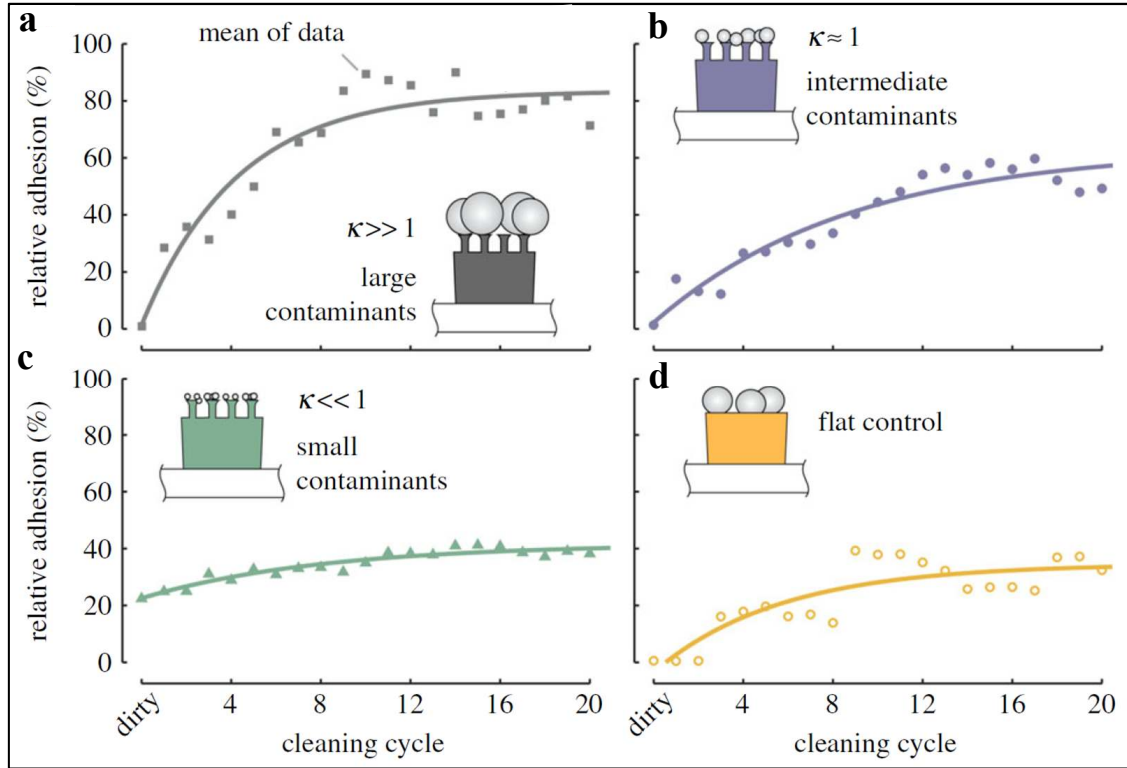


Figure 4.1: Self-cleaning experiment results showing the relative adhesion for the large, intermediate and small contaminant regimes, and the flat control sample. **(a)** Graph of relative adhesion after several cleaning cycles for the large contaminant regime ( $\kappa \gg 1$ ) shows a fast adhesion recovery of up to 80% after 9 cleaning cycles from a negligible adhesion immediately after contamination. (Each data point is the average result from 5 samples). **(b)** Relative adhesion plotted against cleaning cycles for the intermediate contaminant regime ( $\kappa \approx 1$ ) shows a gradual adhesion recovery of up to 55% after 12 cleaning cycles from a negligible adhesion value immediately after contamination. (Each data point is the average result from 6 samples). **(c)** Graph of relative adhesion plotted against cleaning cycles for the small contaminant regime ( $\kappa \ll 1$ ) shows a maximum recovery of 40% after 11 cleaning cycles from an initial value of 22% immediately after contamination. (Each data point is the average result from 8 experiments). **(d)** Graph of relative adhesion for the flat control shows maximum recovery of 35% after 20 cleaning cycles from a negligible value before the first cycle. (Each data point is the average of 8 experiments). Relative adhesion is defined in Equation 4.1.  $\kappa$  is the ratio of the particle diameter to the microfiber tip diameter. The solid lines are guide to the eyes

regime shows the highest adhesion recovery followed by the intermediate and small contaminant regimes. The relative adhesion in the large contaminant regime saturated at 80% recovery after 9 cleaning cycles with the number of tested samples  $N_{\text{samples}} = 5$ . In the intermediate contaminant regime, the adhesion reached 55% of clean adhesion in only 12 cleaning cycles ( $N_{\text{samples}} = 6$ ). The adhesion recovery saturated to 40% for the small contaminant regime in 11 cleaning cycles ( $N_{\text{samples}} = 8$ ). For the flat control sample, we found that only very large particles could be cleaned. The overall performance of the control was worse than that of all the microfiber samples, with adhesion recovery of approximately 35% after 20 cleaning cycles ( $N_{\text{samples}} = 5$ ).

We believe that the poor adhesion recovery for the small contaminant regime and the control samples is due to the microfiber deforming around the particle and making direct contact with the substrate during the cleaning steps. When this occurs, the microfiber tip does not move laterally relative to the substrate (or only moves by stick-slip motion) during dragging, so that particle sliding or rolling is inhibited. This condition is easily reached after the first few cleaning cycles for the small contaminant regime, such that no further cleaning is observed in subsequent steps even though contaminants are still present on the microfiber tip. An SEM image of the small contaminant regime in Fig. 4.2 shows some contaminants on the microfiber tips even after several cleaning cycles.

On the other hand, SEM images of the large and intermediate contaminant regimes in Fig. 4.2 show complete removal of the contaminants from the microfiber adhesive, but adhesion recovery in the large contaminant regime climaxed at 80 %. The 20% unrecoverable adhesion after cleaning is due to damage to the microfibers as can be seen in the SEM image. We believe that the damage occurred due to the high normal load used in the experiment.

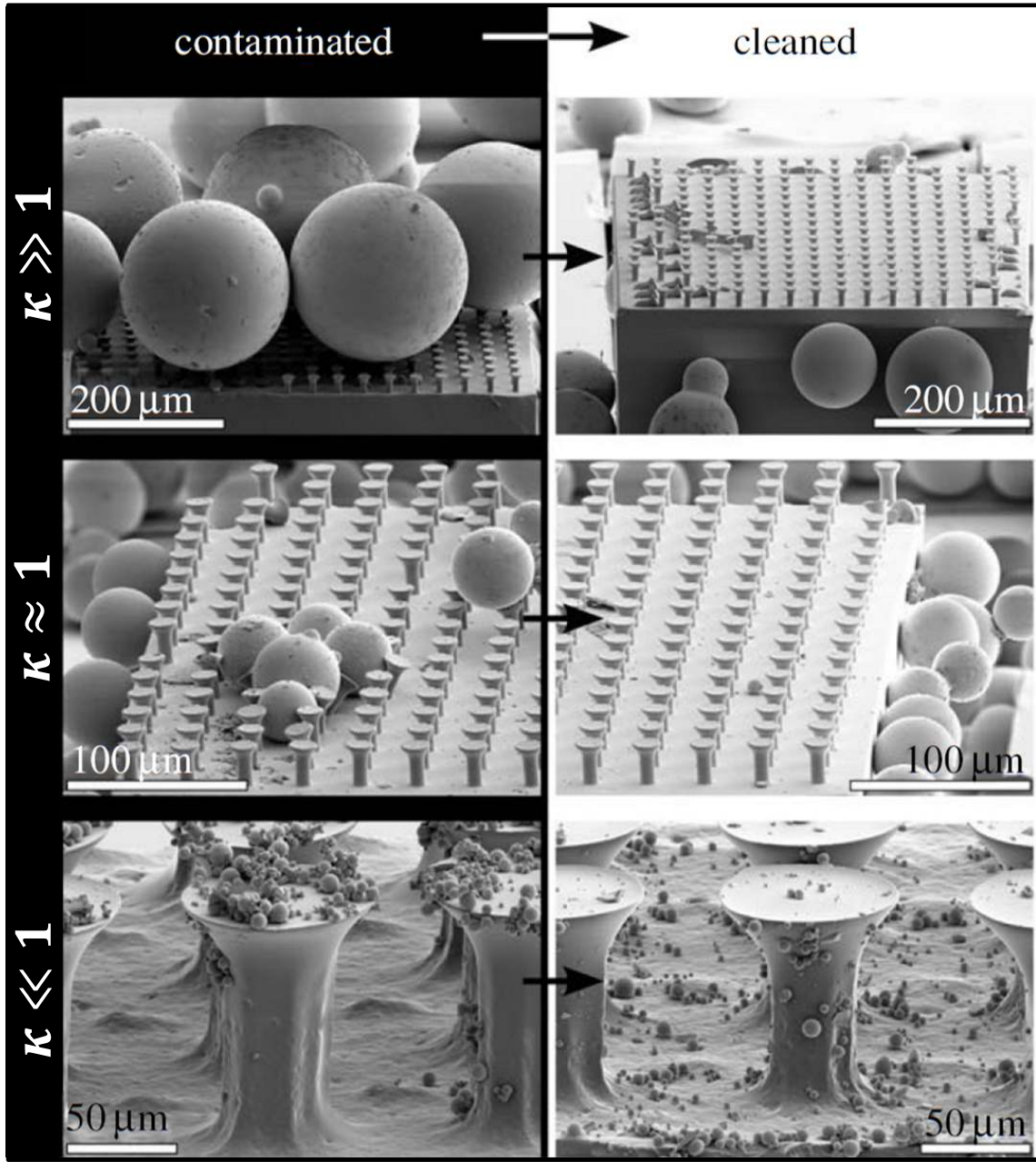


Figure 4.2: SEM images of samples in the small, intermediate and large contaminant regimes before and after contact self-cleaning shows significant cleaning in all regimes. In the large contaminant regime, the sample is completely cleaned but severely damaged, limiting the adhesion recovery to only 80%. Some microfiber damage is also observed in the intermediate regime. For the small contaminant regime, the microfibers are still intact, but it is almost impossible to completely remove all the contaminants from the microfiber tips, which is the reason for the poor adhesion recovery compared to the large contaminant regime.

## Effect of Normal and Shear Loading

To investigate how the loading step affected particle cleaning, the number of particles removed from the samples during the normal loading and the dragging steps were counted in some experiments where the particles were larger than  $40\text{ }\mu\text{m}$ . Figure 4.3 shows micrographs of a large microfiber sample contaminated by particles of mean diameter of  $118.5\text{ }\mu\text{m}$  after contamination (a), after normal loading and unloading (b), and after shear loading (c). We observed that  $95\% \pm 13\%$  of the particles cleaned were removed during the dragging step and the remainder during the normal loading and unloading steps ( $N_{\text{samples}} = 15$ ).

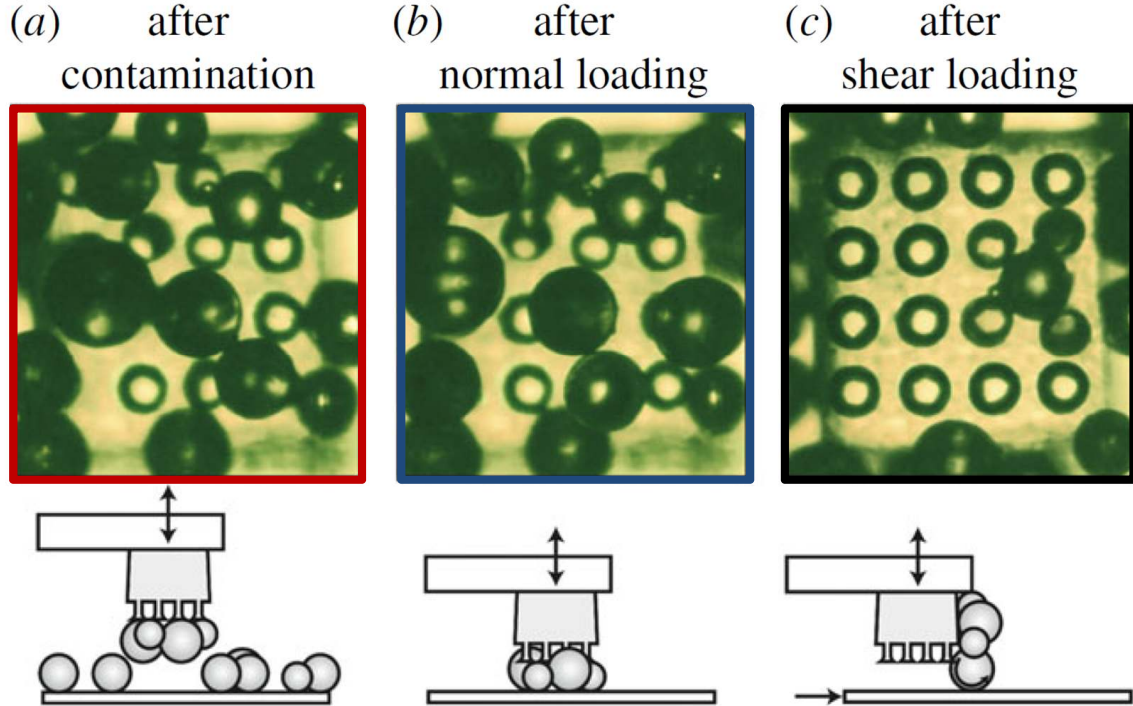


Figure 4.3: Micrographs showing a large microfiber sample contaminated by particles with mean diameter of  $118.5\text{ }\mu\text{m}$ ; (a) after contamination, (b) after normal loading and unloading and (c) after dragging. The result presented here as well as those of other samples investigated ( $N_{\text{samples}} = 15$ ) showed that  $95\% \pm 13\%$  of particles were cleaned during dragging, which indicates that dragging is a key process in contact self-cleaning.

The observation is in support of our self-cleaning model in Chapter 3. Our model for self-cleaning by substrate adhesion predicts that cleaning can only occur when the work of adhesion

at the contaminant-substrate interface  $w_{cs}$  is greater than 3/4 times that of the contaminant-fiber interface  $w_{cf}$ . In the case of this study, the ratio of  $w_{cs} = 56 \text{ mJ/m}^2$  to  $w_{cf} = 93 \text{ mJ/m}^2$  is 0.6, which is much less than the desired ratio of 0.75. Also, for the large contaminant regime, our model predicted cleaning at small preloads, but very high preload values were used in this experiment, much so that the microfibers were buckled during loading.

This result also indicates that particle rolling or sliding across the contact interface dominates the dry contact-cleaning process. However, shearing also poses a challenge to the lifetime of microfiber adhesives as observed in the post-cleaning SEM image and previously reported [43].

### **Anti-fouling**

Here, we study the ability of the microfiber adhesive to retain its adhesiveness immediately after contamination by analyzing the dirty adhesion  $P_{\text{dirty}}$  measured directly after the contamination and before the first cleaning cycle. As shown in Fig 4.1, samples in the large and intermediate contaminant regimes had very poor anti-fouling. These samples lost almost all of their initial adhesion upon contamination due to the size of the particles. The contaminating particles were large enough to prevent the microfibers in the array from making contact with the substrate even under high compressive loads. However, for the samples in the small contaminant regime, adhesion only dropped to an average of 22.4% immediately after contamination (Fig. 4.1), which is indicative of a good anti-fouling performance.

There are three possible explanations for the observed anti-fouling performance of the small particle regime:

1. the random distribution of contaminants across the sample,
2. the mechanics of mushroom shaped microfiber tip, and
3. the adhesion contribution of the small contaminants to the overall adhesive force of the array.

$a_f$ ( $\mu\text{m}$ )	$N_f$	$\sigma_0$ (MPa)	$P_{\text{clean}}$ (mN)	$P_{\text{dirty}}$ (mN) $\kappa = 10.7$ $D_s = 213.6 \mu\text{m}; N_s = 4$	$P_{\text{dirty}}$ (mN) $\kappa = 5.9$ $D_s = 118.5 \mu\text{m}; N_s = 16$	$P_{\text{dirty}}$ (mN) $\kappa = 0.1$ $D_s = 2.8 \mu\text{m}; N_s = 11\ 560$
10	289	0.29	26.33	$0.15 \pm 0.01$	$0.33 \pm 0.01$	$5.56 \pm 0.90$

Table 4.2: Simulation results of the clean  $P_{\text{clean}}$  and dirty  $P_{\text{dirty}}$  adhesion of a microfiber array contaminated with large microspheres ( $\kappa = 10.7$  and  $\kappa = 5.9$ ) and small microspheres ( $\kappa = 0.1$ ). Comparison of the calculated dirty adhesion due to the contributions of the small microsphere to the clean adhesion resulted in a 21.1% relative adhesion, whereas larger microspheres resulted in as low as 0.56% relative adhesion. Note that these results were for the maximum number of contaminants possible in the array. In practice, the number of contaminating particles could be less, resulting in a smaller adhesive force.  $D_s$  is the mean particle diameter,  $\sigma_0$  is the interfacial strength of the microfibers,  $N_s$  is the number of microspheres in contact with the substrate and  $\kappa = D_f/D_s$ .

In the first case, although the contamination was from a monolayer of particles, they were stochastically distributed across the array such that some microfibers can retain clean tips after the contamination process, leading to a higher relative adhesion. In the second case, even when a microfiber tip is contaminated, the mushroom-shaped tip can deform around the contaminating particle and make good contact during loading, as long as the contaminants are much smaller than the microfiber tip [22, 61, 107, 108, 128], which could also have led to the high anti-fouling performance. Lastly, the adhesive force of several contaminating particles making contact with the substrate can add up and contribute significantly to the overall adhesion of the sample. To further investigate the adhesion contribution of the contaminants and the particle size dependence, we will develop a model of adhesion for a contaminated adhesive for various particle sizes.

First, let us obtain the adhesive force of a clean microfiber adhesive  $P_{\text{clean}}$ . For an array where all microfibers have mushroom tips and are in contact with a flat substrate. Assuming that the substrate is atomically smooth and rigid, the adhesive force between the microfiber adhesive array and the substrate has been modeled in Section 2.3 as

$$P_{\text{clean}} = N_f \sigma_0 a_f^2, \quad (4.2)$$

where  $N_f = \rho A$  is the number of microfibers in the array,  $A$  is the apparent contact area (area of the adhesive),  $\rho$  is the density of the microfiber array,  $\sigma_0$  is the interfacial strength of the microfibers, and  $a_f$  is the radius of the microfiber tip.

For a fully contaminated array, the adhesive force  $F_p$  of a single rigid and spherical particle of radius  $R$  in contact with a rigid substrate is given as

$$F_p = 2\pi w_{ps} R, \quad (4.3)$$

where  $w_{ps}$  is the work of adhesion of the particle-substrate interface. The Derjagin-Muller-Toropov (DMT) model is used here due to the hard-to-hard contact interface between the particle and the substrate, where the Tabor parameter  $\mu_{\text{Tabor}}$  is less than 0.1. Consequently, the adhesive force  $P_{\text{dirty}}$  of a fully contaminated adhesive pad is given by

$$P_{\text{dirty}} = \pi N_p w_{ps} D_s. \quad (4.4)$$

Here,  $D_s$  is the average particle diameter and  $N_p$  is the number of contaminating particles in contact with the substrate.

Let us consider a  $0.5 \text{ mm} \times 0.5 \text{ mm}$  adhesive pad consisting of  $N_f = 289$  small microfibers ( $a_f = 10 \text{ }\mu\text{m}$ , microfiber stem radius  $a = 5 \text{ }\mu\text{m}$ , microfiber edge-to-edge spacing  $S = 20 \text{ }\mu\text{m}$ , and  $\sigma_0 = 0.294 \text{ MPa}$ ). The adhesive force of the array without contaminants can be obtained from Equation 4.2 as  $26.33 \text{ mN}$ . If the adhesive is contaminated by small silica microspheres ( $D_s = 2.8 \text{ }\mu\text{m}$ ,  $w_{ps} = 56 \text{ mJ/m}^2$ ), the adhesive force as obtained from equation 4.4 is  $5.56 \text{ mN}$ , which is  $21.1\%$  of  $P_{\text{clean}}$ . However, if the adhesive is contaminated by large microspheres ( $D_s = 118.5 \text{ }\mu\text{m}$ ), the adhesive force becomes  $0.33 \text{ mN}$ , which is  $1.25\%$  of  $P_{\text{clean}}$ . For even larger microspheres ( $D_s = 213.6 \text{ }\mu\text{m}$ ) the adhesive force is  $0.15 \text{ mN}$  and  $0.6\%$  of the  $P_{\text{clean}}$ . Surprisingly, these results match closely with that of the experiments (see Tab. 4.2), and show that for a fully contaminated sample, small contaminants can contribute significantly to the



adhesion of the sample compared to large contaminants.

### 4.2.3 Conclusions

In this section, we analyzed the results of contact self-cleaning experiments conducted on elastomer microfiber adhesives with mushroom tips using the load-drag-unload procedure. Despite the remarkable high adhesion of the microfibers examined, all samples exhibited a phenomenal self-cleaning characteristic. The adhesive samples and spherical silica contaminants grouped into the large, intermediate and small contaminant regimes showed similar trends.

Samples in the large contaminant regime recovered a higher percentage of their initially lost adhesion, and in fewer steps, compared to samples in the intermediate and small contaminant regime. The poor self-cleaning performance of the small contaminant regime can be attributed to the deformation of the microfiber tips around the small particles, such that the tips make contact with the substrate. As a result the microfiber tips do not move horizontally relative to the substrate (or only move by stick-slip) during dragging, so that particle sliding or rolling across the microfibers is inhibited. The poor self-cleaning performance of the small contaminant regime may also be due to the high normal load used in the experiments which could result in the buckling of the microfibers, so that they only make side contact with the substrate during dragging, and cleaning is inhibited.

Adhesion recovery in the large contaminant regime peaked at  $\sim 80\%$  even though the contaminating particles were completely removed from the adhesives as shown in the post-cleaning SEM images. We believe that the 20% unrecoverable adhesion is due to damage from the high normal load used in the experiment. This observation as well as the adverse effect of high normal load on the small contaminant regime aforementioned, leads us to believe that a low normal load is favorable for contact self-cleaning.

In the experiments, samples in the small contaminant regime retained an average of 22.4% of their adhesion after contamination, which is a good indication of anti-fouling. A model of

the adhesion contribution of microsphere contaminants to the overall adhesion of a microfiber sample confirmed that the small contaminants can contribute significantly to the samples' adhesion. The notable anti-fouling performance of the adhesives in the small contaminant regime can also be attributed to the shape of the microfibers tips, which were mushroom-shaped. Previous studies have shown that microfibers with mushroom-shaped tips show better contamination and flaw resistance compared to other tip shapes.

Analysis of the number of particles cleaned during the loading and unloading steps compared to those cleaned during the dragging step showed that 95% of the cleaning occurred during dragging the sample. The observation is consistent with our model of contact self-cleaning by substrate adhesion presented in Chapter 3. The poor contribution of substrate adhesion is due to the low surface energy of the glass substrate compared to that of the microfiber adhesive. The high preload used in the experiment leads to a higher adhesion for the large contaminant regime as shown in Fig 3.9 and could have inhibited cleaning by substrate adhesion.

The observation that self-cleaning occurred mainly during dragging implies that the mechanism of self-cleaning is either by particle rolling or sliding along the microfiber adhesive, or a combination of both mechanisms. Unfortunately, the results gathered from the current experiment does not give enough information to determine the underlying mechanism of contact self-cleaning using the load-drag-unload procedure. Hence, in the following section, we will conduct detailed self-cleaning experiments to uncover the underlying mechanism of contact self-cleaning through the load-drag-unload procedure.

## **4.3 Experiment II: The Mechanism of Contact Self-cleaning of Microfiber Adhesives Using the Load-Drag-Unload Procedure**

In the previous section, we demonstrated contact self-cleaning of synthetic gecko adhesives with mushroom tips using the load-drag-unload cleaning procedures similar to the loading procedure of the gecko toes during use, or the loading procedure of microfiber adhesives in some areas of application such as robotics. However, the underlying mechanism of contact self-cleaning using this procedure was not fully understood. This section presents a detailed experiment of contact self-cleaning that reveals the dominant mechanism of contact self-cleaning via the LDU cleaning procedure. We will also study the effect of dragging rate and normal load on the particle rolling friction. A basic model of spherical particle rolling on an elastomer fibrillar adhesive interface will be developed and compared to the experimental results. These results are expected to take us closer to determining design parameters for achieving self-cleaning microfiber adhesives.

### **4.3.1 Experimental Methodology**

The cleaning experiments were performed using a custom designed 2-axis force measurement system. As shown in Fig. 4.4, the system comprises of automated linear actuated stages (MFA-CC and VP-25XA, Newport) for motion control, manual rotational stages (GON40-U, Newport) for angular alignment correction, and two load cells (GSO-50 and GSO-10, Transducer Techniques) for normal and shear force measurements. The experimental setup was mounted onto an inverted optical microscope (ECLIPSE TE200, Nikon), and a colored digital video camera (DFW-X710, Sony) was used to capture the visual data and observe the contact area during the experiments. Custom software was used to control the system and to record a time-stamped visual and force data. A monochromatic light source (DC-950, Fiber-Lite) was channeled through

the microscope onto the contact interface for better view of the contact area.

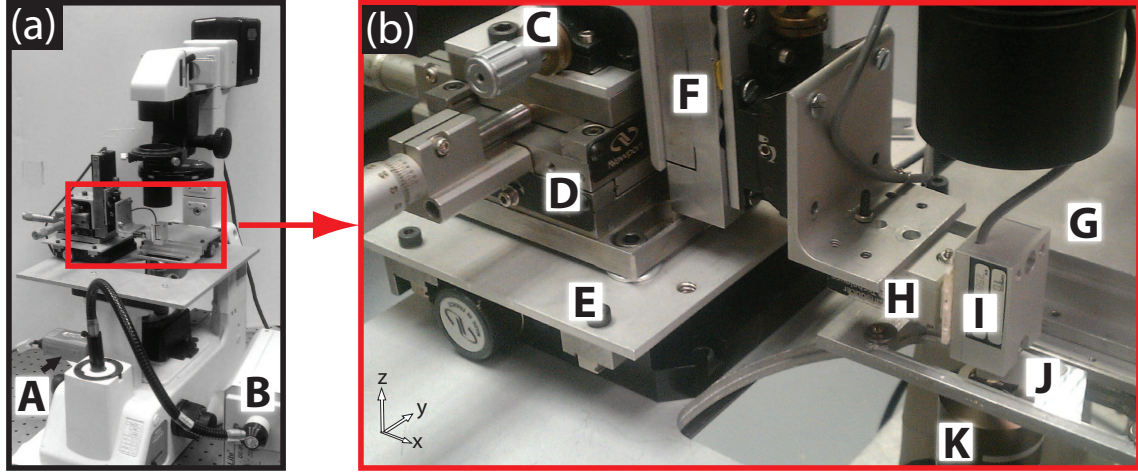


Figure 4.4: Images of the 2-axis force measurement system used in the self-cleaning experiments showing: (a) the inverted microscope upon which the setup was mounted and; (b) the custom-built experimental setup. In the figures, A=camera, B=light source, C=goniometer, D>manual 2-axis linear stage, E=motorized y-axis linear stage, F=motorized z-axis linear stage, G=motorized x-axis linear stage, H=vertical axis load cell, I=horizontal axis load cell, J=glass substrate, and K=microscope objective. The contaminated sample (not shown) is mounted onto the horizontal axis load cell and brought into contact with the glass substrate during the experiment.

Experiments were conducted using elastomer microfiber adhesive samples with mushroom-shaped tips [2, 27, 49, 95]. The samples were made from polyurethane elastomer (ST-1060, BJB Enterprises, Youngs modulus  $E_f = 2.9$  MPa, Poissons ratio  $\nu_f = 0.5$ ), and fabricated using a previously published lithography and soft molding technique [2]. The microfibers were laid out in a square-packing pattern, with a center-to-center spacing of  $118 \mu\text{m}$ , microfibers tip diameter  $a_f$  of  $95 \mu\text{m}$ , and an aspect ratio (fiber tip diameter to microfiber height ratio) of 1.

The samples were contaminated with a single fused silica micro-particle (FSB Swiss Jewel Company). A single  $250 \mu\text{m}$  diameter particle was used in the experiment to study the cleaning mechanism for cases where the particles are larger than the microfiber tips (large contaminant regime) and for cases where the particles are smaller than the microfiber tips (small contaminant regime). In the latter case, a flat polyurethane elastomer sample was used. Using  $250 \mu\text{m}$  diameter particles allowed for observation of the particle motion type (rolling or sliding), in the

video images. However, to study the effects of normal load and drag speed, we used large 1 mm diameter particles due to the resolution limit of our load cells, in order to measure the rolling friction values for a single particle as well as to obtain a clear view of the contact area. Our use of spherical microparticles as contaminants makes the current work consistent with, and applicable to previous studies. [44, 52, 58, 62, 88, 89, 95, 121, 134]

## 4.3.2 Results and Discussions

### Evidence of Particle Rolling

Let us define the normalized particle displacement,  $\eta$ , as

$$\eta = 2\delta x / \Delta_x, \quad (4.5)$$

where  $\delta x$  is the particle displacement, and  $\Delta_x$  is the applied drag distance. Evidently,  $\eta$  is also a measure of the cleaning performance. Large values of  $\eta$  indicate large particle displacement relative to the adhesive after a single cleaning step, which results in better cleaning performance. For a spherical particle sandwiched between a glass substrate and a fibrillar adhesive sample, as shown in Fig. 4.5, three cases of particle motion are possible when the glass substrate is dragged:

**Case I:** The particle can slide across the substrate without moving relative to the microfiber tips  $\Rightarrow \eta = 0$  (Fig. 4.5(b));

**Case II:** The particle can slide across the microfiber tips without moving relative to the substrate  $\Rightarrow \eta = 2$  (Fig. 4.5(c));

**Case III:** The particle can roll with respect to both surfaces  $\Rightarrow \eta = 1$  (Fig. 2 4.5(d)).

A combination of any two or all three cases is also possible when the critical forces required for each of the particle motion are similar. For example, the particle can roll with intermittent slipping across the fibrillar adhesive when the critical shear force for particle rolling  $f_{\text{rolling}}$  is

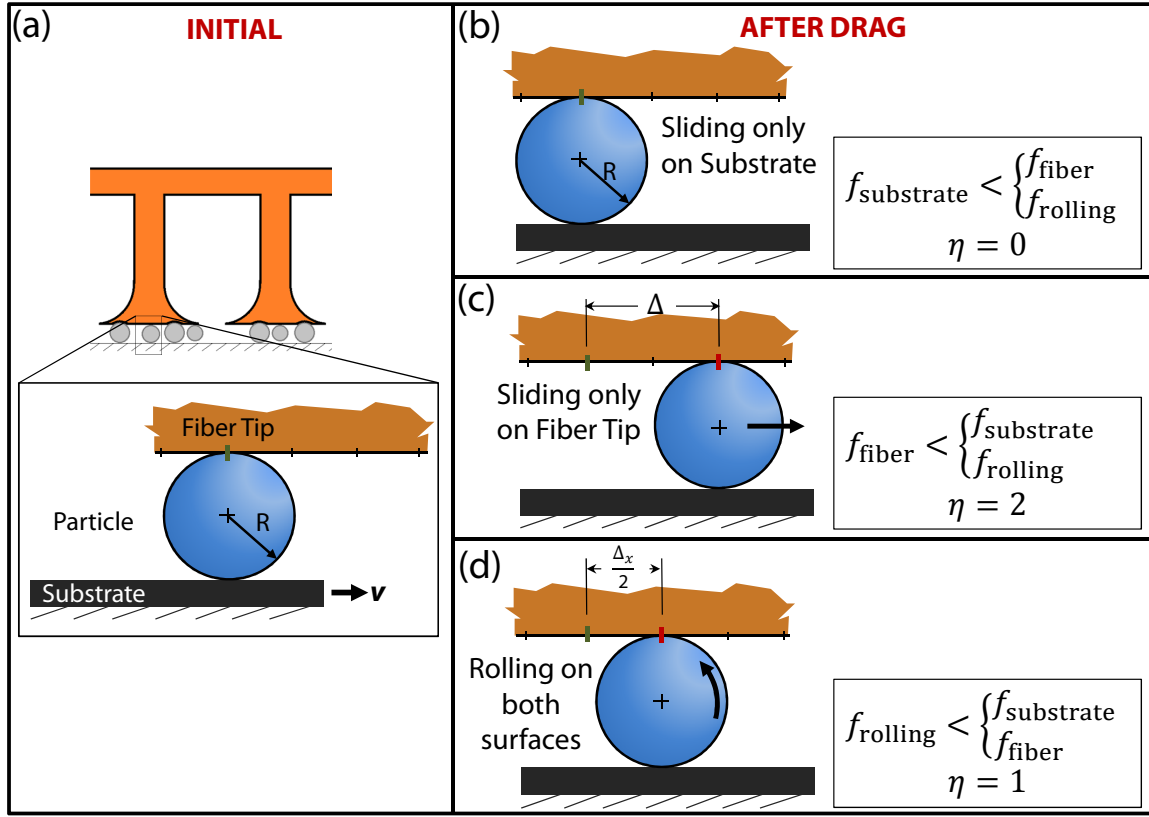


Figure 4.5: Schematics of a single contaminating particle sandwiched between a polyurethane microfiber tip and a hard glass substrate, before and after the substrate is dragged. **(a)** Initial position of the particle before dragging (note the markers on the microfiber tip: each marker spacing =  $\Delta_x/2$ , green markers indicate starting position and red markers indicate the final position of the particle after the dragging step). After dragging: **(b)** the particle remains in the same position relative to the microfiber when sliding occurs only at the substrate interface, **(c)** the particle is displaced a distance equal to the drag distance, when sliding occurs only across the microfiber tip, or **(d)** the particle is displaced a distance equal to one-half the applied drag distance under pure rolling condition. Here,  $R$  is the particle radius,  $f_{\text{fiber}}$  is the critical shear force for particle sliding across the microfiber,  $f_{\text{substrate}}$  is the critical shear force for particle sliding across the substrate,  $f_{\text{rolling}}$  is the critical shear force required to overcome the rolling resistance.  $\eta$  is the normalized particle displacement given in equation 4.5,  $V$  is the drag speed and  $\Delta_x$  is the applied drag distance.

close to the critical shear force for particle sliding across the microfiber  $f_{\text{fiber}}$ , in which case  $\eta$  will be slightly greater than 1.

In logical terms, any one of the cases of particle motion (Fig. 4.5(b-d)) is a sufficient condition for obtaining  $\eta$ . However the value of  $\eta$ , in and of itself, is not sufficient to know the particle motion. For example, under pure rolling motion,  $\eta$  is equal to 1; but,  $\eta = 1$  does not necessarily imply that the particle motion is pure rolling, as it could be the result of a combination of several particle motions. Thus, a visual inspection is necessary to ascertain the particle motion.

Figure 4.6 shows graphs of the normalized particle displacements measured at various normal loads for a 250  $\mu\text{m}$  diameter contaminant particle sandwiched between a microfiber array and dragged horizontally at a speed of 20  $\mu\text{m/s}$ . From the graph, it is observed that  $\eta$  is approximately equal to 1 for all loads, which suggests that rolling dominates the cleaning process. Analysis of the videos recorded during the experiments confirmed that particle rolling is the dominant cleaning mechanism (videos can be found in the supplementary materials available in the electronic version of this thesis). At very small normal loads less than 10 mN,  $\eta$  is slightly greater than 1 as can be seen in Fig. 4.6(a). This suggests that there was some sliding at the microfiber interface although rolling occurred for most of the time. At large normal loads greater than 50 mN,  $\eta$  becomes less than 1 and decreases with increasing normal load as shown in Fig. 4.6(b). This indicates the occurrence of sliding at the substrate interface. At very high loads, the particle becomes significantly indented in the microfiber array which begins to act as obstacles, so that sliding at the substrate (Case I) becomes the dominant particle motion, and cleaning is inhibited.

Also, the observed dependence of  $\eta$  on the normal load is intuitive since friction in this case is a function of both the applied normal load and contact area as described in Chapter 3. By increasing the normal load, the contact area at the adhesive interface is increased significantly (for the soft polyurethane) compared to the contact area at the substrate interface (for hard

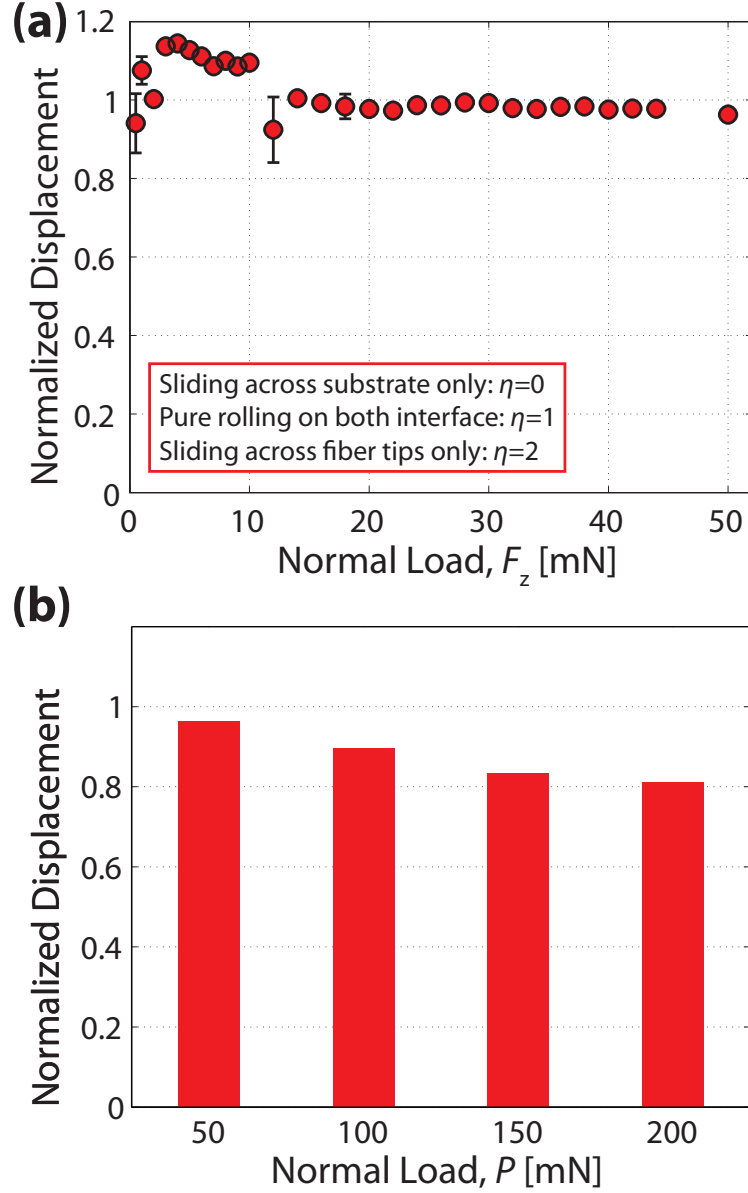


Figure 4.6: Graphs of the normalized particle displacements measured at various normal loads for a  $250\text{ }\mu\text{m}$  diameter contaminant particle sandwiched between a microfiber array and dragged horizontally at a speed of  $20\text{ }\mu\text{m/s}$ . **(a)** The normalized particle displacement is approximately equal to 1 at all loads less than 50 mN, which suggests that particle rolling dominates the cleaning process. Analysis of the videos recorded during the experiments confirmed that particle rolling is the dominant cleaning mechanism (videos can be found in the supplementary materials available in the electronic version of this thesis). **(b)** Graph of the normalized particle displacement for normal loads up to 200 mN shows a decreasing normalized displacement as the normal load is increased. The decreasing performance is due to an increasing occurrence of particle sliding across the substrate.  $\eta$  is the normalized particle displacement given by equation 4.5.



glass). This can lead to a significantly higher friction resistance at the adhesive interface so that sliding occurs only along the substrate. These results lead us to conclude that a low normal load is favorable for the load-drag-unload self-cleaning procedure. In the following section, we study the effect of cleaning rate and normal load on the rolling friction during contact self-cleaning.

### **Effect of Dragging Rate and Normal Load on Particle Rolling Friction**

We studied the effect of drag rate and normal load on particle rolling friction by measuring the rolling friction during the LDU process. During the experiment, it was important that the microfibers were not in direct contact with the substrate so that the measured shear force was solely due to the friction at the particle-fiber and particle-substrate interfaces. As a result, a 1 mm diameter particle was used. A sample plot of the normal (black line AKLMG) and tangential (red line ABCDEFG) forces measured during a single experiment is shown in Fig. 4.7. In the graph, line AB is the crosstalk on the tangential force sensor during normal loading. The average tangential force measured at the end of the loading step (line BC) is subtracted from the tangential force measured during the dragging step (line C-F) to obtain the actual rolling friction without the crosstalk. Analysis of the rolling friction curve reveals two distinct regions. The first is observed at the onset of rolling (line C-E) during which the rolling friction increases gradually until it saturates. In the second region (line E-F), the rolling friction remains constant for the rest of the dragging step. The increase in rolling friction in the first region is believed to be the result of an increasing contact area at the onset of rolling (see contact area insets in Fig. 4.7).

Rolling friction curves for various drag speeds ranging from 10 to 500  $\mu\text{m/s}$ , under a constant normal load of 100 mN, are shown in Fig. 4.8(a). At low drag speeds, the rolling friction increased gradually until it reached a steady-state value. However, for higher drag speeds, the rolling friction increased past the steady-state value to an initial peak value before decreasing to a steady-state rolling friction. The peak of this overshoot was also observed to increase as

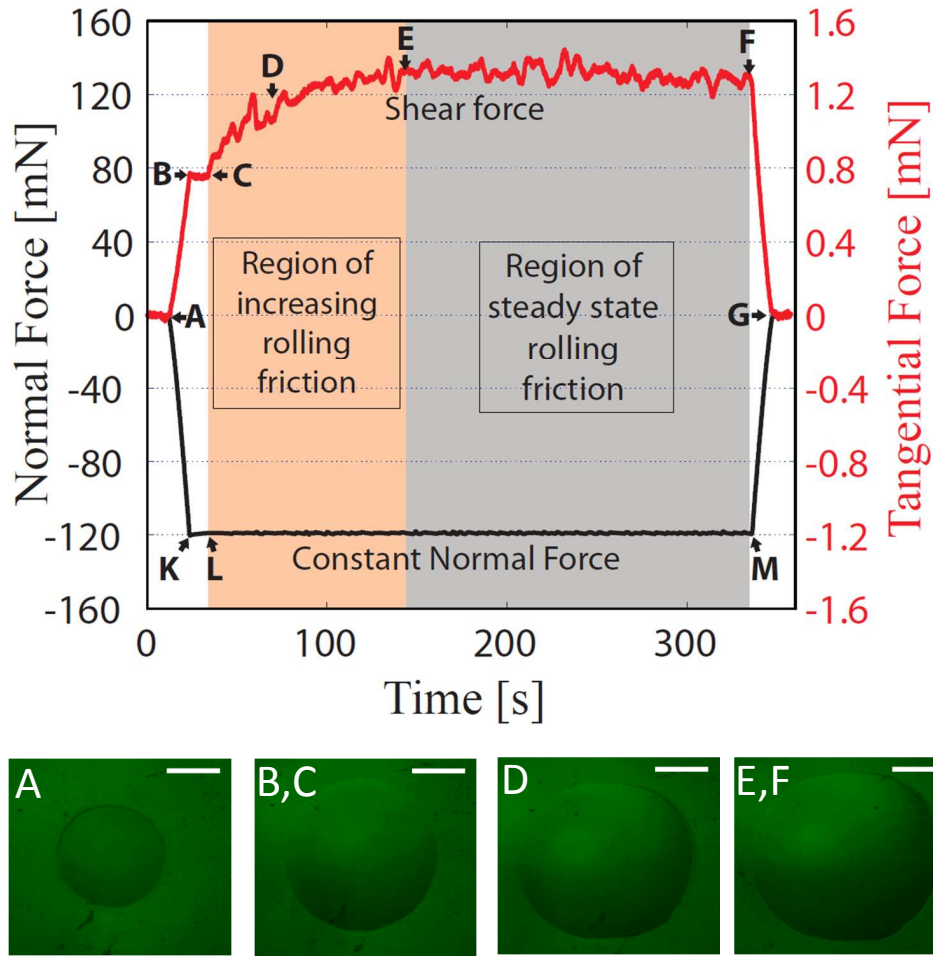


Figure 4.7: Graph of the normal and tangential forces measured during a single contact self-cleaning experiment with a 1 mm diameter silica micro-particle rolling across a flat polyurethane adhesive sample, for a normal load of 120 mN and a drag speed of  $10 \mu\text{m/s}$ . Line AKLMG (black line) is the measured normal force, while line ABCDEFG (red line) is the measured tangential force. During the experiment, the contaminated sample was pressed against a smooth and flat glass slide until preload of 120 mN was reached (line AK). A contact time of 10 s was observed before the substrate was dragged horizontally while keeping the preload constant (line LM). After a drag distance of 3 mm, the sample was pulled away from the glass substrate (line MG). The crosstalk on the measured tangential force due to the normal load was obtained as the average of line BC and subtracted from the rest of the tangential force measurement to obtain the actual rolling friction. The increasing rolling friction observed at the initial phase of rolling is attributed to the growth of the contact area (insets) at the onset of rolling.

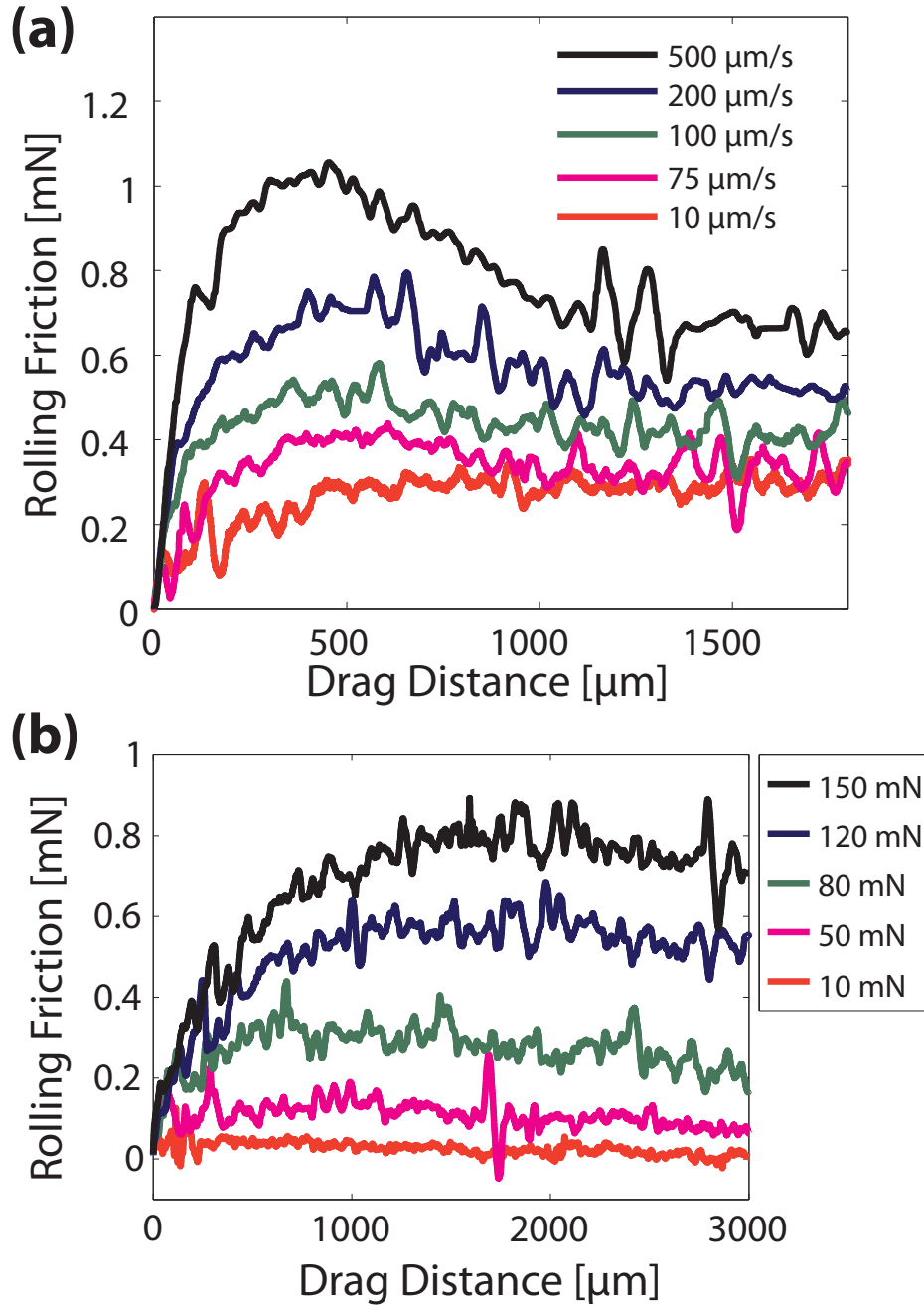


Figure 4.8: Graphs showing the dependence of rolling friction on the drag speed and normal load for a 1 mm diameter particle. **(a)** Rolling friction plotted against drag distance for various drag speeds at a constant normal load of 100 mN shows an increasing steady state rolling friction as the drag speed was increased. An initial peak rolling friction with overshoots of up to 160% of the steady state value was observed for drag speeds greater than 50  $\mu\text{m/s}$ . **(b)** Graph of rolling friction plotted against drag distance for various normal loads and at a constant drag speed 10  $\mu\text{m/s}$  shows an increasing steady state rolling friction as the normal load is increased.

the drag speed was increased, and rose up to 160% of the steady state rolling friction for a drag speed of 500  $\mu\text{m/s}$ . Finally, we observed that the average steady-state rolling friction increased as the drag speed was increased. We believe that the increase in the steady-state rolling friction was due to an increase in the work of adhesion, which is known to increase with the crack propagation speed as presented in Chapter 2 and will be further discussed later in this section. We believe that the observed overshoot is as a result of the enhanced adhesion at the initial contact area before the onset of rolling (a relaxation phenomenon), in addition to the rate effect on work of adhesion mentioned above.

Rolling friction curves from cleaning experiments conducted at various normal loads (10 to 150 mN), but for a constant drag speed of 10  $\mu\text{m/s}$  are shown in Fig. 4.8(b). The curves had similar trend for different normal loads, but reached a higher steady-state rolling friction as the normal load was increased. The observed increase in the rolling friction with normal load is believed to be as a result of the increased contact area at higher normal loads.

Using the mechanics of contact self-cleaning by particle rolling presented in Chapter 3, and the model for the rate dependence of adhesion presented in Chapter 2, we will model the observed load and rate effect on particle rolling friction as follows.

The critical force for self-cleaning by particle rolling mechanism as derived in Section 3.3 is

$$f_{\text{rolling}} = 3\pi (\xi_{\text{cf}}w_{\text{cf}} + \xi_{\text{cs}}w_{\text{cs}}) \quad (4.6)$$

where  $\xi$  is the critical rolling displacement before a re-adjustment of the contact zone (irreversible change in position of the particle) and a function of the contact radius, and  $W$  is the work of adhesion of the contaminant-microfiber and contaminant-substrate interfaces denoted by the subscripts “cf” and “cs”, respectively. By assuming a conservative value of  $\xi$  equal to the contact radius, and calculating the work of adhesion and contact radii at both interfaces for the case of the materials used in this study, we observed that  $w_{\text{pf}}\xi_{\text{pf}}$  for the soft polyurethane interface was over an order of magnitude greater than  $w_{\text{ps}}\xi_{\text{ps}}$  for a rigid glass interface. Thus, for

simplicity, we can neglect the contribution of the substrate from equation 4.6 so that the critical rolling friction force can be obtained as

$$f_{\text{rolling}} = 3\pi w_{\text{pf}} \xi_{\text{pf}}. \quad (4.7)$$

Although equation 4.7 does not show a direct dependence on the drag speed, the work of adhesion has been previously shown in Section 2.4 to be dependent on crack propagation speed through a power law relationship of the form

$$w_{\text{pf}} = G_0 [1 + (v/v_0)^n]. \quad (4.8)$$

Here,  $v$  is the crack propagation speed which is equal to the particle displacement speed (one-half of the drag speed for pure rolling motion),  $G_0$  is the work of adhesion as  $v$  approaches zero,  $v_0$  is the crack propagation speed at which  $G_0$  is doubled, and  $n$  is a fitting parameter.

Also, since  $\xi$  is a function of the contact radius, it is expected to be dependent on normal load. We propose that  $\xi_{\text{pf}}$  as a function of the normal load  $P$  in the form

$$\xi_{\text{pf}} = \xi_0 + CP, \quad (4.9)$$

such that  $\xi_{\text{pf}} = \xi_0$  when  $P$  is zero [35, 55], but increases linearly with  $P$  by a compliance parameter  $C$  (m/N) [65]. We anticipate that  $\xi_0$  is a function of the particle size and will increase for larger particles [19, 55];  $C$ , on the other hand will depend on the effective modulus of the contact interface and the contact radius.

By substituting equations 4.8 and 4.9 into equation 4.7, we obtain the equation for the rolling friction force as a function of both the normal load and drag speed as

$$f_{\text{rolling}} = 3\pi G_0 (\xi_0 + CP) [1 + (v/v_0)^n], \quad (4.10)$$

where  $\xi_0$  and  $G_0$  are geometric and material dependent properties, while  $n$  and  $C$  are fitting parameters for the rate and load dependence, respectively. A graph of the average steady-state rolling friction plotted against  $P$  for a  $5 \mu\text{m/s}$  rolling speed is shown in Fig. 4.9(a). The graph shows a linear relationship between rolling friction and normal load.

The experimental data was fitted to equation 4.10 to obtain  $C = 1.85 \pm 0.13 \mu\text{m/mN}$ , and  $n = 0.63$ , where  $\xi_0 = 0.4 \mu\text{m}$ ,  $G_0 = 140 \text{ mJ/m}^2$  and  $v_0 = 104.4 \mu\text{m/s}$  for the polyurethane-fused silica interface. Due to the relatively high normal load values investigated,  $\xi_0$  given here is statistically insignificant, and experiments at very small normal load with a high resolution force sensor will be required to obtain a more accurate value [19, 55].

Experimental results of the average steady state rolling friction measured at various drag speeds are shown in Fig. 4.9(b) for normal loads of 20, 50, and 100 mN. For each normal load, the theoretical rolling friction obtained from equation 4.10 using the parameter values listed above is also plotted and fits well with the experimental data. It is important to note that although the theoretical plots were obtained using fitted parameters  $n$  and  $C$ , those parameters were obtained from a single loading case (100 mN) but they agree well with experimental results at differing loads and drag speeds values.

### 4.3.3 Conclusions

By studying the mechanics of cleaning using a single contaminating particle, we have shown that particle rolling is the dominant mechanism for contact self-cleaning of mushroom-shaped microfiber adhesives using the load-drag-unload procedure. Analysis of the particle displacement suggested that particle rolling is the dominant motion. A review of the videos recorded during the experiments confirmed that particle rolling is indeed the dominant cleaning mechanism for the small and large contaminant regime (A video of this experiment is included as a supplementary material in the electronic version of this thesis).

The experimental results also showed that particle motion at low load is dominated by

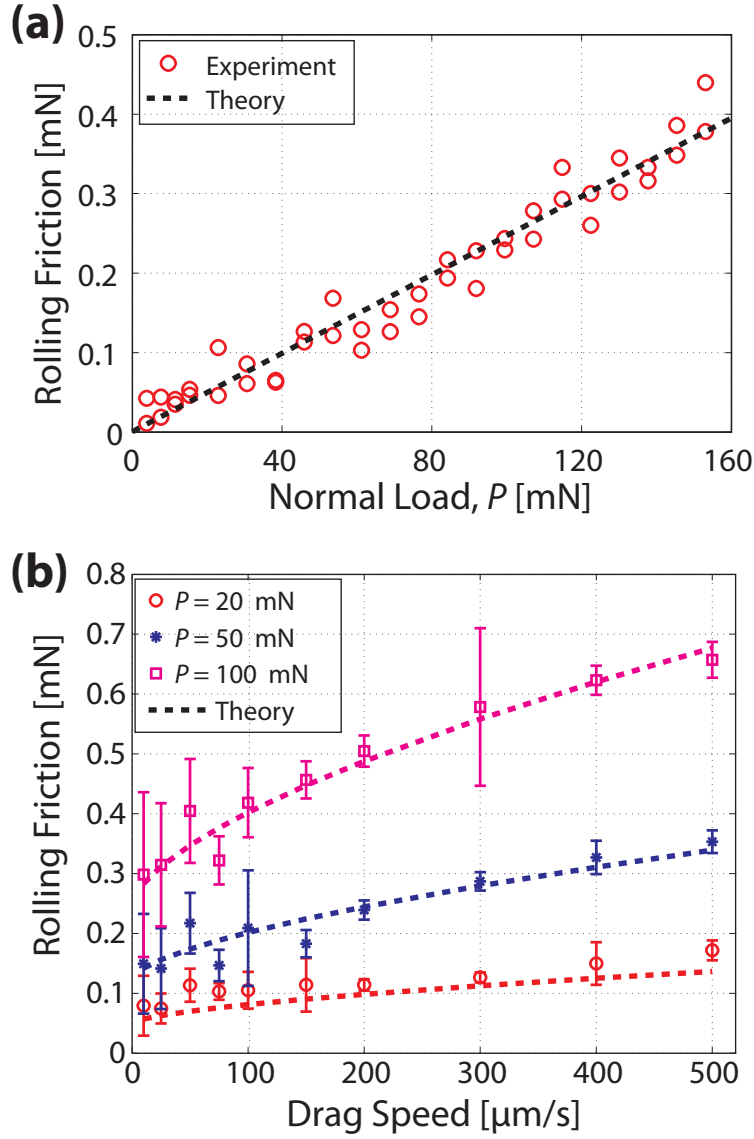


Figure 4.9: Experimental and theoretical results from equation 4.10 of the dependence of rolling friction on both normal load and drag speed. **(a)** Graph of rolling friction as a function of normal load for a  $5 \mu\text{m/s}$  rolling speed. Each data point represents the average steady-state rolling friction for a single experiment. The dashed line is a fitted line from which are obtained after fitting to equation 4.9. **(b)** Experimental results of the average steady-state rolling friction measured at various drag speeds and for normal loads of 20, 50, and 100 mN. The theoretical results (dashed lines) are obtained from equation 4.10 and agrees well with the experimental results at various loads and drag speed values where  $n = 0.63$ , and  $C = 1.9 \mu\text{m/mN}$  are obtained from fitting to equation 4.10,  $G_0 = 140 \text{ mJ/m}^2$ ,  $v_0 = 104.4 \mu\text{m/s}$ , and  $\xi_0 = 0.38 \mu\text{m}$ .

rolling with some slipping. This result is in agreement with our model prediction as shown in the cleaning map presented in Fig. 3.7 for shear loading. However, at high loads, the cleaning performance dropped below  $\eta = 1$  as sliding at the substrate interface occurred intermittently with particle rolling. Cleaning was optimally inhibited at high loads as sliding along the substrate became prominent.

The experimental result and supporting theoretical model shows that rolling friction is strongly dependent on the applied normal load and the drag rate. Increasing the applied normal load or the drag rate both lead to an increase in the rolling resistance, resulting in a reduction in the cleaning performance. Based on this analysis, we suggest that low normal loads and low drag rates are more favorable for contact cleaning of spherical contaminants.

## **4.4 Simulation of Contact Self-cleaning for Microfiber Adhesives**

### **4.4.1 Introduction**

In this section, we will utilize our current understanding of the mechanics and mechanisms of contact self-cleaning to design a routine for the numerical simulation of contact self-cleaning via the load-drag-unload procedure. A 2-dimensional simulation procedure is presented for a single row of microfibers with mushroom-shaped tips of Young's modulus  $E_f$ , tip radius  $a$ , microfiber length  $L$ , tip edge-to-edge spacing  $g$ , and microfiber edge-to-edge spacing  $S$  (see Fig. 4.10). The contaminants are assumed to be hard spheres and the substrate is assumed to be rigid, flat and atomically smooth.



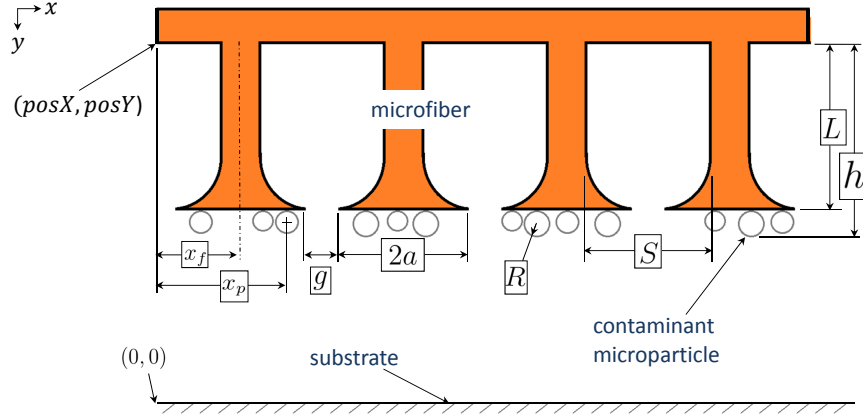


Figure 4.10: An illustrative diagram with dimensions showing the side view of a contaminated microfiber array used in the simulation of contact self-cleaning via the load-drag-unload procedure.

#### 4.4.2 Simulation Methodology

The load-drag-unload cleaning procedure will be used in the simulation using a constant normal load  $P$ . Based on the preceding experimental result and model predictions for the contact self-cleaning, we will assume that the particles are cleaned by particle rolling only, but the simulation can be easily modified to account for self-cleaning by substrate adhesion and particle sliding on the adhesive. We will begin by listing and initializing all the simulation parameters.

##### Microfiber array parameters:

- $posX, posY$  is the  $x$ - and  $y$ -coordinates of the top-left edge of the microfiber backing layer relative to the origin
- The microfibers are labeled  $j$  from 1 to  $N_f$ , such that  $j = 1$  is the first microfiber and  $j = N_f$  is the last microfiber, counting from left to right
- $x_f(j)$  is the horizontal location of center axis of microfiber  $j$  with respect to  $posX$
- $R^*(j)$  is the radius of the largest particle in contact with microfiber  $j$  at an given instance
- $h(j)$  is the virtual height of microfiber  $j$  and given as  $h(j) = L + 2R^*(j)$
- $H$  is the maximum virtual height in the array

- $f_{\text{STATE}}(j)$  is the state of microfiber  $j$  which can be used to determine whether the microfiber is contaminated or not

$$f_{\text{STATE}}(j) = \begin{cases} 1 & \text{if } h(j) > L \\ 2 & \text{if } h(j) = L \end{cases} \quad (4.11)$$

- $\Delta_x$  is the applied drag distance for each cleaning cycle

### Particle parameters:

First, a set of 100 particle radii is randomly generated using the desired mean and standard deviation of the particles

- The particles are labeled  $i$  from 1 to  $N_p$ , where  $N_p$  is the total number of particles in the array
- $R(i)$  is the radius of particle  $i$  which is obtained by randomly selecting a number from the generated particle radii
- $x_p(i)$  is the horizontal position of particle  $i$  with respect to  $posX$ . The initial value is randomly generated to be between the left edge of the first microfiber's tip and the right edge of the last microfiber's tip. If a newly generated particle intersects with a previously generated particle, the new data is recycled and another data is generated. Particles and their location are generated until the pad is filled
- $p_{\text{state}}$  is the state of the particle that tells whether it can be displaced, or it has been cleaned, where

$$p_{\text{state}}(i) = \begin{cases} 0 & \text{alive, but not in contact with substrate} \\ 1 & \text{alive, and in contact with substrate} \\ 2 & \text{cleaned, i.e. dead} \end{cases} \quad (4.12)$$

Similar to the experiments, we will separate the simulation steps for one cleaning cycle into three levels as shown in Fig. 4.11. In **Level I**, the adhesive force of the contaminated microfiber

array is obtained. In **Level II**, the sample is brought into contact with the substrate and indented until the desired preload is reached. Particles that are alive and make contact with the substrate after the indentation are considered “cleanable” and their  $p_{\text{state}}$  are change from 0 to 1. In **Level III**, the sample is displaced by small increments  $dx$  in the positive Y-axis until the specified drag distance  $\Delta_x$  reached. For each incremental step, the particles with  $p_{\text{state}} = 1$  are displaced a distance  $\delta x$  in the reverse direction with respect to the sample. However, if any of the particles are cleaned after an incremental displacement, the value of  $p_{\text{state}}$  for such particles are changed to 2, and the simulation returns to level II where the indentation distance and related parameters are readjusted. The simulation continues to loop through Levels II and III (as necessary) until  $\Delta_x$  is reached which indicates the completion of a single cleaning cycle, and another cycle begins. The cleaning simulation ends after completing LEVEL I if all the particles have been cleaned or the desired number of cleaning cycles is reached. Details of each of the simulation levels can be found in Appendix A.2.

#### 4.4.3 Results and Discussions

The contact self-cleaning simulation was implemented in C++ for a microfiber array ( $a = 47.5 \mu\text{m}$ ,  $L = 105 \mu\text{m}$ ,  $S = 75 \mu\text{m}$ ,  $E_f = 2.9 \text{ MPa}$ ) contaminated by particles of various sizes: small ( $D_s = 30 \pm 5 \mu\text{m}$ ) and large ( $D_s = 118 \pm 18 \mu\text{m}$ ). Using the mean and standard deviation specified for each particle size, a set of 100 random particle radii were generated using a random number generator routine in Excel. Particle sizes used in the simulation were randomly selected from the 100 particle radii from the C++ program. A tolerance of 0.005 was used in the simulation for step 7 in Level I. The simulation result is shown in Figure 4.12(a). Each error bar represents the mean and standard deviation of 20 simulations. The graph shows a dependence of adhesion recovery on particle sizes for each cleaning cycle. Large particles are observed to clean easily and faster compared to smaller particles. A summary of the experimental results obtained in Experiment I is given in Fig 4.12(b). A comparison of the results for

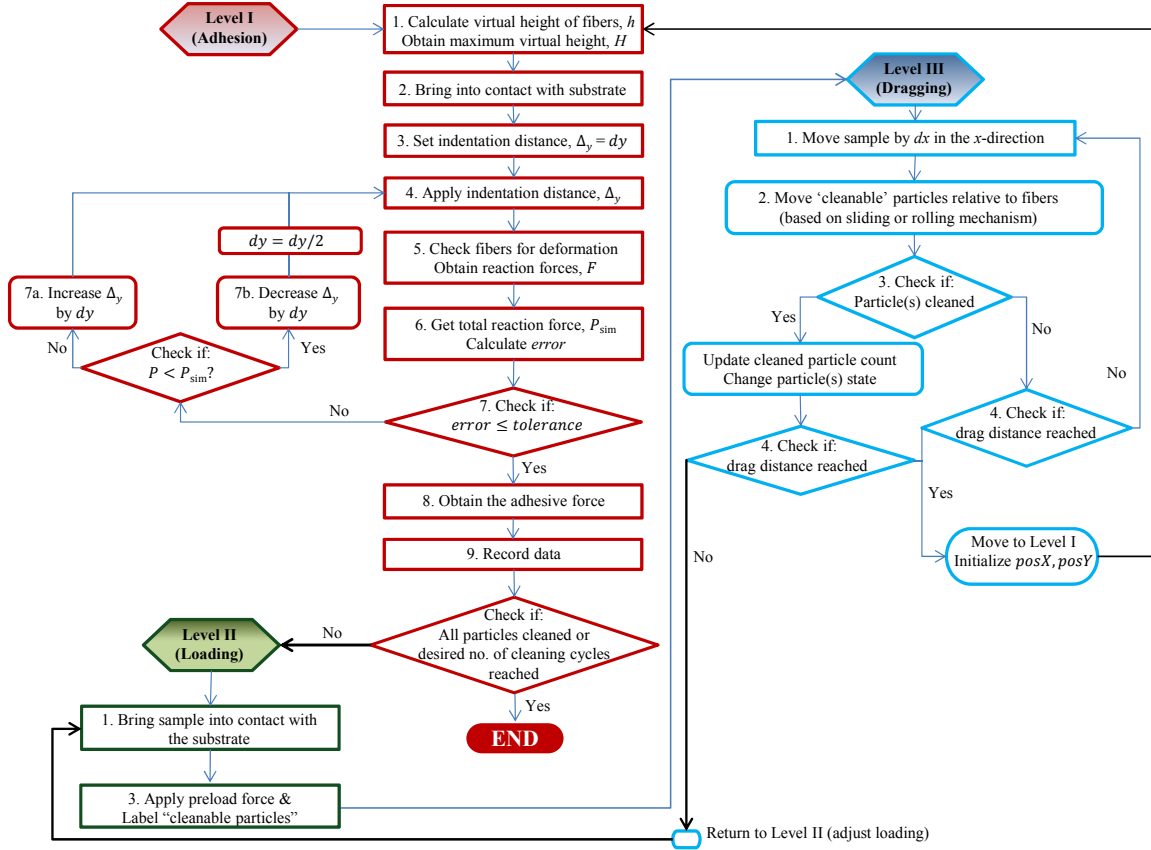


Figure 4.11: A numerical simulation flow chart for contact self-cleaning of microfiber adhesives using the load-drag-unload procedure. Similar to the load-drag-unload contact self-cleaning experiments, each cleaning cycle is separated into three (3) levels. In Level I, the adhesive force of the contaminated microfiber adhesive is obtained. In Level II, the adhesive is pressed against the substrate until the desired preload is reached. In Level III, the sample is dragged against the substrate by small increments until the specified drag distance is reached. If a particle is cleaned after any drag step and the drag distance has not been reached, the simulation returns to Level II, where the indentation distance and the number of contacting microfibers are readjusted.

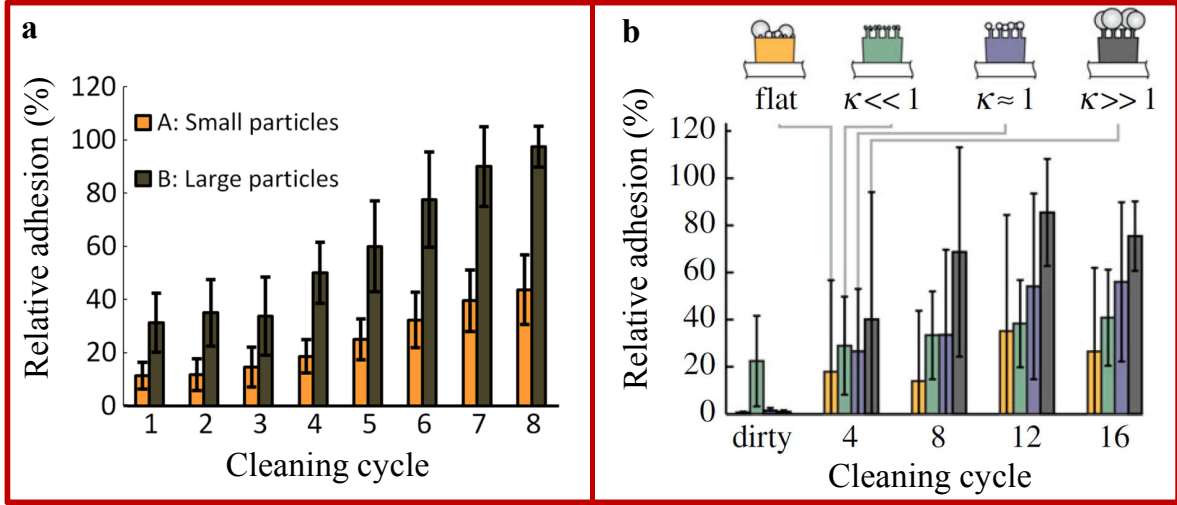


Figure 4.12: **(a)** Results of numerical simulation of contact self-cleaning of a microfiber adhesive array ( $a = 47.5 \mu\text{m}$ ,  $L = 105 \mu\text{m}$ ,  $S = 75 \mu\text{m}$ ,  $E_f = 2.9 \text{ MPa}$ ) contaminated with small ( $D_s = 30 \pm 5 \mu\text{m}$ ) and large ( $D_s = 118 \pm 18 \mu\text{m}$ ) microspheres using the load-drag-unload procedure. Error bars represents the mean and standard deviation of 20 simulations. **(b)** Experimental results of adhesion recovery for load-drag-unload based contact self-cleaning of microfiber adhesives with mushroom-shaped tips. Both results show similar trend for the dependence of adhesion recovery on contaminant size

the large ( $\kappa \gg 1$ ) and small ( $\kappa \ll 1$ ) particles in both cases, shows similar trends of adhesion recovery. Note that the adhesive force measured immediately after contamination shown in the experimental result is not shown in the simulation result. A comparable result for this case has been given in Tab. 4.2

## 4.5 Summary

In this chapter, we presented experiments and simulations that have significantly expanded on the current knowledge of contact self-cleaning using the load-drag-unload procedure. We started by investigating a first set of contact self-cleaning experiment of gecko-inspired microfiber adhesives with mushroom-shaped tips (the experiment was designed and conducted by my colleague Y. Menguc and collaborator M. Rohrig. I developed the model and analyzed the results presented here). The following observations were made from our analysis of the

experiments:

- a. Although the microfiber adhesives used in the experiments had a significantly high adhesion, they all showed adhesion recovery to a notable extent. The results are in agreement with previous studies that have reported the mushroom-shaped tips as optimum tip shape for contamination and flaw resistance.
- b. Microfiber adhesives contaminated by particles much larger than the microfibers tips showed better and faster adhesion recovery compared to those contaminated with smaller microspheres. This shows that microfiber adhesives have better self-cleaning performance when contaminated with larger particles compared to smaller particles.
- c. completely cleaned adhesives (i.e. no contaminants remaining on the fiber tips) could not recover 100% of their initial adhesion before contamination due to damage to the microfibers. In this case, the damage is attributed to the high normal load applied during the experiments, and evident in the post-cleaning SEM images.
- d. Samples contaminated with particles much smaller than the microfibers tips showed great anti-fouling or contamination resistance. The exceptional anti-fouling capabilities of these microfibers to small contaminants is due to the ability of the microfiber tips to deform around the particle and still make good contact with the substrate - a phenomenon that has been shown to be peculiar to microfibers with mushroom tips. A theoretical model presented also suggests that the anti-fouling performance may be partly due to the adhesion contribution of a large quantity of microspheres making contact with the substrate.
- e. The poor self-cleaning performance of the samples contaminated with smaller microspheres was due partly to the deformation of the microfiber tips around the particles, which inhibited the particles from rolling or sliding with respect to the microfiber; and to the buckling of the microfibers which led to the microfibers making side contact with the substrate. Both of these scenarios are due to high normal loads and show that a high normal load during contact self-cleaning is detrimental to the process.

- f. Observations of the contributions of each of the load ing steps showed that approximately 5% of cleaning occurred during the loading and unloading steps, leaving the rest 95% to the drag step. Although this observation was not surprising based on the analysis using the contact self-cleaning model presented in this work, it was interesting to note that the same process of shearing of the samples, which under high loads can cause significant damage to the microfiber, is the crucial step required for cleaning.

Although these results contained a lot of insight to the contact self-cleaning process and exposed the critical step during the process, it was not sufficient to unravel the contact self-cleaning mechanism that dominated the load-drag-unload procedure, hence the need for a second experiment.

In the second experiment, the following observations were made:

- a. Particle motion during dragging in the LDU procedure was shown to be dominated by rolling. This experimental observation is in harmony with the model developed for contact self-cleaning under shear loading.
- b. The experiment also showed that particle motion at low load was dominated by rolling but with some sliding at the microfiber interface. This result is also in agreement with the previously derived model in 3.3.
- c. We showed by conducting further experiments that increasing the normal load or the drag speed during the dragging step both lead to an increase in the rolling friction. A model of the speed and normal load effect on rolling friction agrees with the current experimental results.

Finally, based on the broadened understanding of contact self-cleaning and the unveiled mechanism, we developed a method for simulating contact self-cleaning using the load-drag-unload procedure. A comparison of the simulation result and those obtained in Experiment I, shows very similar trends for the dependence of adhesion recovery on contaminant sizes. In Chapter 5, we will discuss how these results can be used to obtain microfiber adhesives with improved self-cleaning performance.

# **Chapter 5**

## **Design Considerations for Contact**

### **Self-cleaning of Microfiber Adhesives**

#### **5.1 Introduction**

There is currently a tremendous amount of information on design methodology for gecko-inspired microfiber adhesives with high adhesion and friction characteristics. A compilation of literature on gecko and gecko-inspired adhesives found in [36] contains several reports of successful design of synthetic microfiber adhesives with strong, directional and controllable adhesion to smooth surfaces. Some of these synthetic adhesives have achieved adhesive strengths similar, or even higher compared to that of the natural gecko on smooth surfaces [40, 74, 95]. However, no design method that addresses self-cleaning or anti-fouling of microfiber adhesives have so far been presented. The lack of a design methodology for the design of synthetic microfiber adhesives with contact self-cleaning or anti-fouling characteristics is the motivation for this work.

In the preceding chapters, we developed a model of adhesion and contact self-cleaning, and have presented experiments that uncovered the major factors that influence contact self-cleaning of microfiber adhesives. We will begin this chapter with a recount of these parameters and how



they influence contact self-cleaning and anti-fouling. In subsequent sections, these parameters will be used to provide design considerations for microfiber adhesives with enhanced contact self-cleaning performance while maintaining a good adhesion. We will also present design considerations for the design of microfiber adhesive for anti-fouling performance in Section 5.4. A chapter summary will be presented in Section 5.6.

## **5.2 Factors that Influence Self-cleaning and Anti-fouling of Microfiber Adhesives**

Based on the theoretical model and experimental results presented in the previous chapters, here are the factors that influence contact self-cleaning and anti-fouling in microfiber adhesives:

### **5.2.1 Microfiber Tip Shape**

The microfiber tip shape is known to be very crucial to the adhesive strength, controllability, and overall performance of microfiber adhesives [22, 32, 39, 51, 105, 128]. Of the several microfiber tip designs (Fig. 5.1), the mushroom-shaped tips have shown remarkable adhesion qualities. Recent work by Aksak et al. [4] presented the optimal shape for a mushroom-tipped microfiber with adhesive strength up to 97% of the intrinsic interface strength (theoretical limit). Thus it will be exciting to find out that the mushroom-shaped tips also contribute positively to self-cleaning and anti-fouling.

As shown in Fig. 5.1(b), microfibers with flat tips are desirable for contact self-cleaning compared to other shapes as they allow for a good contact between the particle and the substrate. This allows for efficient cleaning. Among flat-tipped microfibers, those with mushroom-shaped tips provide an added benefit to self-cleaning by allowing the microfibers to act as a reservoir for embedded contaminants (Fig. 5.1(c)). The same is true for microfibers with spatular tips, but in their case, the protrusion are not symmetric.

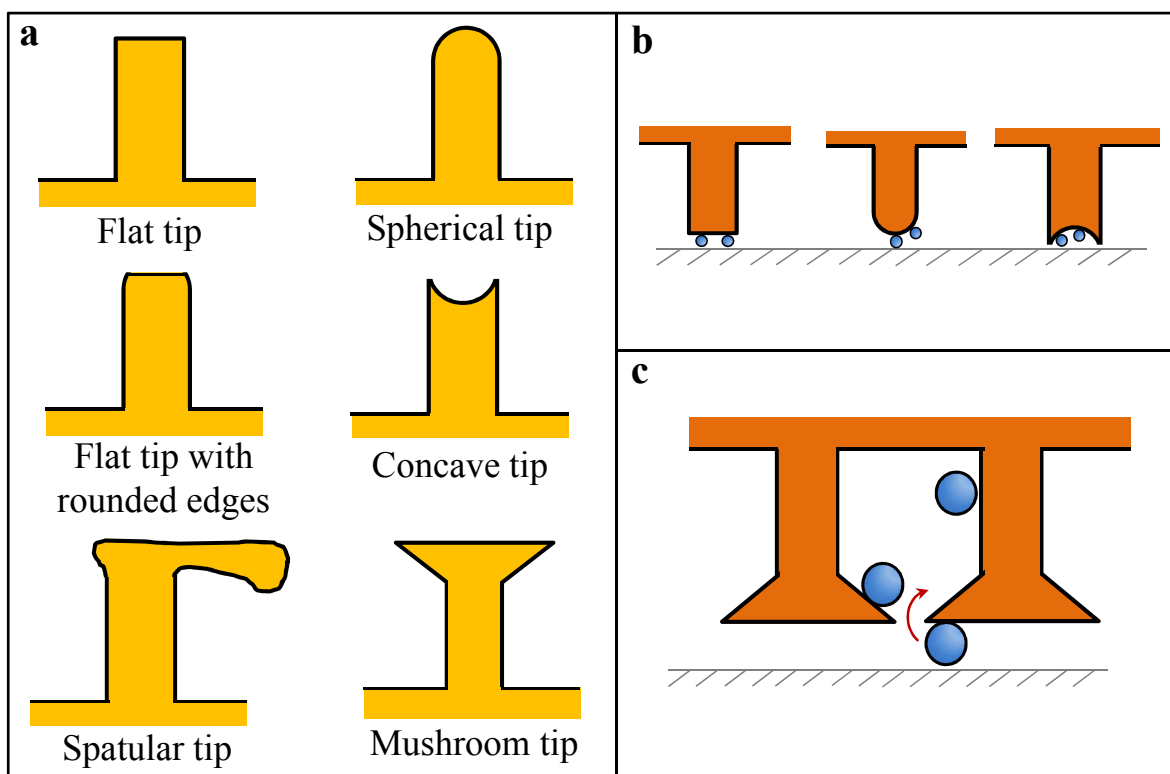


Figure 5.1: Microfiber tip shapes and their effect on self-cleaning. **(a)** Various tip shapes used in the design of microfiber adhesives. **(b)** Microfibers with flat tips are desirable for contact self-cleaning compared to other shapes as they allow for a good contact between several particles and the substrate. **(c)** Among flat-tipped microfibers, those with mushroom-shaped tips provide an added benefit to self-cleaning by allowing the microfibers to act as a reservoir for embedded contaminants.

The extraordinary adhesion performance of microfibers with mushroom-shaped tips is shown to be as a result of the robustness of the tips to flaws and contaminant. In fact, previous work by Carbone et al. [22] showed that as long as the crack width on the interface, due to the presence of a contaminant, is less than the microfiber stem diameter, the microfiber can retain a good measure of adhesiveness. This feature is also important and contributes to anti-fouling. Based on these reasons, microfibers with mushroom-shaped tips proves to be most efficient for adhesion as well as self-cleaning and anti-fouling performance.

### **5.2.2 Microfiber Tip Radius**

The microfiber tip radius plays a crucial role in self-cleaning as well as anti-fouling. It may actually be the most important geometric parameter that must be considered, based on the model and experimental results in the preceding chapters. In a broader scale, the self-cleaning performance of the small and large contaminant regimes showed that small microfiber tips (large contaminant regime) had better self-cleaning performance, while large microfiber tips (small contaminant regime) performed better in terms of anti-fouling performance. Narrowing down to each of these cases, while small microfiber tips are advantageous for contact self-cleaning, they are also beneficial for adhesion, especially for rough or irregular surfaces. On the other hand, large microfibers are beneficial for anti-fouling but have negative effect on adhesion. Later in this chapter, we will try to design the tip radius for optimal adhesion and anti-fouling performance.

### **5.2.3 Contaminant Size**

As discussed in the preceding chapters, the contaminant size can also affect the self-cleaning and anti-fouling performance of the microfiber array. Similar to our discussions of the effect of microfiber tip radius, contaminants that are much larger than the microfiber tips are easier to clean both by normal and shear loading, but could cause a complete loss of the adhesion for the

adhesive.

#### **5.2.4 Loading Condition**

Our model for self-cleaning by substrate adhesion showed that high normal load could lead to a poor self-cleaning performance. Our experiments for as well as theoretical model also showed that high normal load was detrimental to the self-cleaning performance due to increased friction and shear resistance at the microfiber interface. From the experiment, it was also observed that high normal load during cleaning caused damage to the microfibers and led to a complete loss of some of the adhesive's original adhesive strength. Thus, a low normal load is beneficial to self-cleaning.

Due to these several factors as well as application considerations, there is no general microfiber design that is optimum for self-cleaning and anti-fouling in various environment and for all applications. However, the microfiber can be designed for optimum self-cleaning or anti-fouling performance for a specific environment or for a desired task. Depending on the size of contaminants in an environment, microfiber adhesives can then be designed for optimal self-cleaning performance, given the application procedure. In the following sections, we will discuss design considerations and present a case study of microfiber adhesive design for optimal self-cleaning based on application procedure and application environment. Our belief is that, similar to chemical companies having different grades of chemical adhesives for optimum performance in various applications and environments (i.e., wood paints, metal paint, outdoor paint, etc.), manufacturers of microfiber adhesives can produce adhesives with optimum self-cleaning, anti-fouling and adhesion performance for various applications and different environments.

## **5.3 Microfiber Design Considerations for Self-cleaning Based on Application Procedure**

In Chapter 3, we presented two application-based loading procedures for microfiber adhesives, namely: the load-unload procedure, and the load-drag-unload procedure. Generally, most microfiber adhesive application steps fall within either of the two procedures.

### **5.3.1 Considerations for the load-unload procedure**

In applications where the loading condition are similar to the load-unload procedures (such as the use of microfiber adhesives for transfer printing), self-cleaning can only be effected using normal loads. This implies that the substrate adhesion mechanism must be enhanced. The condition for cleaning by substrate adhesion requires that the adhesive force of the substrate interface is greater than the adhesive force of the microfiber interface. Such condition can be met by (1) using a substrate material with a comparable adhesive strength to that of the adhesive, or (2) tuning the microfiber adhesive strength such that contaminants will be deposited. The later will required reducing the adhesive strength of the microfibers, which though achievable, may not be desirable. A third approach involves (3) controlling the adhesive force of the microfiber array by the preload force. This approach only limits the applied preload during the use of the microfiber adhesive and eliminates the need for a special microfiber array design as in option (2) or a special substrate material as in option (1). A last but easily implementable approach is (4) the use of microfibers with better anti-fouling capabilities. This may be the most practical approach based on our experimental observations that contact self-cleaning is less likely under normal loading condition. Thus, a microfiber with optimum anti-fouling properties for the desired application environment should be designed.

### 5.3.2 Considerations for the load-drag-unload procedure

Microfiber applications that mimics the load-drag-unload procedure, such as locomotion, or applications that involves shear loading of the microfibers allows for self-cleaning to be achieved easily as indicated by our experimental results in Chapter 4. Unlike the case with only normal load, self-cleaning is very likely during the shear loading by particle sliding along the microfiber interface and, most likely by particle rolling. To achieve self-cleaning, the following should be taken into consideration:

**Small microfiber tips:** The microfiber adhesive should be designed such that the microfiber tips are much smaller than the dominant contaminants. Based on the studies presented in this work, microfibers with small tips have been shown to outdo large microfibers with large tips in self-cleaning performance. Design of microfibers with small tips also has positive effect on the adhesion performance of the array in most cases, except for very rough surfaces where long microfibers are desirable. Thus, the design of microfibers with small tips is usually a good practice.

**Low normal load:** Low normal loads should be used during application to prevent damage to the microfibers in the dragging step.

**High substrate friction:** Based on the condition for contact cleaning under a combined normal and shear load given in equation 3.13, the applied shear force should be less than the critical shear force at the substrate interface. One of the ways to achieve this is by using substrates with high friction coefficient. Such high friction surfaces with inhibit particle sliding along the substrate and effectively increase the cleaning region for a cleaning map like that shown in Fig. 3.7. However, a high friction substrate may also have the tendency to cause damage to the microfiber tips when in contact.

**Patch size and groove design:** For particle much larger than the microfiber tip to be cleaned, they must be completely removed from the microfiber array. This implies that the size of the array determines the number of cleaning steps that must be taken before the particles are completely cleaned. A solution to this problem for very large array is to pattern grooves onto the microfiber array as temporal contaminant storage. Grooves and deep wells can be patterned into the array to collect rolling and sliding particles. Experimental results in Chapter 4 showed that particle embedding is a dominant process in contact self-cleaning. This means that the patterning of grooves onto the array will be a great design practice as it increases the efficiency of the embedding process. The natural geckos possess skin folds called lamellae at the base of their fibrillar structures which help to enhance self-cleaning in the animal by acting as a cavity where contaminants can be embedded for a long period of time before the skins are regenerated. Similarly, microfiber adhesives with grooves mimicking the lamellae in geckos will make embedding more efficient and enhance contact self-cleaning.

The results of a preliminary study of the advantage of implementing a groove pattern in the microfiber adhesive array, conducted by Y. Menguc [95] are shown in Fig. 5.2. Mushroom-tipped microfiber array with  $95\ \mu\text{m}$  tip diameter and  $105\ \mu$  length were used in the study. The patch was patterned such that the raised ridges were four pillars wide ( $550\ \mu\text{m}$ ) and the intervening gaps were two pillars wide ( $225\ \mu\text{m}$ ), which resulted in approximately 67% area coverage by the adhesive structures. The microfiber array with groove and a control without groove were contaminated by glass spheres with diameter of  $110\ \mu\text{m}$ . By manual manipulation of the adhesive to simulate the load-drad-unload procedure, the groove-patterned adhesive demonstrated a significantly better cleaning compared to the non-patterned sample.

As evident in the study, the grooves take the place of the microfibers and reduce the overall performance of the adhesive (33% less adhesives was reported in the study presented). However, for optimum design, we propose that hexagonally patterned deep grooves with groove width no more than 150% the size of contaminants, should be implemented. The use of hex-patterned

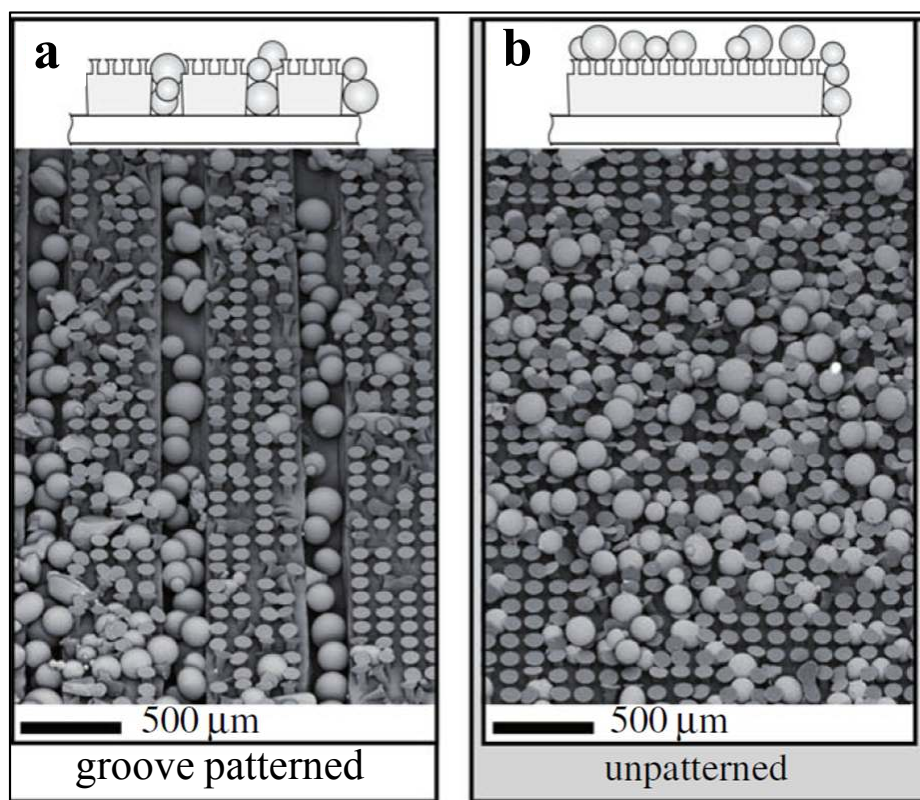


Figure 5.2: Results of a preliminary study to show the advantage of implementing a groove pattern in the microfiber adhesive array. **(a)** SEM image of a microfiber adhesive patch with groove showed an extensively cleaned microfiber array when compared to **(b)** an SEM image of an unpatterned adhesive after similar cleaning steps. The experiments were conducted by Y. Menguc [95].



grooves as opposed to long groove strips used in the preliminary study, eliminates the need to align the groove perpendicular to the direction of drag. Hex-packed grooves will also reduce the stresses on the grooves which could lead to damage of the adhesive. In fact, most natural adhesive systems possess groove design that may have evolved to aid contaminants embedding (See Fig. 5.3).

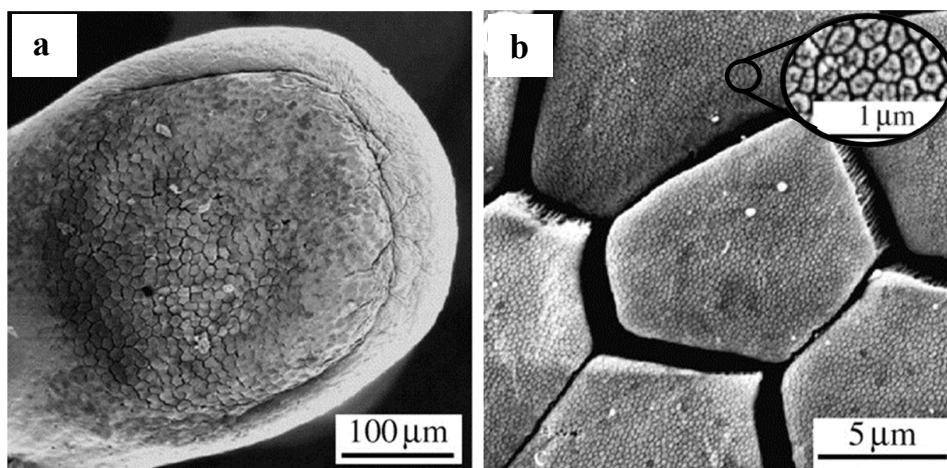


Figure 5.3: Morphology of tree frog toe showing hexagonal patterned adhesive pad [37]. **(a)** SEM image of the toe pad **(b)** SEM image of the epidermis showing hexagonal patterned grooves. The grooves may have also evolved to aid contaminant embedding, besides the already known function of secreting mucus for wet adhesion. (Inset) High-magnification image of the surface of a single hexagonal cell showing peg-like projections.

## 5.4 Microfiber Design Considerations for Anti-fouling

As discussed earlier, there are cases where microfiber design for self-cleaning may not be the best option from a design or application standpoint. The alternative in such cases will be to design the microfiber adhesive for optimal anti-fouling performance. Our review of various microfiber tips have shown that microfibers with mushroom tips are best for adhesion performance as well as self-cleaning and anti-fouling performance. The following must be considered for self-cleaning performance:

**Mushroom-shaped tip design:** The microfiber adhesives should be designed with mushroom tip decorations. Our analysis of various microfiber tip design earlier in this chapter showed that microfibers with mushroom shaped tips has better resistance to contaminants compared to other tip designs. Hence, a practical design for anti-fouling must begin with microfibers with mushroom-shaped tips.

**Large microfiber tip size:** Self-cleaning experiments presented in this work have shown that microfibers with large tips are favorable for anti-fouling (refer to Fig. 4.1). This is because microfibers with large tips can deform around the particles to make contact with the substrate. On the other hand, increasing the tips of the microfiber would lead to lower adhesion performance of the array. Thus, it is important to optimize the microfiber tip size based on the size of contaminants prevalent in the application environment.

Carbone et al. [22] have shown that the microfibers with mushroom-shaped tips are able to retain a significant portion of their initial adhesion as long as the gap width  $a_p$  due to a contaminant particle is less than the microfiber stem radius  $a$ . So that the tip size can be optimized for both adhesion and anti-fouling by letting  $a = a_p$ . In this case the adhesive force of the contaminated microfiber is given as

$$F = \left( \frac{\pi \omega E^*}{2 a_p} \right) \pi a_t^2, \quad (5.1)$$

where  $\omega$  is the work of adhesion of the interface,  $E_f^* = E_f / (1 - \nu_f^2)$  is the effective modulus of the interface,  $E_f$  is the Young modulus of the microfiber,  $\nu_f$  is the poisson ratio of the microfiber, and  $a_t$  is the microfiber tip radius.

**High preload:** For optimum adhesion of contaminated adhesives under normal loads only, it is important to apply sufficient load that is enough to make the microfibers to deform around the contaminants and make contact with the substrate, but less than the critical buckling force

(for vertical microfibers). Overall, high preloads in this case will ensure higher contact area and effectively, better adhesion.

## 5.5 Case Study: Design of a Self-cleaning Microfiber Adhesive Patch for Use in an Office Environment

Let us consider a situation where microfiber adhesives with optimal adhesion or self-cleaning performance are desired for use in an office environment. We will present two scenarios based on the application of the adhesive. In the first case, we will assume that the adhesive will be implemented under normal and shear loading, for example on the fingers of a humanoid robot for enhanced gripping, or as a residue-free attachment mechanism for hanging a white board to office walls.

As discussed earlier, we will use microfiber adhesives with mushroom shaped tips. The microfiber geometry will be optimized for adhesion by setting the microfiber tip radius to be 1.1 times the stem radius [4]. The microfiber length will also be optimized based on the equation for lateral stability of the microfibers in an array given in 2.10 as

$$L = \left( \frac{\pi^4 E_f^* a}{2^{11} \gamma_f} \right)^{1/12} \left( \frac{3 E_f a^3 S^2}{\gamma_f} \right)^{1/4}, \quad (5.2)$$

where  $\gamma_f$  is the surface energy of the microfiber material, and  $S$  is the edge-to-edge distance between the microfibers.

For optimal self-cleaning or anti-fouling performance in an office setting, it is important to know the sizes of contaminants present in the environment. Thus, we conducted a literature survey to find the size distribution of dirt particles in offices. A very good analysis of dust and dirt particles was conducted by Molhave et al. [99] in which they analyzed about 11 kg of dusts collected from seven Danish office buildings with approximately 1047 occupants. Result of the

Particle size ( $\mu\text{m}$ )	Percentage composition (wt %)
0-3	< 0.1
3-6	0.1
6-10	0.4
10-25	6.3
25-50	12
50-125	41
> 125	40

Table 5.1: Size distribution of about 11 kg of bulk dust obtained from seven Danish office buildings with about 1047 occupants [99].

size distribution of the dust particles is shown in Tab. 5.1. From the table, 40% of the dirt particles greater than 125  $\mu\text{m}$ , 81% were greater than 50  $\mu\text{m}$ , 93% were greater than 25  $\mu\text{m}$ , and 99.3% were greater than 10  $\mu\text{m}$ , based on weight composition. As always, we will assume that the particles are spherical.

**Microfiber radius:** Assuming we are making our design based on the size of 93% of the particles, this would require that particles with diameter greater than 25  $\mu$  should be in the large contaminant regime. In the experimental study presented in 4.2, it was observed that particles with diameter greater than 2 times the microfiber tip diameter, had similar cleaning behavior as much larger particles so that they were considered in the large contaminants regime. Using the same ratio, the microfiber tip diameter should be at most 12.5  $\mu\text{m}$ , so that  $a_t = 6.25 \mu\text{m}$ . Assuming a dense parking so that  $S = 2a_t$ , the microfiber edge-to-edge spacing will be 12.5  $\mu\text{m}$ , and the microfiber length obtained from equation 5.2 is 65.4  $\mu\text{m}$ , where  $E_f = 2.9 \text{ MPa}$ ,  $\nu_f = 0.5$ , and  $\gamma_f = 50 \text{ mJ/m}^2$ .

**Groove pattern:** For a more efficient self-cleaning by particle deposition, there is a need to pattern grooves into the array to serve as temporary storage for cleaned contaminant. However,

as mentioned earlier, the implementation of groove design leads to a loss in the adhesive strength of the array.

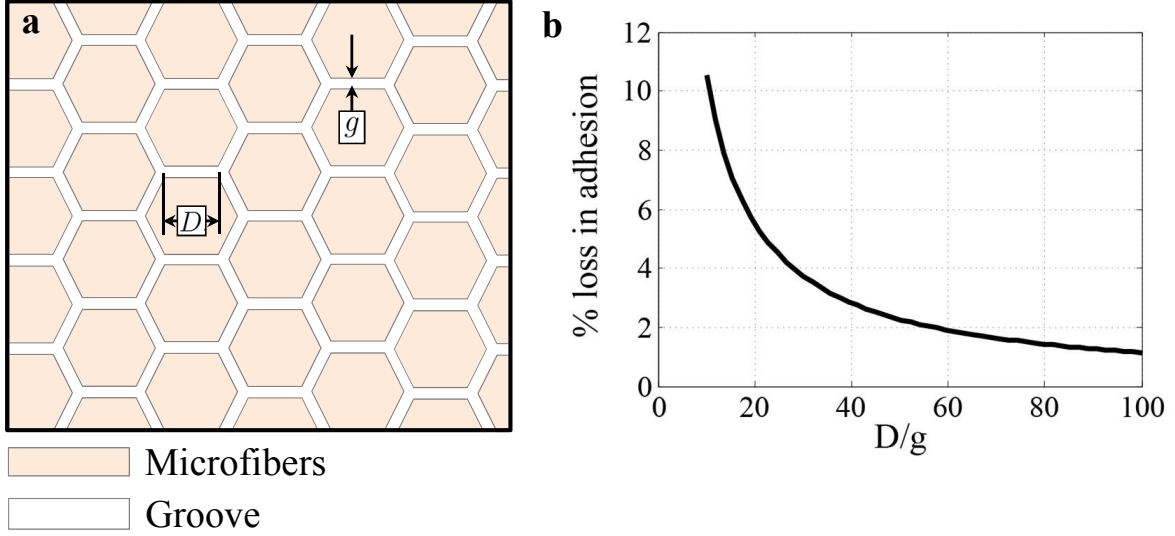


Figure 5.4: **(a)** Schematic view of a microfiber array with hexagonally patterned groove. **(b)** Graph of percentage loss in adhesion as a function of groove size ratio.  $D$  is the side length of the hexagonal pattern, and  $g$  is the width of the groove.

Thus, to implement a groove design, it is important to know the area ratio of adhesive displaced by the groove, in order to make sure that the array retains enough adhesion to perform it's desired task. For a hexagonally patterned groove design (Fig. 5.4(a)), with groove width  $g$  and hexagon length  $D$ , the area fraction  $\phi$  of the groove is given as

$$\phi = \frac{g(6D + \sqrt{3}g)}{(\sqrt{3}D + g)(3D + \sqrt{3}g)}, \quad (5.3)$$

which in expanded series form is

$$\phi = \frac{2g}{\sqrt{3}D} - \frac{g^2}{D^2} + \frac{4g^3}{3\sqrt{3}D^3} - \frac{5g^4}{9D^4} + 0 \left( \left( \frac{1}{D} \right)^5 \right). \quad (5.4)$$

For  $D \gg g$ , we can drop the second term in the series so that

$$\phi = \frac{2g}{\sqrt{3}D}. \quad (5.5)$$

A graph of the % loss in adhesion of the array as a function of  $D/g$  is shown in Fig. 5.4(b). The plot shows that for groove patterns with  $D/g > 11$ , the percentage of lost adhesion in the array is less than 10%.

For the groove size, the groove should be wide enough to lodge most of the particle sizes. Unfortunately, the data given in Tab. 5.1 does not provide enough information to determine the upper range of the contaminant. However, we will assume a groove with of  $200 \mu\text{m}$  so that we can retain particles less than  $200 \mu\text{m}$  in the groove. For a 10% less adhesion ( $\phi = 0.1$ ), the side length of the hexagonal pattern is obtained from equation 5.5 as  $\sim 2.3 \text{ mm}$ .

## 5.6 Summary

In this chapter, we combined our findings from previous chapter to develop a concise list of factors that are vital to contact self-cleaning and anti-fouling. Interestingly, most of the factors that are beneficial for adhesion are also advantageous to contact self-cleaning. A review of various tip shapes showed that mushroom-shaped tip, which is so far the optimum tip geometry, is more advantageous for contact self-cleaning compared to other tip design. Similarly, small microfiber tips are advantageous to both adhesion and contact self-cleaning.

Due to the environmental and application factors, we believe that no single microfiber design is best for all environments and applications. Rather, microfiber adhesives can be designed for optimum cleaning performance for a given application or for a desired environment, by taking some key factors into consideration. For applications that utilized only normal loads (load-unload procedure), best practice will be the design of the microfiber for anti-fouling since self-cleaning is not easily achieved with normal loads only, except with specially designed substrate,

which is usually not the case in real world applications.

Apart from the size and structure of the individual microfiber, the size of the adhesive sample also plays a crucial role in the adhesion recovery process. Large microfiber patches will require more steps before to remove the contaminants from the array. To resolve this problem, we propose the design of hexagonally patterned groves to serve as temporal storage for rolling and sliding contaminants. A revisit of the natural gecko's adhesion system suggests that the lamellae on the gecko toes, serves a similar purpose as a temporal storage for contaminants. In fact, most natural adhesive and friction mechanisms employs the grove design, possibly for this purpose. We should that depending on the ratio of the groove width to the side length of the hexagonal pattern, the effect of groove implementation on the adhesive strength of the array is considerably low.

Based on the divergent nature of the parameters involved in contact self-cleaning, we proposed that different grades of gecko inspired microfiber adhesives can be manufactured for better performance in different applications and in various environments, similar to how current chemical companies make adhesives or paints for based on application or environment. I.e., wood paint, metal paint, outdoor paint, etc. The end user or design specialist, can then select an appropriate grade, depending on the intended usage procedure or environment.

Using a case study, we investigated the design of microfiber adhesive for use in an office environment. Our result showed that microfibers with tip diameter less than  $12.5\ \mu\text{m}$  should be able to self-clean in an office environment, for application procedures that involve shear loading.

# Chapter 6

## Summary and Conclusion

### 6.1 Overview of Contributions

This work was motivated by open questions related to adhesion modeling in microfiber adhesives and the lack of a thorough understanding of self-cleaning in gecko-inspired microfiber adhesives. In this thesis, solutions to the questions were provided and in-depth insight were presented through the following contributions:

#### 6.1.1 Adhesion Modeling for Microfiber Adhesives

A model of microfiber adhesion was presented that improved on previous model by taking the deformation of the backing layer under an individual microfiber into consideration. Microfiber array deformation under a spherical indenter was also modeled to show the load-indentation, and load-contact area relationship for microfiber adhesives. The developed model is useful for predicting the number of fiber in contact with a single particle under a given normal load, or indentation distance. The model is also useful for obtaining the contact area of a microfiber adhesive array for friction analysis.

The dependence of pull-off force on the rate of retraction for microfiber adhesives was



modeled. Experiments and finite element simulations were conducted to show that the rate effect on adhesion is a function of the crack propagation speed at the interface, and mainly due to interfacial viscoelasticity. It was concluded that the influence of the bulk material properties is negligible. The model developed was validated by experiments, and can be used to predict the change in adhesion due to a change in crack propagation speed of an adhesive interface.

A procedure for simulating the adhesive force of a microfiber adhesive array in contact with a spherical surface was also presented. The simulation provided can be used to predict the effect of the microfiber geometric and material properties, as well as loading conditions, on the adhesive force of a microfiber adhesive array.

### **6.1.2 Mechanisms of Self-cleaning**

A general definition for self-cleaning of microfiber adhesives was presented along with a broad review of the possible mechanisms of self-cleaning. Three major categories of self-cleaning were identified as wet self-cleaning, dynamic self-cleaning, and contact self-cleaning. The mechanisms associated with each of the categories of self-cleaning were also identified and discussed. A total of seven self-cleaning mechanisms were identified which include rolling of a water droplet, capillary adhesion, vibration and agitation, digital hyperextension, substrate adhesion, particle rolling, and particle sliding on microfibers, and the last three were grouped under contact self-cleaning. A new approach for self-cleaning that involved the temporary embedding of the particle inside the microfiber adhesive array was proposed as an effective cleaning process.

### **6.1.3 Mechanics of Contact Self-cleaning**

The mechanics of self-cleaning by substrate adhesion, particle rolling, and particle sliding on the microfiber, were developed. The models addressed two categories of contaminants based on the ratio of the microfiber diameter to the contaminant diameter. Two cases of loading

procedures, namely the load-unload procedure and the load-drag-unload procedure were also investigated in the model. The model predicted that cleaning by substrate adhesion will occur only when the adhesive force of the substrate on the contaminant is greater than the adhesive of the microfiber adhesive on the contaminant. For hard contaminants smaller than the microfiber tips, this condition implies that the work of adhesion of the substrate interface should be greater than  $3/4$  of the work of adhesion at the microfiber interface.

For contaminants much larger than the microfiber tips, the model predicted that cleaning would occur when the preload force is low, such that the adhesive force at the microfiber interface is at its minimum. The model also predicted that self-cleaning will occur during dragging when the critical rolling friction, or the sliding friction at the microfiber interface is less than the critical sliding friction at the substrate interface. For large contaminants, the model predicted that low normal loads, which results in a low contact area at the microfiber interface, is beneficial to self-cleaning.

#### **6.1.4 Experiments and Simulation of Contact Self-cleaning**

Detailed experiments of contact self-cleaning were conducted using the load-drag-unload cleaning procedure. The experiments showed that small microfiber sizes with microfiber tips smaller than the size of the contaminants, have better contact self-cleaning characteristics compared to large microfiber tips. On the other hand, microfibers with tips much larger than the size of the contaminant possess better anti-fouling characteristics. High normal loads during the experiments were shown to cause damage to the microfibers, much so that up to 20% of the initial adhesion were completely lost and could not be recovered even after a complete removal of all the contaminants from the adhesive.

Further experiments showed that particle rolling was the dominant contact self-cleaning mechanism when using the load-drag-unload cleaning procedure with spherical contaminants. Experimental analysis and a model of the effect of normal loads and drag speed both showed

that increasing the normal load or drag speed both led to an increase in the critical rolling friction, with negative self-cleaning consequences.

Based on the uncovered mechanism of self-cleaning in microfiber adhesives, a simulation method was presented for simulating contact self-cleaning using the load-drag-unload procedure. The simulation results confirmed that large contaminants ( $\geq$  microfiber tips) are cleaned faster compared to small contaminants.

### **6.1.5 Design Considerations for Microfiber Adhesives with Contact Self-cleaning or Anti-fouling Characteristics**

Several parameters that influence self-cleaning and anti-fouling that were uncovered in this study were presented. The mushroom tip shape was found to be more favorable for both self-cleaning and anti-fouling compared to other microfiber tip shapes. The design of grooved patterns on the microfiber adhesive array was shown to be favorable for contact self-cleaning, although it could also lead to a loss in the overall adhesion of the microfiber array. A method for obtaining the groove parameters for minimum effect on adhesion, was presented. The design guidelines presented can be used to obtain microfiber adhesives that are suitable for use in a given environment or with a given application procedure.

The results presented in this work also suggests that the sub-micron size of the gecko's spatulae supports its self-cleaning functionality. Also, the gecko's lamellae is believed to play a key role in self-cleaning by acting as a temporary storage for embedded contaminant.

## **6.2 Outlook**

Microfiber adhesives are becoming very attractive for use in several application areas due to its numerous features. One of the challenges of microfiber adhesives has been identified as the presence of contaminants in real world environment, which could lead to a complete loss of

adhesion. Although fibrillar adhesives possess better resistance to contamination than conventional pressure sensitive adhesives, this thesis work presents a thorough study of self-cleaning and anti-fouling of microfiber adhesives that takes us closer to overcoming the problems of contamination. If followed, the design guidelines presented for self-cleaning and anti-fouling could lead to the design of microfiber adhesives with robust adhesion and self-cleaning performance in various environments. Considering its numerous functionalities, gecko-inspired microfiber adhesives could serve as a better alternative to some adhesive mechanism currently employed in industrial, medical and consumer settings.

In this thesis, contact self-cleaning was investigated using spherical micro-particles as contaminants. Future work to study the effect of particle shapes and roughness on self-cleaning would be necessary in order to extend the current work to various dirt and dust geometries. Some of the characteristics of self-cleaning investigated here are also useful for pick-and place applications of microfiber adhesives, so that the design considerations presented can also be applied to tackle other problems not directly related to contamination.

Similar to the various grades of present day glue or chemical adhesives (wood glue, metal glue, high temperature glue, etc.), the future for microfiber adhesives will certainly comprise of various grades of the adhesive that end users can select from, depending on the intended application process or environments.

This thesis work takes us closer to the design of robust, anti-fouling, and self-cleaning gecko-inspired microfiber adhesives for numerous applications in various environments.

# Appendix A

## Numerical Simulations

### A.1 Simulation Steps for Obtaining the Indentation Distance of a Spherical Indenter on a Microfiber Array

The following steps can be used to obtain the indentation distance of a spherical indenter on a microfiber array, for a specified preload (Fig. A.1). A schematic diagram of the loading condition is given in Fig. 2.2.

1. Specify a desired preload  $P$ .
2. Guess an initial indentation distance  $\Delta$ . A small initial value is preferred.
3. Generate array of microfibers with  $n_f$  number of microfibers in each row,  $i$  and column,  $j$  such that  $n_f > 2r_c/d$ .  $r_c$  is the contact radius of the sphere with the array and is given as

$$r_c = \sqrt{R^2 - (R - \Delta)^2}, \quad (\text{A.1})$$

$d = S + 2a$  is the center-to-center spacing between adjacent microfibers. For hexagonally

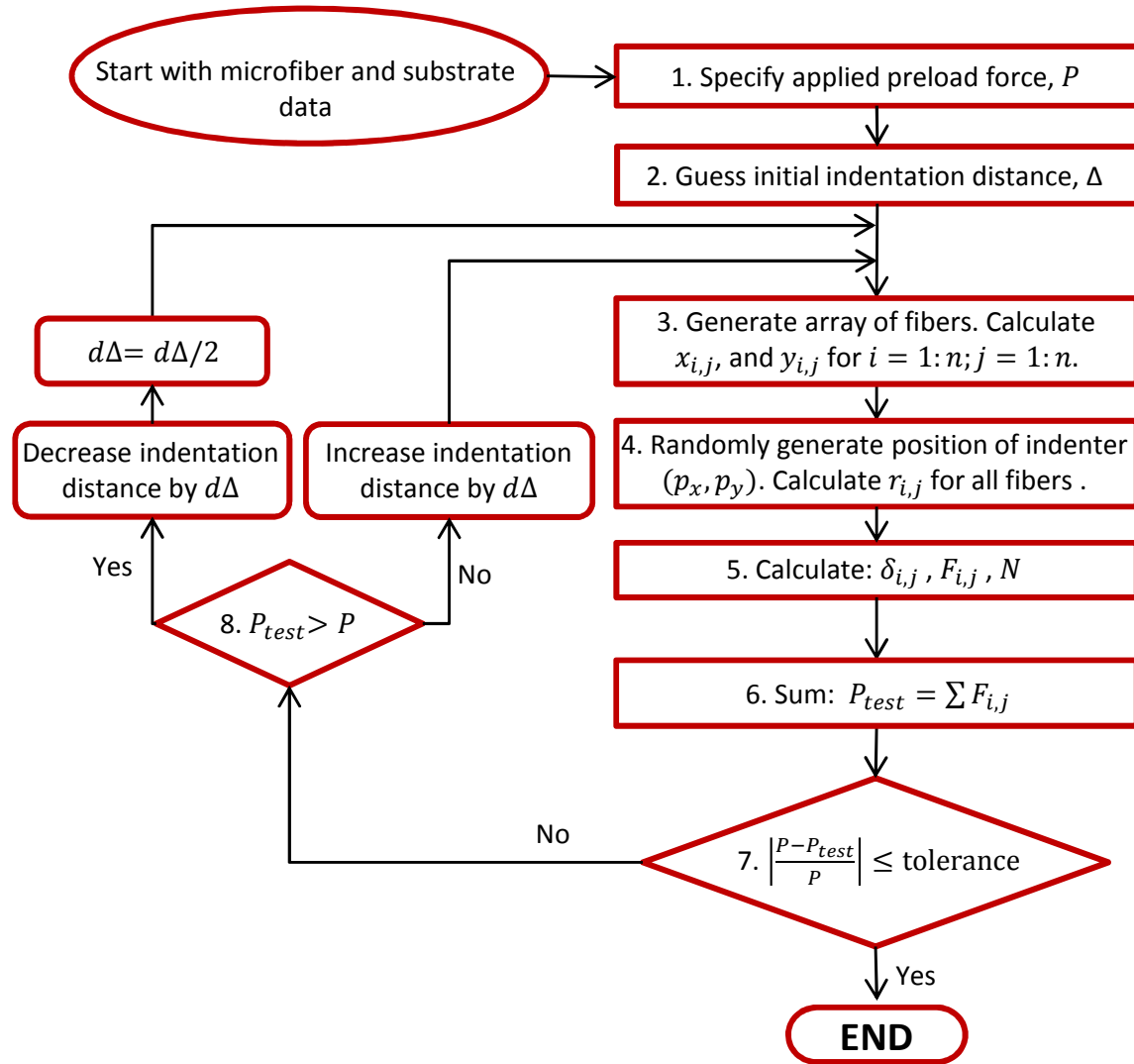


Figure A.1: Flowchart for finding the indentation distance  $\Delta$  of a spherical indenter of radius  $R$  for a given normal load  $P$ .  $r_{i,j}$ ,  $\delta_{i,j}$ , and  $F_{i,j}$  are the radial distance from the center of the sphere, the indentation distance and the reaction force, respectively, of a microfiber in row  $i$  and column  $j$ .  $(p_x, p_y)$  are the  $x$  and  $y$  coordinates of the indenter in the microfiber array.  $N_f$  is the number of microfibers in contact with the substrate.  $P_{test}$  is the estimated preload obtained from each iteration. This routine is valid for compressive load only.

arranged microfibers, the coordinates of each microfiber is given as

$$x(i, j) = \begin{cases} d((j - 1) + 0.5) & \text{for odd values of } i \\ d(j - 1) & \text{for all other values} \end{cases} \quad (\text{A.2})$$

$$y(i, j) = jd\sqrt{3}/2$$

4. Randomly generate the position  $(p_x, p_y)$  of the indenter on the microfiber surface, such that it is within a radius of  $0.5d$  from the center of the array. Obtain the radial distance from the center of each microfiber to the center of the sphere given as

$$r_{i,j} = \sqrt{(x_{i,j} - p_x)^2 + (y_{i,j} - p_y)^2}. \quad (\text{A.3})$$

5. Obtain the deformation of each microfiber  $\delta_{i,j}$ . For microfibers with  $\delta_{i,j} < \delta_{cr}$  the force acting on the microfiber is obtained by solving for  $F$  in Eqn. 2.6, but when  $\delta_{i,j} \geq \delta_{cr}$ ,  $F_{i,j} = F_{cr}$ .  $N_f$  is obtained as the number of microfibers with  $F_{i,j} > 0$ .
6. Sum up all  $F_{i,j}$  to obtain  $P_{\text{test}}$
7. Check whether

$$\left| \frac{P - P_{\text{test}}}{P} \right| \leq \text{tolerance}. \quad (\text{A.4})$$

If the result of Eqn. A.4 is true, we have obtained an approximate value of  $\Delta$  for the given  $P$ . Otherwise, we adjust the value of  $\Delta$  accordingly and return to *step 3*, and the simulation is repeated until Eqn. A.4 is satisfied. Although the preceding routine is used for obtaining the value of  $\Delta$  for a known value of  $P$ , it can also be used to obtain  $P$  for a known value of  $\Delta$ . The model and simulation given above is valid only for compressive load.

## A.2 Simulation Steps for Contact Self-cleaning of Microfiber Adhesives Based on the Load-Drag-Unload Procedure

The following are steps for simulating contact self-cleaning based on a load-drag-unload cleaning procedure. The simulation is separated into three levels similar to the load drag unload experiment (Fig. A.2. A schematic diagram of the microfiber array and contaminant dimension can be found in Section 4.4.

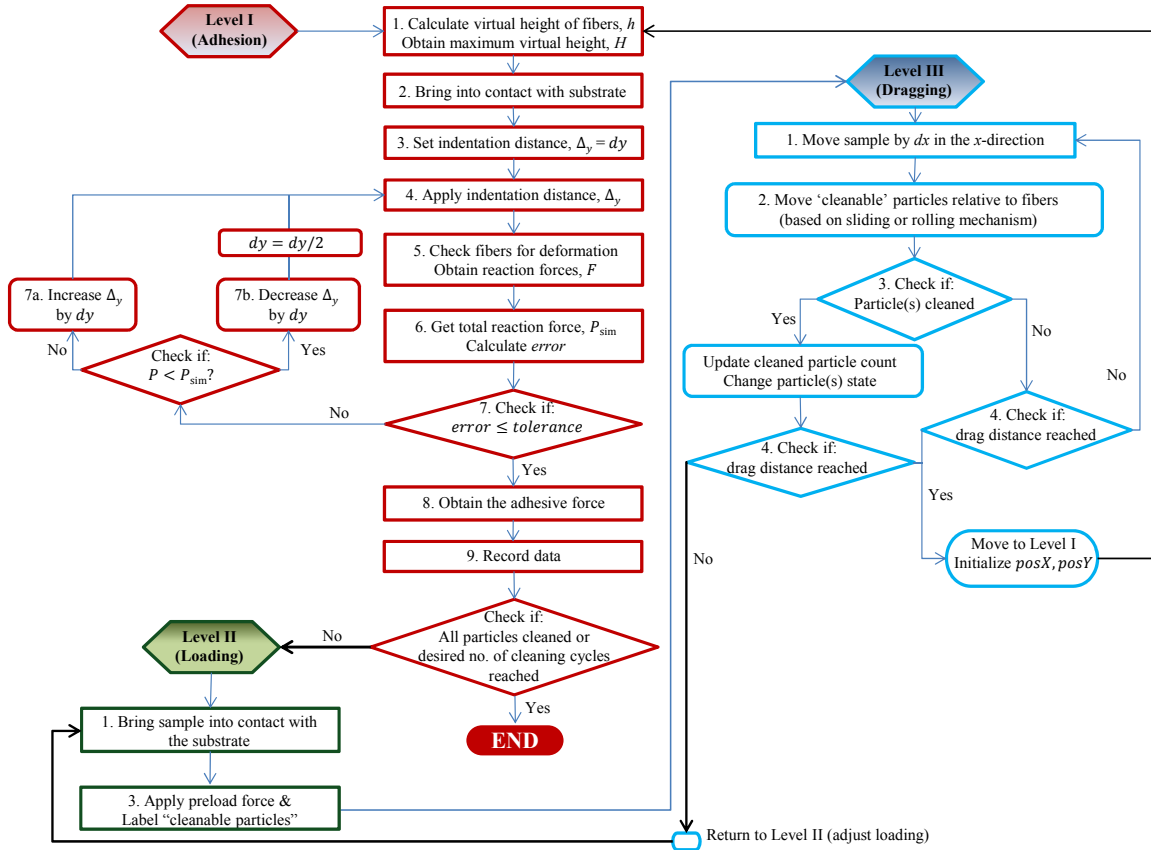


Figure A.2: A numerical simulation flow chart for contact self-cleaning of microfiber adhesives using the load-drag-unload procedure. Similar to the load-drag-unload contact self-cleaning experiments, each cleaning cycle is separated into three (3) levels. In Level I, the adhesive force of the contaminated microfiber adhesive is obtained. In Level II, the adhesive is pressed against the substrate until the desired preload is reached. In Level III, the sample is dragged against the substrate by small increments until the specified drag distance is reached. If a particle is cleaned after any drag step and the drag distance has not been reached, the simulation returns to Level II, where the indentation distance and the number of contacting microfibers are readjusted.



### A.2.1 LEVEL I: Obtaining the Adhesive Force of a Contaminated Microfiber array

1. Calculate the virtual heights of all microfibers. The virtual height  $h(j)$  of each microfiber  $j$  and obtain the maximum virtual height  $H$
2. Bring sample into contact with the substrate at zero load. The sample is in contact with the substrate at zero loading when  $posY = H$ .
3. Set initial indentation distance  $\Delta_y$ , i.e.,  $\Delta_y = dy$ .
4. Apply indentation distance by setting  $posY = H - \Delta_y$ .
5. Check for microfiber deformation. Microfiber  $j$  is compressed if  $h(j) > posY$ . When this occurs, the microfiber state  $f_{\text{STATE}}(j)$  is set to 1 for  $h(j) > L$  and 2 for  $h(j) = L$ . The reaction force  $F(j)$  of each microfiber is obtained as

$$F(j) = \begin{cases} (h(j) - posY)/C & \text{if } h(j) > posY \\ 0 & \text{otherwise} \end{cases} \quad (\text{A.5})$$

where  $C = L/(\pi a^2 E_f) + 2/(3aK)$  the microfiber compliance as derived in Section 2.2 in Chapter 2,  $E_f$  is the Young's modulus of the microfiber, and  $K$  is the effective modulus of the interface.

6. Obtain the simulated reaction force on the array  $P_{\text{sim}}$  given by

$$P_{\text{sim}} = \sum_j^n F(j). \quad (\text{A.6})$$

Then, obtain the error of the reaction force in comparison to the applied load  $P$  as

$$\text{error} = \left| \frac{P - P_{\text{sim}}}{P} \right|. \quad (\text{A.7})$$

7. Check if the desired tolerance is satisfied, i.e.,  $error \leq tolerance$ . If the tolerance is satisfied, continue to Step 8. If the tolerance is not satisfied, decrease  $\Delta_y$  by  $dy$  if  $P < P_{sim}$  or increase  $\Delta_y$  by  $dy$  if  $P > P_{sim}$  and return to Step 4.
8. Obtain the adhesive force of the array due to microfibers and particles contacting the substrate. Let  $P_{dirty,f}$  be the contribution of the contacting microfibers, and  $P_{dirty,p}$  be the contribution of the contacting particles.  $P_{dirty,f}$  is obtained as

$$P_{dirty,f} = \sum_{j=1}^{N_f} F(j), \quad \text{for } f_{STATE} = 2 \quad (\text{A.8})$$

Check for particles in contact and change  $p_{state}$  to 1.

$$p_{state}(i) = \begin{cases} 1 & \text{if } 2R(i) > (posY - L) \\ 0 & \text{Otherwise} \end{cases} \quad (\text{A.9})$$

where  $p_{state}(i) = 2$  are cleaned particles and no longer considered in the simulation. For the particle contribution to adhesion using the DMT theory,

$$P_{dirty,p} = \sum_{i=1}^{N_p} 2\pi w_{ps} R(i), \quad \text{for } p_{state} = 1 \quad (\text{A.10})$$

where  $N_p$  is the total number of particles and  $w_{ps}$  is the work of adhesion of the particle-substrate interface.

9. The value of the adhesive force is stored

## A.2.2 LEVEL II: Applying a Normal Load to Simulate Loading

- 2.1. Bring sample into contact with the substrate. This is achieved similar to 1 and 2 of LEVEL I.
- 2.2. Apply preload force by following Step 4 through 7 of LEVEL I until the desired preload

is reached.

Label particles as shown in Equation A.9. Particles with  $p_{\text{state}} = 1$  can be cleaned. store date for use in LEVEL III

### A.2.3 LEVEL III: Applying a Horizontal Displacement to Simulate Dragging

3.1. Move sample in the positive x-axis by a small distance  $dx$ . i.e.  $posX = posX + dx$ .

3.2. Move the position of ‘cleanable’ particles by  $\delta x$  in the negative x-axis relative to the microfibers. i.e.

$$x_p(i) = x_p(i) - \delta x, \quad \text{if } p_{\text{state}}(i) = 1 \quad (\text{A.11})$$

For cleaning by particle rolling,  $\delta x = dx/2$ , and for cleaning by particle sliding on microfibers,  $\delta x = dx$ .

3.3. Check if any of particles are cleaned. A particle is cleaned when its position is outside the microfiber array, i.e.,

$$p_{\text{state}}(i) = 2 \quad \text{if } [x_p < x_f(1) - a] \text{ or } [x_p > x_f(N_f) + a] \quad (\text{A.12})$$

Also, if a particle’s diameter  $R(i)$  is smaller than the microfiber length i.e.  $2R(i) < L$  and the spacing between the tips of adjacent microfibers i.e.  $2R(i) < g$ , the particle can also be cleaned when its position is between adjacent microfiber tips i.e.  $[x_f(j) + a] < x_p(i) < [x_f(j + 1) - a]$ . If cleaning occurs, the  $p_{\text{state}}$  of the cleaned particle is changed to 2 and the number count of cleaned particles is adjusted. Particles with  $p_{\text{state}} = 2$  are assumed to be non-existent in subsequent steps.

3.4. Check if the desired drag distance  $\Delta_x$  is reached, i.e.  $posX \geq \Delta_x$ . If  $\Delta_x$  has been reached, the values of  $posX$ ,  $posY$ , and  $h(j)$  are reinitialized to 0, and the number cleaning cycle

is updated before returning to LEVEL I.

If  $\Delta_x$  has not been reached, but particles were cleaned in Step 3, the values of  $h(j)$ ,  $H$ , and  $p_{\text{state}}$  for all particles must be readjusted in LEVEL II to account for the change in the loading condition.

## Appendix B

# Visualization of the Contact Area Using Interferometric Microscopy

Interferometric microscopy was used in some of the studies conducted to obtain a more accurate contact area measurement. When light is reflected between two surfaces separated by a small gap, it generates a pattern formed from the constructive and destructive interference of the reflected wave, which is a function of the gap between the two surfaces. When viewed with a monochromatic light source with a known wavelength  $\lambda$ , it results in a pattern of bright and dark rings (for a spherical surface and a flat surface) known as Newton's rings. The dark rings are as a result of destructive interference between the light rays, where the gap between the two surfaces is an odd multiple of  $\lambda/2$  so that the reflected waves are  $180^\circ$  out of phase; while the bright rings are due to constructive interference where the gap between the surfaces is an even multiple of  $\lambda/2$  and the reflected waves are in phase.

Since the wavelength of the light is known, the gap at the  $n_r^{th}$  ring can be obtained as

$$g = n_r \left( \frac{1}{2} \lambda \right), \quad (\text{B.1})$$

where  $\lambda$  is the wavelength of the light source and  $n_r$  is the ring number counting outward from

the center dark region (the  $0^{th}$  ring).

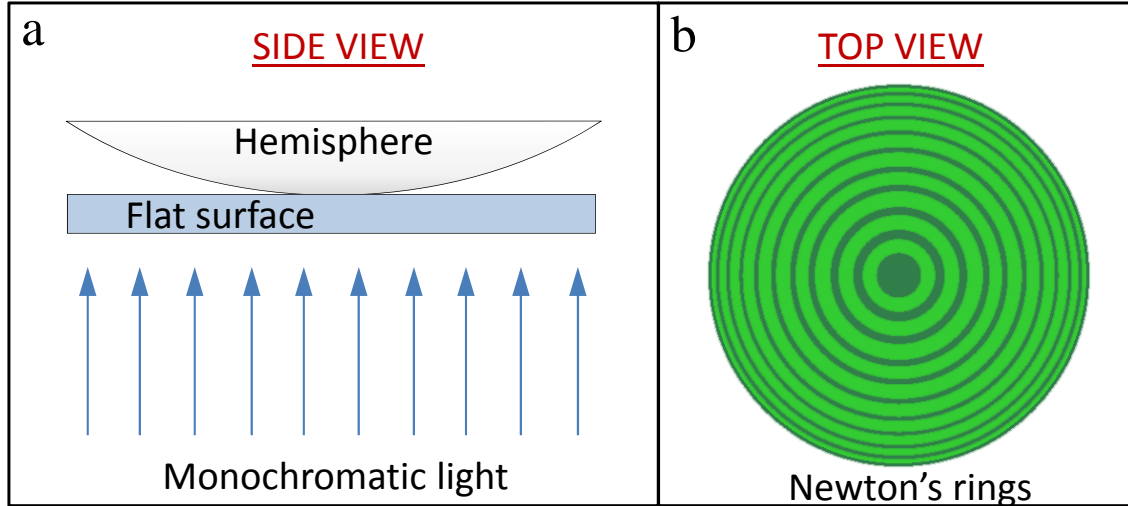


Figure B.1: Schematics of a typical experimental setup to observe contact area using interferometric microscopy. **(a)** Side view schematics of the setup in which a monochromatic light is channeled onto the contact interface. **(b)** Newton's rings interference pattern is observed from a top view through a microscope. The dark rings are as a result of destructive interference between the light rays reflected from the two surfaces which are  $180^\circ$  out of phase, while the bright rings are due to constructive interference from the reflected waves which are in phase.

# Bibliography

- [1] Uyiosa Abusomwan and Metin Sitti. Effect of retraction speed on adhesion of elastomer fibrillar structures. *Applied Physics Letters*, 101(21):211907, 2012. doi: 10.1063/1.4767360. URL <http://link.aip.org/link/?APL/101/211907/1>. 1.4
- [2] B Aksak, M P Murphy, and M Sitti. Adhesion of Biologically Inspired Vertical and Angled Polymer Microfiber Arrays. *Langmuir*, 23(6):3322–3332, 2007. ISSN 0743-7463. URL [http://pubs3.acs.org/acs/journals/doilookup?in\\_doi=10.1021/la062697t](http://pubs3.acs.org/acs/journals/doilookup?in_doi=10.1021/la062697t). 1.1, 1, 1.4, 2.1, 2.2, 2.4.2, 4.3.1
- [3] Burak Aksak, Chung-yuen Hui, and Metin Sitti. The effect of aspect ratio on adhesion and stiffness for soft elastic fibres. *Journal of the Royal Society, Interface / the Royal Society*, 8(61):1166–1175, January 2011. ISSN 1742-5662. doi: 10.1098/rsif.2010.0582. URL <http://www.ncbi.nlm.nih.gov/pubmed/21227962>. 2.4.1, 2.4.2
- [4] Burak Aksak, Korhan Sahin, and Metin Sitti. The optimal shape of elastomer mushroom-like fibers for high and robust adhesion. *Beilstein Journal of Nanotechnology*, 5:630–638, May 2014. ISSN 2190-4286. doi: 10.3762/bjnano.5.74. URL <http://www.beilstein-journals.org/bjnano/content/5/1/74>. 5.2.1, 5.5
- [5] Aristotle. *Historia Animalium*. Clarendon, Oxford, 1918. URL [http://classics.mit.edu/Aristotle/history\\_anim.9.ix.html](http://classics.mit.edu/Aristotle/history_anim.9.ix.html)[http://classics.mit.edu/Aristotle/history\\$delimiter"026E30F\\$anim.html](http://classics.mit.edu/Aristotle/history$delimiter). 1.1
- [6] E Arzt, S Enders, and S Gorb. Towards a micromechanical understanding of biological

- surface devices. *Zeitschrift für Metallkunde*, 93:345–351, 2002. ISSN 0044-3093. URL <http://cat.inist.fr/?aModele=afficheN&cpsidt=14167793>. 1.2
- [7] E Arzt, S Gorb, and R Spolenak. From micro to nano contacts in biological attachment devices. *Proceedings of the National Academy of Sciences USA*, 100(19):10603–10606, 2003. URL [www.pnas.org/cgi/doi/10.1073/pnas.1534701100](http://www.pnas.org/cgi/doi/10.1073/pnas.1534701100). 1.2
- [8] Eduard Arzt, Stanislav Gorb, and Ralph Spolenak. From micro to nano contacts in biological attachment devices. *Proceedings of the National Academy of Sciences of the United States of America*, 100:10603–10606, 2003. ISSN 0027-8424. doi: 10.1073/pnas.1534701100. 1.2
- [9] a. Asbeck, S. Dastoor, a. Parness, L. Fullerton, N. Esparza, D. Soto, B. Heyneman, and M. Cutkosky. Climbing rough vertical surfaces with hierarchical directional adhesion. *2009 IEEE International Conference on Robotics and Automation*, pages 2675–2680, May 2009. doi: 10.1109/ROBOT.2009.5152864. URL <http://ieeexplore.ieee.org/lpdocs/epic03/wrapper.htm?arnumber=5152864>. 1.1
- [10] K Autumn, Y a Liang, S T Hsieh, W Zesch, W P Chan, T W Kenny, R Fearing, and R J Full. Adhesive force of a single gecko foot-hair. *Nature*, 405(6787):681–5, June 2000. ISSN 0028-0836. doi: 10.1038/35015073. URL <http://www.ncbi.nlm.nih.gov/pubmed/10864324>. 1.1, 1.2, 1.1
- [11] K Autumn, A Dittmore, D Santos, M Spenko, and M Cutkosky. Frictional adhesion: a new angle on gecko attachment. *Journal of Experimental Biology*, 209:3569–3579, 2006. doi: 10.1242/jeb.02486. 1.2
- [12] K Autumn, S T Hsieh, D M Dudek, J Chen, C Chitaphan, and R J Full. Dynamics of geckos running vertically. *Journal of Experimental Biology*, 209(2):260–272, 2006. doi: 10.1242/jeb.01980. URL <http://jeb.biologists.org/cgi/content/abstract/209/2/260>. 1.2



- [13] K Autumn, C Majidi, R E Groff, A Dittmore, and R Fearing. Effective elastic modulus of isolated gecko setal arrays. *Journal of Experimental Biology*, 209(18):3558–3568, 2006. doi: 10.1242/jeb.02469. URL <http://jeb.biologists.org/cgi/content/abstract/209/18/3558>. 1.2
- [14] Kellar Autumn. Properties, Principles, and Parameters of the Gecko Adhesive System. *Biological Adhesives*, pages 225–256, 2006. URL [http://dx.doi.org/10.1007/978-3-540-31049-5\\_12](http://dx.doi.org/10.1007/978-3-540-31049-5_12). 1.2
- [15] Kellar Autumn, Metin Sitti, Yiching a Liang, Anne M Peattie, Wendy R Hansen, Simon Sponberg, Thomas W Kenny, Ronald Fearing, Jacob N Israelachvili, and Robert J Full. Evidence for van der Waals adhesion in gecko setae. *Proceedings of the National Academy of Sciences of the United States of America*, 99(19):12252–6, September 2002. ISSN 0027-8424. doi: 10.1073/pnas.192252799. URL <http://www.pubmedcentral.nih.gov/articlerender.fcgi?artid=129431&tool=pmcentrez&rendertype=abstract>. 1.1, 1.2
- [16] M Barquins and M Ciccotti. On the kinetics of peeling of an adhesive tape under a constant imposed load. *International journal of adhesion and adhesives*, 17(1):65–68, 1997. URL [http://dx.doi.org/10.1016/S0143-7496\(96\)00020-6](http://dx.doi.org/10.1016/S0143-7496(96)00020-6)<http://www.sciencedirect.com/science/article/pii/S0143749696000206>. 2.4.3
- [17] W Barthlott and C Neinhuis. Purity of the sacred lotus, or escape from contamination in biological surfaces. *Planta*, 202(1):1–8, 1997. URL <http://link.springer.com/article/10.1007/s004250050096>. 3.1.2, 3.1.2, 3.1
- [18] Jose Berengueres, Kunio Takahashi, Shigeki Saito, and Kenjiro Tadakuma. Magnetic Hair for Wall Mobility. *Intelligent Robots and Systems, 2006 IEEE/RSJ International Conference on*, pages 3934–3939, 2006. doi: 10.1109/IROS.2006.281826. 1.1

- [19] J Blum. Experiments on Sticking, Restructuring, and Fragmentation of Preplanetary Dust Aggregates. *Icarus*, 143(1):138–146, January 2000. ISSN 00191035. doi: 10.1006/icar.1999.6234. URL <http://linkinghub.elsevier.com/retrieve/pii/S0019103599962346>. 4.3.2, 4.3.2
- [20] Luciano F Boesel, Christian Greiner, Eduard Arzt, and Aránzazu Del Campo. Gecko-Inspired Surfaces: A Path to Strong and Reversible Dry Adhesives. *Advanced materials (Deerfield Beach, Fla.)*, pages 2125–2137, March 2010. ISSN 1521-4095. doi: 10.1002/adma.200903200. URL <http://www.ncbi.nlm.nih.gov/pubmed/20349430>. 1.1, 1.4
- [21] D. Campolo, S. Jones, and R.S. Fearing. Fabrication of gecko foot-hair like nano structures and adhesion to random rough surfaces. *2003 Third IEEE Conference on Nanotechnology, 2003. IEEE-NANO 2003.*, 2:856–859, 2003. doi: 10.1109/NANO.2003.1231049. URL <http://ieeexplore.ieee.org/lpdocs/epic03/wrapper.htm?arnumber=1231049>. 1.1
- [22] Giuseppe Carbone, E Pierro, and SN Gorb. Origin of the superior adhesive performance of mushroom-shaped microstructured surfaces. *Soft Matter*, 7(12):5545–5552, 2011. doi: 10.1039/c0sm01482f. URL <http://pubs.rsc.org/en/content/articlehtml/2011/sm/c0sm01482f>. 3.1.3, 4.2.2, 5.2.1, 5.2.1, 5.4
- [23] RW Carpick, N Agrait, DF Ogletree, and M Salmeron. Measurement of interfacial shear (friction) with an ultrahigh vacuum atomic force microscope. *Journal of Vacuum Science & Technology B: Microelectronics and Nanometer Structures*, 14(2):1289–1295, 1996. URL [http://ieeexplore.ieee.org/xpls/abs\\_all.jsp?arnumber=4968416](http://ieeexplore.ieee.org/xpls/abs_all.jsp?arnumber=4968416). 3.3.2
- [24] Graciela Castellanos, Eduard Arzt, and Marleen Kamperman. Effect of viscoelasticity on adhesion of bioinspired micropatterned epoxy surfaces. *Langmuir : the ACS journal of surfaces and colloids*, 27(12):7752–9, June 2011. ISSN 1520-5827. doi: 10.1021/

- la2009336. URL <http://www.ncbi.nlm.nih.gov/pubmed/21604777>. 2.1, 2.4.1, 2.4.4
- [25] Y T Cheng, D E Rodak, C a Wong, and C a Hayden. Effects of micro- and nano-structures on the self-cleaning behaviour of lotus leaves. *Nanotechnology*, 17(5):1359–1362, March 2006. ISSN 0957-4484. doi: 10.1088/0957-4484/17/5/032. URL <http://stacks.iop.org/0957-4484/17/i=5/a=032?key=crossref.a3b96c275987fff470239796f008192f>. 1.3, 3.1.2
- [26] E. Cheung, M.E. Karagozler, and M. Sitti. A new endoscopic microcapsule robot using beetle inspired microfibrillar adhesives. *Proceedings, 2005 IEEE/ASME International Conference on Advanced Intelligent Mechatronics.*, pages 551–557, 2005. doi: 10.1109/AIM.2005.1511040. URL <http://ieeexplore.ieee.org/lpdocs/epic03/wrapper.htm?arnumber=1511040>. 1.1, 1.5, 1.4
- [27] Eugene Cheung and Metin Sitti. Adhesion of biologically inspired polymer microfibers on soft surfaces. *Langmuir : the ACS journal of surfaces and colloids*, 25(12):6613–6, June 2009. ISSN 0743-7463. doi: 10.1021/la900997p. URL <http://www.ncbi.nlm.nih.gov/pubmed/19449817>. 4.3.1
- [28] Eugene Cheung and Metin Sitti. Enhancing Adhesion of Biologically Inspired Polymer Microfibers with a Viscous Oil Coating. *The Journal of Adhesion*, 87(6):547–557, June 2011. ISSN 0021-8464. doi: 10.1080/00218464.2011.583582. URL <http://www.tandfonline.com/doi/abs/10.1080/00218464.2011.583582>. 1
- [29] A J Crosby, Mark Hageman, and Andrew Duncan. Controlling Polymer Adhesion with ”Pancakes”. *Langmuir*, 21:11738–11743, 2005. 1
- [30] E J De Souza, M Kamperman, G Castellanos, E Kroner, V Armbruester, M S Romann, B Schick, and E Arzt. In vitro adhesion measurements between skin and micropatterned poly(dimethylsiloxane) surfaces. *Conference proceedings : ... Annual*

*International Conference of the IEEE Engineering in Medicine and Biology Society. IEEE Engineering in Medicine and Biology Society. Conference*, 2009(0):6018–21, January 2009. ISSN 1557-170X. doi: 10.1109/IEMBS.2009.5334532. URL <http://www.ncbi.nlm.nih.gov/pubmed/19964886>. 1.1

- [31] A DelCampo, Christian Greiner, Eduard Arzt, A DelCampo, and Aranzazu Del Campo. Contact Shape Controls Adhesion of Bioinspired Fibrillar Surfaces. *Langmuir*, 23(7):3495–3502, March 2007. ISSN 0743-7463. doi: 10.1021/la0633987. URL [http://pubs3.acs.org/acs/journals/doilookup?in\\_doi=10.1021/la7010502](http://pubs3.acs.org/acs/journals/doilookup?in_doi=10.1021/la7010502)<http://www.ncbi.nlm.nih.gov/pubmed/17315904>. 1.4

- [32] A del Campo, Christian Greiner, Eduard Arzt, A DelCampo, and Aranzazu Del Campo. Contact Shape Controls Adhesion of Bioinspired Fibrillar Surfaces. *Langmuir*, 23(7):3495–3502, March 2007. ISSN 0743-7463. doi: 10.1021/la0633987. URL [http://pubs3.acs.org/acs/journals/doilookup?in\\_doi=10.1021/la7010502](http://pubs3.acs.org/acs/journals/doilookup?in_doi=10.1021/la7010502)<http://www.ncbi.nlm.nih.gov/pubmed/17315904>. 5.2.1

- [33] Aránzazu del Campo, Christian Greiner, Irma Álvarez, and Eduard Arzt. Patterend surfaces with pillars with controlled and 3D tip geometry mimicking bioattachment devices. *Advanced Materials*, 19:1973–1977, July 2007. doi: 10.1002/adma.200602476. 1

- [34] B.V Derjaguin, V.M Muller, and Yu.P Toporov. Effect of contact deformations on the adhesion of particles. *Journal of Colloid and Interface Science*, 53(2):314–326, November 1975. ISSN 00219797. doi: 10.1016/0021-9797(75)90018-1. URL <http://linkinghub.elsevier.com/retrieve/pii/0021979775900181>. 3.3.2

- [35] C Dominik and A Tielens. Resistance to rolling in the adhesive contact of two elastic spheres. *Philosophical Magazine A*, 72:783–803, 1995. URL <http://www.tandfonline.com/doi/full/10.1080/01418619508243800>. 3.3.2, 3.3.3,

#### 4.3.2

- [36] Ronald S Fearing. Gecko Adhesion Bibliography, 2014. URL <http://robotics.eecs.berkeley.edu/~ronf/Gecko/gecko-biblio.html>. 5.1
- [37] W Federle, W J P Barnes, W Baumgartner, P Drechsler, and J M Smith. Wet but not slippery: Boundary friction in tree frog adhesive toe pads. *Journal of the Royal Society, Interface / the Royal Society*, 3:689–697, 2006. ISSN 1742-5689. doi: 10.1098/rsif.2006.0135. 5.3
- [38] Xue Feng, Matthew a Meitl, Audrey M Bowen, Yonggang Huang, Ralph G Nuzzo, and John a Rogers. Competing fracture in kinetically controlled transfer printing. *Langmuir : the ACS journal of surfaces and colloids*, 23(25):12555–60, December 2007. ISSN 0743-7463. doi: 10.1021/la701555n. URL <http://www.ncbi.nlm.nih.gov/pubmed/17990898>. 2.1, 2.4.1, 2.4.3
- [39] Huajian Gao and Haimin Yao. Shape insensitive optimal adhesion of nanoscale fibrillar structures. *Proceedings of the National Academy of Sciences USA*, 101(21):7851–7856, May 2004. ISSN 0027-8424. doi: 10.1073/pnas.0400757101. URL <http://www.pubmedcentral.nih.gov/articlerender.fcgi?artid=419520&tool=pmcentrez&rendertype=abstract>. 5.2.1
- [40] Liehui Ge, Sunny Sethi, Lijie Ci, Pulickel M Ajayan, and Ali Dhinojwala. Carbon nanotube-based synthetic gecko tapes. *Proceedings of the National Academy of Sciences*, 104(26):10792–10795, 2007. doi: 10.1073/pnas.0703505104. URL <http://www.pnas.org/cgi/content/abstract/104/26/10792>. 1.3, 5, 1.4, 5.1
- [41] A K Geim, S V Dubonos, I V Grigorieva, K S Novoselov, A A Zhukov, and S Yu Shapoval. Microfabricated adhesive mimicking gecko foot-hair. *Nature Materials*, 2(7):461–463, July 2003. ISSN 1476-1122. doi: 10.1038/nmat917. URL <http://www.ncbi.nlm.nih.gov/pubmed/12776092>. 1.3

- [42] AN Gent and J Schultz. Effect of wetting liquids on the strength of adhesion of viscoelastic material. *The Journal of Adhesion*, 3(4):281–294, 1972. URL <http://www.tandfonline.com/doi/full/10.1080/00218467208072199>. 2.4.3
- [43] Andrew G Gillies and Ronald S Fearing. Shear adhesion strength of thermoplastic gecko-inspired synthetic adhesive exceeds material limits. *Langmuir : the ACS journal of surfaces and colloids*, 27(18):11278–81, September 2011. ISSN 1520-5827. doi: 10.1021/la202085j. URL <http://www.ncbi.nlm.nih.gov/pubmed/21848321>. 1.1, 4.2.2
- [44] Andrew G Gillies, Jonathan Puthoff, Michael J Cohen, Kellar Autumn, and Ronald S Fearing. Dry Self-Cleaning Properties of Hard and Soft Fibrillar Structures. *ACS applied materials & interfaces*, 5(13):1–24, June 2013. ISSN 1944-8252. doi: 10.1021/am400839n. URL <http://www.ncbi.nlm.nih.gov/pubmed/23786527>. 3.1.3, 3.2.3, 3.3.1, 4.3.1
- [45] Paul Glass, Hoyong Chung, Newell R Washburn, and Metin Sitti. Enhanced reversible adhesion of dopamine methacrylamide-coated elastomer microfibrillar structures under wet conditions. *Langmuir*, 25(12):6607–6612, 2009. doi: 10.1021/la9009114. URL <http://pubs.acs.org/doi/abs/10.1021/la9009114>. 1
- [46] Paul Glass, Hoyong Chung, Newell R Washburn, and Metin Sitti. Enhanced wet adhesion and shear of elastomeric micro-fiber arrays with mushroom tip geometry and a photopolymerized p(DMA-co-MEA) tip coating. *Langmuir : the ACS journal of surfaces and colloids*, 26(22):17357–62, November 2010. ISSN 1520-5827. doi: 10.1021/la1029245. URL <http://www.ncbi.nlm.nih.gov/pubmed/20879746>. 1
- [47] N J Glassmaker, T Himeno, C-Y Hui, and J Kim. Design of biomimetic fibrillar interfaces: 1. Making contact. *Journal of the Royal Society, Interface / the Royal Society*, 1(1):23–33, November 2004. ISSN 1742-5689. doi: 10.1098/rsif.2004.0004. URL <http://www.pubmedcentral.nih.gov/articlerender>.

- fcgi?artid=1618938&tool=pmcentrez&rendertype=abstract. 1, 2.3
- [48] S Gorb, M Varenberg, A Peressadko, and J Tuma. Biomimetic mushroom-shaped fibrillar adhesive microstructure. *Journal of The Royal Society Interface*, 4(October 2006):271–275, 2007. doi: 10.1098/rsif.2006.0164. 1.1, 1.4, 3.1.3
- [49] Stanislav N Gorb and Michael Varenberg. Mushroom-shaped geometry of contact elements in biological adhesive systems. *Journal of Adhesion Science and Technology*, 21(12):1175–1183, October 2007. doi: doi:10.1163/156856107782328317. URL <http://www.ingentaconnect.com/content/vsp/ast/2007/00000021/F0020012/art00004>. 4.3.1
- [50] Nick Gravish, Matt Wilkinson, Simon Sponberg, Aaron Parness, Noe Esparza, Daniel Soto, Tetsuo Yamaguchi, Michael Broide, Mark Cutkosky, Costantino Creton, and Kellar Autumn. Rate-dependent frictional adhesion in natural and synthetic gecko setae. *Journal of the Royal Society, Interface / the Royal Society*, 7(43):259–69, February 2010. ISSN 1742-5662. doi: 10.1098/rsif.2009.0133. URL <http://www.pubmedcentral.nih.gov/articlerender.fcgi?artid=2842608&tool=pmcentrez&rendertype=abstract>. 2.1, 2.4.1
- [51] C Greiner, A DelCampo, and E Arzt. Adhesion of Bioinspired Micropatterned Surfaces: Effects of Pillar Radius, Aspect Ratio, and Preload. *Langmuir*, 23(7):3495–3502, 2007. ISSN 0743-7463. 1, 3.3.1, 5.2.1
- [52] W R Hansen and K Autumn. Evidence for self-cleaning in gecko setae. *Proceedings of the National Academy of Sciences USA*, 102(2):385–389, January 2005. URL <http://www.pnas.org/content/102/2/385.abstract>. 1.1, 1.3, 1.3, 1.2, 2.1, 3.1.2, 3.2, 3.1.3, 3.2.3, 3.3.1, 3.3.1, 4.2, 4.3.1
- [53] Matthew B Havener, Vincent Sica, Tian Tang, and Anand Jagota. Biomimetic-

- Core Shell Fibril for Enhanced Adhesion. *Langmuir*, 24(12):6182–6188, June 2008. ISSN 0743-7463. doi: 10.1021/la7032687. URL [http://pubs3.acs.org/acs/journals/doilookup?in\\_doi=10.1021/la7032687](http://pubs3.acs.org/acs/journals/doilookup?in_doi=10.1021/la7032687)<http://www.ncbi.nlm.nih.gov/pubmed/18494513>. 3.2.3
- [54] Elliot W. Hawkes, John Ulmen, Noe Esparza, and Mark R. Cutkosky. Scaling walls: Applying dry adhesives to the real world. *2011 IEEE/RSJ International Conference on Intelligent Robots and Systems*, pages 5100–5106, September 2011. doi: 10.1109/IROS.2011.6095103. URL <http://ieeexplore.ieee.org/lpdocs/epic03/wrapper.htm?arnumber=6095103>. 1.1
- [55] Lars-oliver Heim, Jürgen Blum, Markus Preuss, and Hans-jürgen Butt. Adhesion and Friction Forces between Spherical Micrometer-Sized Particles. *Physical Review Letters*, 83(16):3328–3331, 1999. 4.3.2, 4.3.2
- [56] Audrey Yoke Yee Ho, Lip Pin Yeo, Yee Cheong Lam, and Isabel Rodríguez. Fabrication and Analysis of Gecko-Inspired Hierarchical Polymer Nanosetae. *ACS nano*, 5(3):1897–906, March 2011. ISSN 1936-086X. doi: 10.1021/nn103191q. URL <http://www.ncbi.nlm.nih.gov/pubmed/21355603>. 1.4, 3.2.1
- [57] AM Homola, JN Israelachvili, PM McGuiggan, and ML Gee. Fundamental experimental studies in tribology: the transition from interfacial friction of undamaged molecularly smooth surfaces to normal friction with wear. *Wear*, 136:65–83, 1990. URL <http://www.sciencedirect.com/science/article/pii/0043164890900721>. 3.3.2
- [58] Shihao Hu, Stephanie Lopez, Peter H. Niewiarowski, and Zhenhai Xia. Dynamic self-cleaning in gecko setae via digital hyperextension. *Journal of The Royal Society Interface*, (June):1–30, June 2012. ISSN 1742-5662. doi: 10.1098/rsif.2012.0108. URL <http://www.ncbi.nlm.nih.gov/pubmed/22696482><http://rsif.royalsocietypublishing.org/content/9/76/2781.short>. 1.3, 3.2.2,



#### 4.3.1

- [59] Shihao Hu, Stephanie Lopez, Peter H Niewiarowski, and Zhenhai Xia. Dynamic self-cleaning in gecko setae via digital hyperextension. *Journal of the Royal Society, Interface / the Royal Society*, 9(76):2781–90, November 2012. ISSN 1742-5662. doi: 10.1098/rsif.2012.0108. URL <http://www.ncbi.nlm.nih.gov/pubmed/22696482>. 3.1.3, 3.3, 3.2.2, 3.3.1
- [60] C-Y Y C.-Y. Hui, N. J. Glassmaker, T. Tang, A. Jagota, J R Soc Interface, T Himeno, and J Kim. Design of biomimetic fibrillar interfaces: 2. Mechanics of enhanced adhesion. *Journal of The Royal Society, Interface*, 1(1):35–48, November 2004. ISSN 1742-5689. doi: 10.1098/rsif.2004.0005. URL <http://www.pubmedcentral.nih.gov/articlerender.fcgi?artid=1618930&tool=pmcentrez&rendertype=abstract><http://www.pubmedcentral.nih.gov/articlerender.fcgi?artid=1618938&tool=pmcentrez&rendertype=abstract><http://rsif.royalsocietypublishing.org/cgi/doi/10.1098/rsif.2004.0005>. 1.2, 2.5
- [61] Chung-Yuen Hui, Anand Jagota, Lulin Shen, Ajita Rajan, Nicholas Glassmaker, and Tian Tang. Design of bio-inspired fibrillar interfaces for contact and adhesion theory and experiments. *Journal of Adhesion Science and Technology*, 21:1259–1280, 2007. ISSN 0169-4243. doi: 10.1163/156856107782328362. URL <http://www.tandfonline.com/doi/abs/10.1163/156856107782328362>. 4.2.2
- [62] CY Hui, Lulin Shen, Anand Jagota, and K Autumn. Mechanics of anti-fouling or self-cleaning in gecko setae. In *Proceedings of the 29th Annual Meeting of The Adhesion Society (2006)*, number 6, pages 29–31, 2006. URL <http://scholar.google.com/scholar?hl=en&btnG=Search&q=intitle:Mechanics+of+Anti-fouling+or+Self-cleaning+in+Gecko#0>. 1.3,

2.1, 3.2.3, 3.2.3, 3.3.1, 4.3.1

- [63] Duncan J. Irschick, Christopher C. Austin, Ken Petren, Robert N. Fisher, Jonathan B. Losos, and Olaf Ellers. A comparative analysis of clinging ability among pad-bearing lizards. *Biological Journal of the Linnean Society*, 59(1):21–35, September 1996. ISSN 0024-4066. doi: 10.1111/j.1095-8312.1996.tb01451.x. URL <http://doi.wiley.com/10.1111/j.1095-8312.1996.tb01451.x>. 1.2, 2.4.2
- [64] Hadi Izadi, Boxin Zhao, Yougun Han, Neil McManus, and Alexander Penlidis. Teflon hierarchical nanopillars with dry and wet adhesive properties. *Journal of Polymer Science Part B: Polymer Physics*, 50(12):846–851, June 2012. ISSN 08876266. doi: 10.1002/polb.23076. URL <http://doi.wiley.com/10.1002/polb.23076>. 1.4
- [65] H. Minshall J. A. Greenwood and D. Tabor. Hysteresis losses in rolling and sliding friction. *Proceedings of the Royal Society of London. Series A*, 259:480–507, 1961. URL <http://rspa.royalsocietypublishing.org/content/259/1299/480.short>. 4.3.2
- [66] Anand Jagota and Stephen J Bennison. Mechanics of adhesion through a fibrillar microstructure. *Integrative and comparative biology*, 42(6):1140–5, December 2002. ISSN 1540-7063. doi: 10.1093/icb/42.6.1140. URL <http://www.ncbi.nlm.nih.gov/pubmed/21680398>. 1.1
- [67] H E Jeong, S H Lee, P Kim, and K Y Suh. Stretched Polymer Nanohairs by Nanodrawing. *Nano Letters*, 6(7):1508–1513, 2006. ISSN 1530-6984. URL [http://pubs3.acs.org/acs/journals/doilookup?in\\_doi=10.1021/nl061045m](http://pubs3.acs.org/acs/journals/doilookup?in_doi=10.1021/nl061045m). 2
- [68] Hoon Eui Jeong, Sung Hoon Lee, Pilnam Kim, Kahp Y Suh, Hoon Eui, and Sung Hoon. High aspect-ratio polymer nanostructures by tailored capillarity and adhesive force. *Colloids and Surfaces A: Physicochemical and Engineering Aspects*, 313-314:359–364, February 2008. ISSN 09277757. doi: 10.1016/j.colsurfa.2007.

- 04.163. URL <http://www.sciencedirect.com/science/article/B6TFR-4NXRMGH-8/1/cf0b8a09db15620866d74e6f253080cehttp://linkinghub.elsevier.com/retrieve/pii/S092777570700550X>. 2
- [69] Hoon Eui Jeong, Jin-Kwan Lee, Hong Nam Kim, Sang Heup Moon, and Kahp Y Suh. A nontransferring dry adhesive with hierarchical polymer nanohairs. *Proceedings of the National Academy of Sciences of the United States of America*, 106(14):5639–44, April 2009. ISSN 1091-6490. doi: 10.1073/pnas.0900323106. URL <http://www.pubmedcentral.nih.gov/articlerender.fcgi?artid=2667085&tool=pmcentrez&rendertype=abstract>. 1.1, 1, 1.4, 1.4, 1.5
- [70] K L Johnson, K Kendall, and A D Roberts. Surface Energy and Contact of Elastic Solids. *Proceedings of the Royal Society of London. Series A*, 324:301–313, 1971. 2.5, 3.3.2, 3.3.2
- [71] Walid Bin Khaled and Dan Sameoto. Fabrication and characterization of thermoplastic elastomer dry adhesives with high strength and low contamination. *ACS applied materials & interfaces*, 6(9):6806–15, May 2014. ISSN 1944-8252. doi: 10.1021/am500616a. URL <http://www.ncbi.nlm.nih.gov/pubmed/24712514>. 3
- [72] Dong Sung Kim, Hyun Sup Lee, Junghyun Lee, Sungjoo Kim, Kun-Hong Lee, Wonkyu Moon, and Tai Hun Kwon. Replication of high-aspect-ratio nanopillar array for biomimetic gecko foot-hair prototype by UV nano embossing with anodic aluminum oxide mold. *Microsystem Technologies*, 13(5):601–606, 2007. URL <http://dx.doi.org/10.1007/s00542-006-0220-1>. 2
- [73] Sangbae Kim and Matthew Spenko. Whole body adhesion: hierarchical, directional and distributed control of adhesive forces for a climbing robot. In *2007 IEEE International Conference on Robotics and Biomimetics (ROBIO)*, number April, pages 1268–1273. Ieee, April 2007. ISBN 1-4244-0602-1. doi: 10.1109/ROBOT.2007.363159. URL <http://ieeexplore.ieee.org/lpdocs/epic03/wrapper.htm?>

arnumber=4209263[http://ieeexplore.ieee.org/xpls/abs\\_all.jsp?arnumber=4209263](http://ieeexplore.ieee.org/xpls/abs_all.jsp?arnumber=4209263). 1.5

- [74] Seok Kim and Metin Sitti. Biologically inspired polymer microfibers with spatulate tips as repeatable fibrillar adhesives. *Applied Physics Letters*, 89, 2006. ISSN 00036951. doi: 10.1063/1.2424442. 5.1
- [75] Seok Kim and Metin Sitti. Biologically inspired polymer microfibers with spatulate tips as repeatable fibrillar adhesives. *Applied Physics Letters*, 89(26):261911, 2006. URL <http://link.aip.org/link/?APL/89/261911/1>. 1, 1.4
- [76] Seok Kim, Eugene Cheung, and Metin Sitti. Wet self-cleaning of biologically inspired elastomer mushroom shaped microfibrillar adhesives. *Langmuir : the ACS journal of surfaces and colloids*, 25(13):7196–9, July 2009. ISSN 0743-7463. doi: 10.1021/la900732h. URL <http://www.ncbi.nlm.nih.gov/pubmed/19469557>. 3.1.3, 3.2.1, 3.2.1, 3.3.1
- [77] Seok Kim, Metin Sitti, Tao Xie, and Xingcheng Xiao. Reversible dry micro-fibrillar adhesives with thermally controllable adhesion. *Soft Matter*, 5(19):3689, 2009. ISSN 1744-683X. doi: 10.1039/b909885b. URL <http://xlink.rsc.org/?DOI=b909885b>. 1.1, 1.4
- [78] Seok Kim, Jian Wu, Andrew Carlson, Sung Hun Jin, Anton Kovalsky, Paul Glass, Zhuangjian Liu, Numair Ahmed, Steven L Elgan, Weiqiu Chen, Placid M Ferreira, Metin Sitti, Yonggang Huang, and John a Rogers. Microstructured elastomeric surfaces with reversible adhesion and examples of their use in deterministic assembly by transfer printing. *Proceedings of the National Academy of Sciences of the United States of America*, 107(40):17095–100, October 2010. ISSN 1091-6490. doi: 10.1073/pnas.1005828107. URL <http://www.pubmedcentral.nih.gov/articlerender.fcgi?artid=2951455&tool=pmcentrez&rendertype=abstract>. 1.1, 1.4, 1.5, 2.1, 2.4.1, 3.3.1

- [79] Tanu Suryadi Kustandi, Victor Donald Samper, Wan Sing Ng, Ai Shing Chong, and Han Gao. Fabrication of a gecko-like hierarchical fibril array using a bonded porous alumina template. *Journal of Micromechanics and Microengineering*, 17(10):N75–N81, October 2007. ISSN 0960-1317. doi: 10.1088/0960-1317/17/10/N02. URL <http://stacks.iop.org/0960-1317/17/i=10/a=N02?key=crossref.3845d5f814455a087fe59a493363a9ee>. 1.4
- [80] T.S. T.S. Kustandi, Victor Donald V.D. V.D. Samper, D.K. D.K. Dong Kee D.K. D.K. Yi, W.S. W.S. Wan Sing Ng, Pavel Neuzil, W. Sun, By Tanu, and Suryadi Kustandi. Self-Assembled Nanoparticles Based Fabrication of Gecko Foot-Hair-Inspired Polymer Nanofibers. *Advanced Functional Materials*, 17(13): 2211–2218, September 2007. ISSN 1616301X. doi: 10.1002/adfm.200600564. URL <http://doi.wiley.com/10.1002/adfm.200600564><http://dx.doi.org/10.1002/adfm.200600564>. 3.2.1
- [81] MK Kwak, HE Jeong, WG Bae, HS Jung, and KY Suh. Anisotropic Adhesion Properties of Triangular-Tip-Shaped Micropillars. *Small*, 7(16):2296–2300, 2011. URL <http://onlinelibrary.wiley.com/doi/10.1002/sml1.201100455/full>. 1.4
- [82] Moon Kyu Kwak, Hoon-Eui Jeong, and Kahp Y Suh. Rational Design and Enhanced Biocompatibility of a Dry Adhesive Medical Skin Patch. *Advanced materials (Deerfield Beach, Fla.)*, pages 1–5, July 2011. ISSN 1521-4095. doi: 10.1002/adma.201101694. URL <http://www.ncbi.nlm.nih.gov/pubmed/21796686>. 1.1, 1.5, 1.4
- [83] Moon Kyu Kwak, Changhyun Pang, Hoon-Eui Jeong, Hong-Nam Kim, Hyunsik Yoon, Ho-Sup Jung, and Kahp-Yang Suh. Towards the Next Level of Bioinspired Dry Adhesives: New Designs and Applications. *Advanced Functional Materials*, pages n/a–n/a, September 2011. ISSN 1616301X. doi: 10.1002/adfm.201100982. URL <http://doi.wiley.com/10.1002/adfm.201100982>. 1.1
- [84] M Lamblet, E Verneuil, T Vilmin, a Buguin, P Silberzan, and L Léger. Adhesion en-

- hancement through micropatterning at polydimethylsiloxane-acrylic adhesive interfaces. *Langmuir : the ACS journal of surfaces and colloids*, 23(13):6966–74, June 2007. ISSN 0743-7463. doi: 10.1021/la063104h. URL <http://www.ncbi.nlm.nih.gov/pubmed/17511481>. 1
- [85] M Lanzetta and M R Cutkosky. Shape Deposition Manufacturing of Biologically Inspired Hierarchical Microstructures. *CIRP Annals - Manufacturing Technology*, 57(1): 231–234, 2008. ISSN 00078506. doi: 10.1016/j.cirp.2008.03.102. URL <http://linkinghub.elsevier.com/retrieve/pii/S0007850608000541>. 1.4
- [86] Dong Yun Lee, Dae Ho Lee, Seung Goo Lee, and Kilwon Cho. Hierarchical gecko-inspired nanohairs with a high aspect ratio induced by nanoyielding. *Soft Matter*, 8(18): 4905, 2012. ISSN 1744-683X. doi: 10.1039/c2sm07319f. URL <http://xlink.rsc.org/?DOI=c2sm07319f>. 1.4
- [87] Haeshin Lee, Bruce P Lee, and Phillip B Messersmith. A reversible wet/dry adhesive inspired by mussels and geckos. *Nature*, 448(19):338–342, 2007. doi: 10.1038/nature05968. URL <http://www.nature.com/nature/journal/vaop/ncurrent/full/nature05968.html>. 1.4
- [88] Jongho Lee and Ronald S Fearing. Contact self-cleaning of synthetic gecko adhesive from polymer microfibers. *Langmuir*, 24(19):10587–91, October 2008. ISSN 0743-7463. doi: 10.1021/la8021485. URL <http://www.ncbi.nlm.nih.gov/pubmed/18781819>. 4, 2.1, 3.1.3, 3.3, 3.2.3, 3.3.1, 3.3.1, 4.3.1
- [89] Jongho Lee and RS Ronald S Fearing. Wet Self-Cleaning of Superhydrophobic Microfiber Adhesives Formed from High Density Polyethylene. *Langmuir*, 28(43):15372–15377, October 2012. ISSN 1520-5827. doi: 10.1021/la303017a. URL <http://www.ncbi.nlm.nih.gov/pubmed/23072291><http://pubs.acs.org/doi/abs/10.1021/la303017a>. 3.1.3, 3.2.1, 3.2.1, 3.3, 3.3.1, 4.3.1

- [90] Jongho Lee, Ronald S. Fearing, and Kyriakos Komvopoulos. Directional adhesion of gecko-inspired angled microfiber arrays. *Applied Physics Letters*, 93(19):191910, 2008. ISSN 00036951. doi: 10.1063/1.3006334. URL <http://link.aip.org/link/APPLAB/v93/i19/p191910/s1&Agg=doi>. 1.4
- [91] Alborz Mahdavi, Lino Ferreira, Cathryn Sundback, Jason W Nichol, Edwin P Chan, David J D Carter, Chris J Bettinger, Siamrut Patanavanich, Loice Chignozha, Eli Ben-Joseph, Alex Galakatos, Howard Pryor, Irina Pomerantseva, Peter T Masiakos, William Faquin, Andreas Zumbuehl, Seungpyo Hong, Jeffrey Borenstein, Joseph Vacanti, Robert Langer, and Jeffrey M Karp. A biodegradable and biocompatible gecko-inspired tissue adhesive. *Proceedings of the National Academy of Sciences*, 105(7):2307–2312, February 2008. ISSN 1091-6490. doi: 10.1073/pnas.0712117105. URL <http://www.pubmedcentral.nih.gov/articlerender.fcgi?artid=2268132&tool=pmcentrez&rendertype=abstracthttp://www.pnas.org/cgi/content/abstract/105/7/2307>. 1.1, 1.5
- [92] C. Majidi, R. E Groff, Y. Maeno, B. Schubert, S. Baek, B. Bush, R. Maboudian, N. Gravish, M. Wilkinson, K. Autumn, and R. S Fearing. High Friction from a Stiff Polymer Using Microfiber Arrays. *Physical Review Letters*, 97(7):76103, August 2006. ISSN 0031-9007. doi: 10.1103/PhysRevLett.97.076103. URL <http://link.aps.org/abstract/PRL/v97/e076103http://link.aps.org/doi/10.1103/PhysRevLett.97.076103>. 4
- [93] Carmel S. Majidi, Richard E. Groff, and Ronald S. Fearing. Attachment of fiber array adhesive through side contact. *Journal of Applied Physics*, 98(10):103521, 2005. ISSN 00218979. doi: 10.1063/1.2128697. URL <http://link.aip.org/link/JAPIAU/v98/i10/p103521/s1&Agg=doi>. 2.1
- [94] D Maugis. *Contact, Adhesion and Rupture of Elastic Solids*. Springer, 2000. 2.2, 2.2, 2.4.3, 3.3.2

- [95] Yigit Mengüç, Michael Röhrig, Uyiosa Abusomwan, Hendrik Holscher, and Metin Sitti. Staying sticky: contact self-cleaning of gecko-inspired adhesives. *Journal of The Royal Society Interface*, 11(94):20131205, May 2014. ISSN 1742-5662. doi: 10.1098/rsif.2013.1205. URL <http://www.ncbi.nlm.nih.gov/pubmed/24554579><http://171.66.127.193/content/11/94/20131205.short>. 3.1.3, 3.2.3, 3.3.1, 4.3.1, 5.1, 5.3.2, 5.2
- [96] Yigit Mengüç, Sang Yoon Yang, Seok Kim, John a. Rogers, and Metin Sitti. Gecko-Inspired Controllable Adhesive Structures Applied to Micromanipulation. *Advanced Functional Materials*, 22(6):1246–1254, March 2012. ISSN 1616301X. doi: 10.1002/adfm.201101783. URL <http://doi.wiley.com/10.1002/adfm.201101783>. 1.1, 1.4, 1.4, 1.5
- [97] C Menon, M Murphy, and M Sitti. Gecko Inspired Surface Climbing Robots. *Robotics and Biomimetics, 2004. ROBIO 2004. IEEE International Conference on*, pages 431–436, 2004. doi: 10.1109/ROBIO.2004.1521817. 1.1
- [98] C. Menon, Y. Li, D. Sameoto, and C. Martens. Abigaille-I: Towards the development of a spider-inspired climbing robot for space use. *2008 2nd IEEE RAS & EMBS International Conference on Biomedical Robotics and Biomechatronics*, pages 384–389, October 2008. doi: 10.1109/BIOROB.2008.4762903. URL <http://ieeexplore.ieee.org/lpdocs/epic03/wrapper.htm?arnumber=4762903>. 1.1
- [99] L Mø lhave, T Schneider, S.K Kjæ rgaard, L Larsen, S Norn, and O Jø rgensen. House dust in seven Danish offices, 2000. ISSN 13522310. (document), 5.5, 5.1
- [100] M P Murphy and M Sitti. Waalbot: An Agile Small-Scale Wall-Climbing Robot Utilizing Dry Elastomer Adhesives. *IEEE/ASME Trans. on Mechatronics*, 12(3):330–338, 2007. ISSN 1083-4435. 1.1, 1.5
- [101] M. P. Murphy, C. Kute, Y. Menguc, and M. Sitti. Waalbot II: Adhesion Recovery and



- Improved Performance of a Climbing Robot using Fibrillar Adhesives. *The International Journal of Robotics Research*, 30(1):118–133, October 2010. ISSN 0278-3649. doi: 10.1177/0278364910382862. URL <http://ijr.sagepub.com/cgi/doi/10.1177/0278364910382862>. 1.1, 1.4, 1.5
- [102] Michael Murphy, Burak Aksak, and Metin Sitti. Adhesion and anisotropic friction enhancements of angled heterogeneous micro-fiber arrays with spherical and spatula tips. *Journal of Adhesion Science and Technology*, 21(12):1281–1296, October 2007. URL <http://dx.doi.org/10.1163/156856107782328380>. 1, 1.4, 4.2.1
- [103] Michael P Murphy, Burak Aksak, and Metin Sitti. Gecko-inspired directional and controllable adhesion. *Small (Weinheim an der Bergstrasse, Germany)*, 5(2):170–5, February 2009. ISSN 1613-6829. doi: 10.1002/sml.200801161. URL <http://www.ncbi.nlm.nih.gov/pubmed/19115348>. 1.3, 1, 1.4
- [104] Michael P Murphy, Seok Kim, and Metin Sitti. Enhanced adhesion by gecko-inspired hierarchical fibrillar adhesives. *ACS applied materials & interfaces*, 1(4):849–55, April 2009. ISSN 1944-8244. doi: 10.1021/am8002439. URL <http://www.ncbi.nlm.nih.gov/pubmed/20356011>. 1.1, 1.3, 1, 1.4
- [105] Dadhichi Paretkar, Marleen Kamperman, David Martina, Jiahua Zhao, Costantino Creton, Anke Lindner, Anand Jagota, Robert McMeeking, and Eduard Arzt. Preload-responsive adhesion: effects of aspect ratio, tip shape and alignment., June 2013. ISSN 1742-5662. URL <http://www.ncbi.nlm.nih.gov/pubmed/23554348>. 3.3.1, 5.2.1
- [106] Aaron Parness, Daniel Soto, Noe Esparza, Nick Gravish, Matt Wilkinson, Kellar Autumn, and Mark Cutkosky. A microfabricated wedge-shaped adhesive array displaying gecko-like dynamic adhesion, directionality and long lifetime. *Journal of The Royal Society Interface*, 6(41):1223–1232, 2009. doi: 10.1098/rsif.2008.0048. URL <http://rsif.royalsocietypublishing.org/content/6/41/1223.short>. 1,

- [107] B N J Persson, S. Gorb, and B. N. J. Persson. The effect of surface roughness on the adhesion of elastic plates with application to biological systems. *Journal of Chemical Physics*, 119(21):11437–11444, 2003. ISSN 00219606. doi: 10.1063/1.1621854. URL <http://link.aip.org/link/JCPSA6/v119/i21/p11437/s1&Agg=doi>. 4.2.2
- [108] B N J Persson. Biological Adhesion for Locomotion on Rough Surfaces : Basic Principles and A Theorist s View. *MRS Bulletin*, 32:486–490, 2007. 4.2.2
- [109] B.N.J Persson. Noadhesion. *Wear*, 254(9):832–834, May 2003. ISSN 00431648. doi: 10.1016/S0043-1648(03)00233-3. URL <http://linkinghub.elsevier.com/retrieve/pii/S0043164803002333>. 1.2
- [110] Marco Piccardo, Antoine Chateauminois, Christian Fretigny, Nicola M Pugno, and Metin Sitti. Contact compliance effects in the frictional response of bioinspired fibrillar adhesives. *Journal of the Royal Society, Interface / the Royal Society*, 10(83): 20130182, July 2013. ISSN 1742-5662. doi: 10.1098/rsif.2013.0182. URL <http://www.ncbi.nlm.nih.gov/pubmed/23554349>. 3.3.2, 3.7
- [111] J. B. Puthoff, M. Holbrook, M. J. Wilkinson, K. Jin, N. S. Pesika, and K. Autumn. Dynamic friction in natural and synthetic gecko setal arrays. *Soft Matter*, 9(19):4855, 2013. ISSN 1744-683X. doi: 10.1039/c3sm50267h. URL <http://xlink.rsc.org/?DOI=c3sm50267h>. 2.1, 2.4.1
- [112] L Qu and L Dai. Gecko-Foot-Mimetic Aligned Single-Walled Carbon Nanotube Dry Adhesives with Unique Electrical and Thermal Properties. *Advanced Materials*, 19(22): 3844–3849, 2007. URL <http://dx.doi.org/10.1002/adma.200700023>. 5
- [113] S. Reddy, E. Arzt, A DelCampo, and a. delCampo. Bioinspired Surfaces with Switchable Adhesion. *Advanced Materials*, 19(22):3833–3837, November 2007. ISSN 09359648. doi: 10.1002/adma.200700733. URL <http://dx.doi.org/10.1002/adma>.

200700733<http://doi.wiley.com/10.1002/adma.200700733>. 1.4

- [114] Michael Röhrig, Michael Thiel, Matthias Worgull, and Hendrik Hölscher. 3D direct laser writing of nano- and microstructured hierarchical gecko-mimicking surfaces. *Small (Weinheim an der Bergstrasse, Germany)*, 8(19):3009–15, October 2012. ISSN 1613-6829. doi: 10.1002/sml.201200308. URL <http://www.ncbi.nlm.nih.gov/pubmed/22778085>. 1.4
- [115] D Sameoto and C Menon. Recent advances in the fabrication and adhesion testing of biomimetic dry adhesives. *Smart Materials and Structures*, 19(10):103001, October 2010. ISSN 0964-1726. doi: 10.1088/0964-1726/19/10/103001. URL <http://stacks.iop.org/0964-1726/19/i=10/a=103001?key=crossref.3264d868b2c2cb6c13147baacceb4b2d>. 1.1
- [116] D Sameoto, C Menon, Menrva Group, Engineering Science, Simon Fraser, and B C Va. Direct molding of dry adhesives with anisotropic peel strength using an offset lift-off photoresist mold. *Journal of Micromechanics and Microengineering*, 19(11):115026, November 2009. ISSN 0960-1317. doi: 10.1088/0960-1317/19/11/115026. URL <http://stacks.iop.org/0960-1317/19/i=11/a=115026?key=crossref.455535a8a8795c7729ce2692f8a42136><http://stacks.iop.org/0960-1317/19/i=11/a=115002?key=crossref.16cb67ecf9750091f792e0365e1be53b>. 1.1
- [117] Dan Sameoto, Yasong Li, and Carlo Menon. Multi-Scale Compliant Foot Designs and Fabrication for Use with a Spider-Inspired Climbing Robot. *Journal of Bionic Engineering*, 5(3):189–196, September 2008. ISSN 16726529. doi: 10.1016/S1672-6529(08)60024-4. URL <http://linkinghub.elsevier.com/retrieve/pii/S1672652908600244>. 1.1
- [118] Daniel Santos, Sangbae Kim, Matthew Spenko, Aaron Parness, and Mark Cutkosky. Directional Adhesive Structures for Controlled Climbing on Smooth Vertical Surfaces.

*IEEE International Conference on Robotics and Automation*, pages 1262–1267, 2007.

1.1

- [119] Daniel Santos, Matthew Spenko, Aaron Parness, Sangbae Kim, and Mark Cutkosky. Directional adhesion for climbing: theoretical and practical considerations. *Journal of Adhesion Science and Technology*, 21(12):1317–1341, October 2007. ISSN 01694243. doi: doi:10.1163/156856107782328399. URL <http://openurl.ingenta.com/content/xref?genre=article&issn=0169-4243&volume=21&issue=12&spage=1317><http://www.ingentaconnect.com/content/vsp/ast/2007/00000021/F0020012/art00010>. 1.4
- [120] B Schubert, C Majidi, RE Groff, S Baek, and B Bush. Towards friction and adhesion from high modulus microfiber arrays. *Journal of Adhesion Science and Technology*, 21(12):1297–1315, 2007. URL <http://www.tandfonline.com/doi/full/10.1163/156856107782328344>. 1.1, 4
- [121] Sunny Sethi, Liehui Ge, Lijie Ci, P M Ajayan, and Ali Dhinojwala. Gecko-Inspired Carbon Nanotube-Based Self-Cleaning Adhesives. *Nano Letters*, 8(3):822–825, March 2008. ISSN 1530-6984. doi: 10.1021/nl0727765. URL <http://www.ncbi.nlm.nih.gov/pubmed/18266335>[http://pubs3.acs.org/acs/journals/doi/lookup?in\\_doi=10.1021/nl0727765](http://pubs3.acs.org/acs/journals/doi/lookup?in_doi=10.1021/nl0727765). 3.1.3, 3.2.1, 3.2.1, 3.2.2, 3.2.2, 3.3.1, 4.3.1
- [122] M Sitti and R S Fearing. Nanomolding Based Fabrication of Synthetic Gecko Foot-hairs. In *Proceedings of the IEEE Nanotechnology Conference*, pages 137–140, 2002. 1.1, 1.4
- [123] Metin Sitti. High Aspect Ratio Polymer Micro/Nano-Structure Manufacturing using Nanoembossing, Nanomolding and Directed Self-Assembly. In *Proc.of the IEEE/ASME Advanced Mechatronics Conference*, pages 886–890, Kobe, Japan, 2003. 4
- [124] Metin Sitti and Ronald S. Fearing. Synthetic gecko foot-hair micro/nano-structures

- as dry adhesives. *Journal of Adhesion Science and Technology*, 17(8):1055–1073, August 2003. ISSN 15685616. doi: 10.1163/156856103322113788. URL <http://www.ingentaselect.com/rpsv/cgi-bin/cgi?ini=xref&body=linker&reqdoi=10.1163/156856103322113788>. 1.1
- [125] A Solga, Z Cerman, BF Striffler, M Spaeth, and W Barthlott. The dream of staying clean: Lotus and biomimetic surfaces. *Bioinspiration & Biomimetics*, 2(4):S126–34, 2007. URL <http://iopscience.iop.org/1748-3190/2/4/S02>. 3.1.2
- [126] Daniel Soto, Ginel Hill, Aaron Parness, Noe Esparza, Mark Cutkosky, and Tom Kenny. Effect of fibril shape on adhesive properties. *Applied Physics Letters*, 97(5):053701, 2010. ISSN 00036951. doi: 10.1063/1.3464553. URL <http://link.aip.org/link/APPLAB/v97/i5/p053701/s1&Agg=doi>. 1, 1.4
- [127] Ralph Spolenak, S. Gorb, H. Gao, E. Arzt, E. The Royal Society, and Engineering Sciences. Effects of contact shape on the scaling of biological attachments. *Proceedings of the Royal Society London Series A*, 461(October 2003):305–319, February 2005. ISSN 1364-5021. doi: 10.1098/rspa.2004.1326. URL <http://rspa.royalsocietypublishing.org/cgi/doi/10.1098/rspa.2004.1326><http://rspa.royalsocietypublishing.org/content/461/2054/305.short>. 2.2
- [128] A. V. Spuskanyuk, R. M. McMeeking, V. S. Deshpande, and E. Arzt. The effect of shape on the adhesion of fibrillar surfaces. *Acta Biomaterialia*, 4:1669–1676, 2008. ISSN 17427061. doi: 10.1016/j.actbio.2008.05.026. 4.2.2, 5.2.1
- [129] Bilsay Sümer and Metin Sitti. Rolling and Spinning Friction Characterization of Fine Particles Using Lateral Force Microscopy Based Contact Pushing. *Journal of Adhesion Science and Technology*, 22(5):481–506, June 2008. ISSN 01694243. doi: 10.1163/156856108X295527. URL <http://openurl.ingenta.com/content/xref?genre=article&issn=>

0169-4243&volume=22&issue=5&spage=481. 3.3.2

- [130] T Sun, L Feng, X Gao, and L Jiang. Bioinspired surfaces with special wettability. *Accounts of Chemical Research*, 38(8):644–652, 2005. URL <http://pubs.acs.org/doi/abs/10.1021/ar040224c>. 3.1.2
- [131] D Tabor. Surface forces and surface interactions. *Journal of Colloid and Interface Science*, 58(1):2–13, 1977. URL <http://www.sciencedirect.com/science/article/pii/0021979777903666>. 3.3.2
- [132] Tian Tang, CY Hui, and NJ Glassmaker. Can a fibrillar interface be stronger and tougher than a non-fibrillar one? *Journal of The Royal Society Interface*, 2(5):505–516, 2005. doi: 10.1098/rsif.2005.0070. URL <http://rsif.royalsocietypublishing.org/content/2/5/505.short>. 2.4.1
- [133] Y.-C. Tsai, W.-P. Shih, Y.-M. Wang, L.-S. Huang, and P.-J. Shih. E-Beam Photoresist and Carbon Nanotubes as Biomimetic Dry Adhesives. *19th IEEE International Conference on Micro Electro Mechanical Systems*, (January):926–929, 2006. doi: 10.1109/MEMSYS.2006.1627952. URL <http://ieeexplore.ieee.org/lpdocs/epic03/wrapper.htm?arnumber=1627952>. 3.2.1
- [134] Yao-Chuan Tsai, Po-Jen Shih, Tzung-Han Lin, and Wen-Pin Shih. Self-cleaning Effects of Biomimetic Dry Adhesives. *2006 1st IEEE International Conference on Nano/Micro Engineered and Molecular Systems*, (c):1388–1391, January 2006. doi: 10.1109/NEMS.2006.334772. URL <http://ieeexplore.ieee.org/lpdocs/epic03/wrapper.htm?arnumber=4135202>. 3.1.3, 3.2.1, 4.3.1
- [135] O Unver, M P Murphy, and M Sitti. Geckobot and Waalbot: Small-Scale Wall Climbing Robots. In *Infotech@Aerospace*, pages 1–10, Arlington, VA, 2005. 1.1
- [136] O Unver, A Uneri, A Aydemir, and M Sitti. Geckobot: a gecko inspired climbing robot using elastomer adhesives. In *IEEE International Conference on Robotics and Automa-*

tion, volume 1, pages 2329–2335, 2006. 4.2

- [137] Shilpi Vajpayee, Rong Long, Lulin Shen, Anand Jagota, and Chung-Yuen Hui. Effect of rate on adhesion and static friction of a film-terminated fibrillar interface. *Langmuir : the ACS journal of surfaces and colloids*, 25(5):2765–71, March 2009. ISSN 0743-7463. doi: 10.1021/la8033885. URL <http://www.ncbi.nlm.nih.gov/pubmed/19437696>. 2.4.1
- [138] Sang Yoon Yang, Andrew Carlson, Huanyu Cheng, Qingmin Yu, Numair Ahmed, Jian Wu, Seok Kim, Metin Sitti, Placid M Ferreira, Yonggang Huang, and John a Rogers. Elastomer Surfaces with Directionally Dependent Adhesion Strength and Their Use in Transfer Printing with Continuous Roll-to-Roll Applications. *Advanced materials (Deerfield Beach, Fla.)*, pages 2117–2122, March 2012. ISSN 1521-4095. doi: 10.1002/adma.201104975. URL <http://www.ncbi.nlm.nih.gov/pubmed/22431430>. 1.5
- [139] H Yao, G Della Rocca, P R Guduru, and H Gao. Adhesion and sliding response of a biologically inspired fibrillar surface: experimental observations. *Journal of The Royal Society Interface*, 2007. URL <http://dx.doi.org/10.1098/rsif.2007.1225>. 1.1
- [140] Betul Yurdumakan, Nachiket R Raravikar, Pulickel M Ajayan, and Ali Dhinojwala. Synthetic gecko foot-hairs from multiwalled carbon nanotubes. *Chemical Communications*, pages 3799–3801, 2005. 5
- [141] Y Zhao, T Tong, L Delzeit, A Kashani, M Meyyappan, and A Majumdar. Interfacial energy and strength of multiwalled-carbon-nanotube-based dry adhesive. *Journal of Vacuum Science & Technology B: Microelectronics and Nanometer Structures*, 24:331–335, 2006. 5